

Electronic Thesis and Dissertation Repository

4-20-2018 10:00 AM

A Numerical Investigation of Human Cough Jet Development and Droplet Dispersion

Ran Bi

The University of Western Ontario

Supervisor

Zhang, Chao

The University of Western Ontario Co-Supervisor

Savory, Eric

The University of Western Ontario

Graduate Program in Mechanical and Materials Engineering

A thesis submitted in partial fulfillment of the requirements for the degree in Master of Engineering Science

© Ran Bi 2018

Follow this and additional works at: <https://ir.lib.uwo.ca/etd>



Part of the [Aerodynamics and Fluid Mechanics Commons](#), [Biomechanical Engineering Commons](#), [Biomechanics and Biotransport Commons](#), and the [Other Mechanical Engineering Commons](#)

Recommended Citation

Bi, Ran, "A Numerical Investigation of Human Cough Jet Development and Droplet Dispersion" (2018). *Electronic Thesis and Dissertation Repository*. 5314.
<https://ir.lib.uwo.ca/etd/5314>

This Dissertation/Thesis is brought to you for free and open access by Scholarship@Western. It has been accepted for inclusion in Electronic Thesis and Dissertation Repository by an authorized administrator of Scholarship@Western. For more information, please contact wlsadmin@uwo.ca.

Abstract

As part of the Western Cold and Flu aerosol (WeCoF) studies, the present study provides Computational Fluid Dynamics (CFD) modelling of human cough flow. The cough flow is characterized in two different aspects, the flow field and the droplets. In the study of the flow field of coughing, various dynamic characteristics, including the velocity variation, streamwise penetration and power spectral density, are examined. CFD simulations using two different approaches, the unsteady Reynolds Averaged Navier-Stokes (URANS) and the large eddy simulation (LES), are performed for comparison purposes. The numerical results are validated by the experimental data obtained from the measurements by the particle image velocimetry (PIV) and hot-wire anemometry (HWA), as well as the published data. Based on the comparison with the URANS approach and the experimental data, the LES approach can be considered as a good candidate to predict the flow field of coughing.

In the study of the droplets produced by coughing, the dynamic characteristics, including the dispersion and evaporation processes, are analyzed. The Lagrangian discrete phase model is adopted to track a total 2084 droplets in the diameter range 3-750 μm . The effects of the relative humidity (RH) of the ambient air and the inlet time-dependent cough velocity on the dispersion and evaporation of the droplets are investigated. It is found that the larger droplets precipitate on the ground as the time progresses, and the precipitating speed depends on the droplet size, whereas the smaller droplets with the diameter $d_p \leq 10 \mu\text{m}$ remain suspended for a longer period. The dispersion process in terms of the droplet penetration is weakened by both a higher ambient RH and a lower inlet cough velocity. The droplet evaporation is significantly affected by the ambient RH, i.e. the higher the RH, the slower the evaporation. However, the inlet cough velocity doesn't show a strong influence on the evaporation of the droplets.

Keywords

Computational Fluid Dynamics (CFD), Human Cough Flow, Flow Field, Droplet, Unsteady Reynolds Averaged Navier-Stokes (URANS), Large Eddy Simulation (LES), Discrete Phase Model

Co-Authorship Statement

The thesis is in the Integrated Article format. Chapter 2 and 3 of this thesis will be submitted for publications.

All the papers are drafted by Ran Bi and corrected under the supervision of Prof. Eric Savory and Prof. Chao Zhang, and in consultation with Dr. Shady Ali in Prof. Eric Savory's Advanced Fluid Mechanics (AFM) research group.

Acknowledgments

First of all, I would like to express my deepest gratitude and appreciation to my supervisors, Prof. Eric Savory and Prof. Chao Zhang, for their guidance, encouragement and support throughout my entire research work.

Then I would express my sincere gratitude to Dr. Shady Ali for his academic help in my research work, and to all my colleagues in Prof. Eric Savory's Advanced Fluid Mechanics (AFM) research group, especially Ahmed Mohamed, Nicholas Dudalski and Dwaipayan Sarkar, who provided me with the experimental data and support for my daily life.

Moreover, I would thank the facilities of the WestGrid, Shared Hierarchical Academic Research Computing Network (SHARCNET) and Compute/Calcul Canada, which provided me with the computational system for my simulation running, as well as the collaborators of the Collaborative Health Research Project (CHRP).

Finally, I would like to express my great gratitude to my family for their love and thoughtful care throughout my entire master's study.

Table of Contents

Abstract	i
Co-Authorship Statement.....	ii
Acknowledgments.....	iii
Table of Contents	iv
List of Tables	vii
List of Figures	viii
List of Appendices	xii
Nomenclature	xiii
Chapter 1	1
1 Introduction	1
1.1 Background.....	1
1.2 Literature Review.....	3
1.2.1 Experimental studies.....	3
1.2.2 Numerical studies.....	4
1.3 Motivation.....	6
1.4 Thesis Scope	6
1.5 Objectives	7
1.6 Thesis Organization	8
References	10
Chapter 2.....	13
2 CFD Modelling of the Flow Field of Coughing	13
2.1 Introduction.....	13
2.1.1 Dynamic characteristics of turbulent free jet flows	14
2.1.2 Numerical studies on turbulent free jet flows	18

2.2 Numerical Methodology	20
2.2.1 Governing equations	20
2.2.1.1 The URANS approach.....	20
2.2.1.2 The LES approach	23
2.2.1.3 Energy equation.....	24
2.2.2 Computational domain and grid.....	25
2.2.3 Boundary and ambient conditions	26
2.2.4 CFD solver	28
2.3 Results and Discussion	30
2.3.1 Velocity field	30
2.3.1.1 Comparison of the results from the URANS and LES approaches	30
2.3.1.2 Comparison with the experimental data from the PIV measurements	32
2.3.1.3 Comparison with the experimental data from the HWA measurements	39
2.3.2 Streamwise penetration and maximum jet width.....	42
2.3.3 Power spectral density	48
2.4 Conclusions.....	51
References.....	54
Chapter 3.....	62
3 CFD Modelling of the Droplets Produced by Coughing	62
3.1 Introduction.....	62
3.1.1 Studies of droplet size distribution	63
3.1.2 Studies of droplet dispersion and evaporation	65
3.1.3 Studies of respiratory pathogen transmission	67
3.2 Numerical Methodology	70

3.2.1	Governing equations	70
3.2.1.1	The LES approach	70
3.2.1.2	Energy equation.....	70
3.2.1.3	Discrete phase model.....	71
3.2.2	Computational domain and grid.....	72
3.2.3	Droplet conditions.....	74
3.2.4	Boundary and ambient conditions	76
3.2.5	CFD solver	79
3.3	Results and Discussion	80
3.3.1	Droplet dispersion.....	80
3.3.1.1	Contours of droplet diameters	80
3.3.1.2	Effect of the ambient RH.....	83
3.3.1.3	Effect of the inlet cough velocity	85
3.3.2	Droplet evaporation	86
3.3.2.1	Effect of the ambient RH.....	86
3.3.2.2	Effect of the inlet cough velocity	90
3.4	Conclusions.....	94
	References.....	97
	Chapter 4.....	102
4	Conclusions and Recommendations	102
4.1	Conclusions.....	102
4.2	Recommendations.....	104
	Appendices.....	105
	Curriculum Vitae	139

List of Tables

Table 2.1: Governing equations of the SST $k-\omega$ turbulence model.	22
Table 2.2: Inlet conditions used in the experiment and LES modelling.	44
Table 3.1: Summary of size distribution of respiratory droplets.	67
Table 3.2: Droplet size distribution (reproduced from Duguid (1946)).	75
Table 3.3: Three cases in different inlet and ambient conditions.	77
Table A-1: Properties of the injected fluid.	120
Table A-2: Properties of the two species of the injected fluid.	120
Table A-3: Information on different grids used for the URANS modelling.	126
Table A-4: Grid independence tests for the URANS modelling.	126
Table A-5: Information on different grids used for the LES modelling.	128
Table A-6: Grid independence tests for the LES modelling.	129

List of Figures

Figure 1.1: The SARS outbreak timeline in 2003 (adapted from Banos & Lacasa (2007))..... 1

Figure 2.1: Schematic of the flow field of coughing (Mohamed, 2017 (with author's permission)). 13

Figure 2.2: Schematic structures of a steady turbulent round free jet (adapted from Abdel-Rahman (2010)). 16

Figure 2.3: Schematic of the computational domain along with its dimensions. 25

Figure 2.4: Grid distribution on the x - z plane ($y=0$) of the computational domain. 26

Figure 2.5: Inlet transient velocity profile (reproduced from Gupta et al. (2009))..... 28

Figure 2.6: Contours of the velocity magnitude at $t = 0.05$ secs for (a) URANS method and (b) LES method. + is at (1, 0, 0) and + is at (1, 0, -0.22). The coordinates are in the unit of metres. 31

Figure 2.7: Contours of the velocity magnitude at $t = 1$ sec for (a) URANS method and (b) LES method..... 31

Figure 2.8: Contours of the velocity magnitude at $t = 2$ secs for (a) URANS method and (b) LES method. 32

Figure 2.9: Contours of the velocity magnitude at $t = 3$ secs for (a) URANS method and (b) LES method. 32

Figure 2.10: Time history of instantaneous velocity magnitude contours obtained from the PIV measurement (Mohamed, 2017 (with author's permission)). 34

Figure 2.11: Time history of instantaneous velocity magnitude contours obtained from the LES modelling. 35

Figure 2.12: A schematic of the x - z plane ($y=0$) of the FLUGIE chamber with the PIV field of view (shaded part, all dimensions are in metres) (adapted from Dudalski et al. (2018)). 36

Figure 2.13: Comparison of the spatially averaged velocities between the numerical and PIV results on the PIV field of view.	37
Figure 2.14: Comparison of the normalized velocity magnitude at the midpoint of each cough flow between the numerical and PIV results.	38
Figure 2.15: Comparison of the normalized velocity u component with (a) the raw data from 11 coughs and (b) the fitting model.	40
Figure 2.16: The general trend of the peak velocity for all the 51 coughs.	41
Figure 2.17: Visualizations of the starting-jet and interrupted-jet stages of the flow field of coughing obtained at (a) 0.30 <i>secs</i> , (b) 0.61 <i>secs</i> , and (c) 1.20 <i>secs</i>	43
Figure 2.18: Illustration of the jet edge, the streamwise penetration distance x_p , the lateral maximum jet width y_w and the corresponding axial distance x_w on the x - y plane ($z=0$).	45
Figure 2.19: Comparison of the streamwise penetration as a function of time (a) at the starting-jet stage and (b) at the interrupted-jet stage.	45
Figure 2.20: (a) Maximum jet width and (b) corresponding axial distance as a function of time in the interrupted-jet stage.	48
Figure 2.21: Comparison of the normalized spectral density.	50
Figure 2.22: Comparison of the power spectral density with the low-pass filter in use.	51
Figure 3.1: Evaporation process of a droplet released by human expiratory activity (adapted from Verreault et al. (2008)).	63
Figure 3.2: Falling and evaporation curve of droplets expelled by human expiratory activity (adapted from Wells (1934)).	63
Figure 3.3: Schematic of the computational domain along with its dimensions.	73
Figure 3.4: Grid distribution on the x - z plane ($y=0$) of the computational domain.	74

Figure 3.5: Duration of the droplet injection (shaded part) (reproduced from Gupta et al. (2009)).....	76
Figure 3.6: Inlet cough velocity profiles employed for Cases #1, #2 and #3 (reproduced from Gupta et al. (2009)).	78
Figure 3.7: Contours of the droplet diameters at (a) 0.15 secs, (b) 0.5 secs, (c) 1 sec, (d) 2 secs, (e) 3 secs and (f) 4 secs on the x-z plane.	82
Figure 3.8: Contours of the droplet diameters at (a) 0.15 secs, (b) 0.5 secs, (c) 1 sec, (d) 2 secs, (e) 3 secs and (f) 4 secs on the y-z plane.	83
Figure 3.9: Comparison of the maximum penetration distance l_m and mean penetration distance $\langle l \rangle$ of the droplets under different ambient RH.	84
Figure 3.10: Comparison of the maximum penetration distance l_m and mean penetration distance $\langle l \rangle$ of the droplets under different inlet cough velocities.....	85
Figure 3.11: Droplet size distributions under different ambient RH at (a) 0.15 secs, (b) 0.5 secs, (c) 1 sec, (d) 2 secs, (e) 3 secs and (f) 4 secs.	88
Figure 3.12: Comparison of the time history of total number of droplets suspended within the computational domain under different ambient RH.	89
Figure 3.13: Comparison of time history of overall mean diameter of the droplets under different ambient RH.	90
Figure 3.14: Droplet size distributions under different inlet cough velocities at (a) 0.15 secs, (b) 0.5 secs, (c) 1 sec, (d) 2 secs, (e) 3 secs and (f) 4 secs.....	92
Figure 3.15: Comparison of time history of total number of droplets suspended under different inlet cough velocities.	93
Figure 3.16: Comparison of time history of overall mean diameter of droplets under different inlet cough velocities.	94
Figure A-1: Schematic of the computational domain along with its dimensions.	105

Figure A-2: Grid distribution on the x - z plane ($y=0$) of the computational domain.	106
Figure A-3: Comparison of the spatial variation of (a) u_j/u_c along the streamwise direction, (b) u/u_c along the vertical direction at $x = 0$, (c) u/u_c along the vertical direction at $x = 3d$, (d) u/u_c along the vertical direction at $x = 20d$, and (e) r_w/d along the streamwise direction with the experimental data.	109
Figure A-4 (a): Schematic layout of the FLUGIE chamber (Mohamed, 2017 (with author's permission)). All dimensions are shown in the unit of metres.	118
Figure A-4 (b): The FLUGIE chamber located in Western University.	119
Figure A-5 (a): Comparison of instantaneous and moving average velocity profiles from the LES modelling.	123
Figure A-5 (b): u' at (1, 0, 0) versus the averaging time $\langle t \rangle$	123
Figure A-6: Streamwise variation of (a) inverse centreline mean velocity decay, (b) normalized centreline TKE and (c) normalized half-width.	127
Figure A-7: Streamwise variation of (a) the peak value of $\langle u \rangle$ along the centreline and (b) the time when peak $\langle u \rangle$ occurs.	129
Figure A-8: Time history of $\langle u \rangle$ at centreline locations of (a) (0.1, 0, 0), (b) (0.2, 0, 0), (c) (0.3, 0, 0) and (d) (0.4, 0, 0). The coordinates are in the unit of metres.	130

List of Appendices

Appendix A: Computational Fluid Dynamic (CFD) Modelling of a Steady Round Free Jet Flow	105
Appendix B: Details about the Governing Equations of the SST Turbulence $k-\omega$ Model ...	110
Appendix C: The Dynamic Smagorinsky-Lilly Model	113
Appendix D: Details about the Energy Equation.....	116
Appendix E: The FLUGIE Cough Chamber	118
Appendix F: Properties of the Injected Fluid.....	120
Appendix G: Moving Average Methodology.....	122
Appendix H: Grid Independence Tests.....	125
Appendix I: The DRW Model	132
Appendix J: Droplet Trajectory	134
Appendix K: Stochastic Collision and Coalescence.....	136
Appendix L: User-Defined Function of the Inlet Velocity Profile for the CFD Modelling of the Steady Round Free Jet Flow	138

Nomenclature

Latin Symbols

c_p	Specific heat capacity (J/kg-K)
$c_{p,j}$	Specific heat capacity of species j (J/kg-K)
C_C	Cunningham correction factor to Stokes' drag law
C_D	Drag force coefficient
C_K	Kolmogorov constant
C_L	Time scale constant
d	Diameter of the inlet (m)
d_p	Diameter of the droplet (μm)
d_w	Distance to the nearest wall
$\langle d_p \rangle$	Overall mean diameter of the droplets (μm)
$D_{j,m}$	Mass diffusion coefficient of species j in the mixture
$D_{T,j}$	Thermal diffusion coefficient of species j
D_ω	Damped cross-diffusion derivative term
D_ω^+	Positive portion of D_ω
e	Total energy
f	Frequency (Hz)
F_D	Drag force per unit droplet mass
F_1, F_2	Blending functions for the SST $k-\omega$ turbulence model

\vec{F}	Additional acceleration
$\sum F_n$	Sum of forces acting on the droplet
g	Gravitational acceleration (m/s ²)
G_k	Production of turbulent kinetic energy
G_ω	Production of specific dissipation rate
h	Sensible enthalpy
\vec{J}_j	Mass diffusion of species j
k	Turbulent kinetic energy (m ² /s ²)
k_i	Molecular thermal conductivity of species i (W/m-K)
k_{eff}	Effective conductivity (W/m-K)
k_m	Molecular thermal conductivity (W/m-K)
k_t	Turbulent thermal conductivity (W/m-K)
l_m	Maximum penetration distance of the droplets from the injector (m)
$\langle l \rangle$	Mean penetration distance of the droplets from the injector (m)
L_e	Eddy length scale
L_S	Mixing length for subgrid scales
$M_{w,i}$	Molecular weight of species i (g/mol)
n	Actual number of collisions
n_1, n_2	Number of the larger and smaller droplets
\bar{n}	Mean number of collisions

N	Total number of droplets suspended within the computational domain
p	Pressure (Pa)
p_{op}	Operating pressure (Pa)
P	Probability of a collision between two droplets
Pr_t	Wall Prandtl number
r_u	Half-width (m)
r_1, r_2	Radius of the larger and smaller droplet
R	Universal gas constant (J/mol-K)/Autocorrelation
Re	Mean flow Reynolds number
Re_r	Relative Reynolds number between the continuous and discrete phase
Re_t	Turbulence Reynolds number
S	Modulus of the mean rate-of-strain tensor
Sc_t	Turbulent Schmidt number
S_{ij}	Mean rate-of-strain tensor
S_k	User-defined source term of k
S_ω	User-defined source term of ω
t	Flow time (<i>secs</i>)
t_{cross}	Particle-eddy crossing time
t_{ip}	Time corresponding to the inlet peak velocity (<i>secs</i>)
t_{iss}	Cough duration (<i>secs</i>)

t_{pk}	Time corresponding to the local peak velocity (<i>secs</i>)
t_s	Time corresponding to the start of the cough (<i>secs</i>)
t_0	Temporal origin in the interrupted-jet stage (m)
t_{1p}	Time corresponding to the initial peak velocity magnitude (<i>secs</i>)
$\langle t \rangle$	Averaging time (<i>secs</i>)
Δt	Time step size (<i>secs</i>)
T	Temperature (K)/Integral time scale of the discrete phase
T_L	Fluid Lagrangian integral time scale
T_{ref}	Reference temperature (K)
u	Axial velocity component (m/s)/Local instantaneous 2D velocity magnitude (m/s)
u_c	Centreline velocity (m/s)
u_i	Velocity component along the i^{th} base vector (m/s)
u_{ip}	Inlet peak velocity (m/s)
u_j	Inlet bulk velocity (m/s)
u_m	Temporal mean inlet velocity (m/s)
u_p	Velocity of the discrete phase (m/s)
u_{pk}	Local peak velocity (m/s)
u_s	Velocity at the start of the cough (m/s)
u_{1p}	Initial peak velocity magnitude (m/s)
u'	RMS of the fluctuating velocity component

$\langle u \rangle$	Moving average of the axial velocity component (m/s)
U	Dimensionless velocity
$\langle U \rangle$	Spatial average of 2D velocity magnitude (m/s)
v_{rel}	Relative velocity between two droplets
V	Volume of one computational grid cell
V_p	Volume of the droplet (m ³)
x	Distance in the streamwise direction from the inlet (m)
x_i	Cartesian coordinate component along the i^{th} base vector
x_p	Streamwise penetration distance (m)
x_w	Axial distance corresponding to the maximum jet width (m)
x_0	Penetration origin in the interrupted-jet stage (m)
X_i	Mole fraction of species i
y	Distance from the closest no-slip wall
y_w	Lateral maximum jet width (m)
Y_j	Mass fraction of species j
Y_k	Dissipation term of k
Y_ω	Dissipation term of ω
z	Distance in the vertical direction from the centreline (m)
z_w	Vertical maximum jet width (m)

Greek Symbols

α^*	Coefficient of Low-Reynolds number correction for the SST k - ω turbulence model
ε	Turbulence dissipation rate (m^2/s^3)
θ_I	Upward jet angle
κ	Von Kármán constant/Wavenumber of an eddy
μ	Dynamic viscosity ($\text{kg}/\text{m}\cdot\text{s}$)
μ_i	Dynamic viscosity of species i ($\text{kg}/\text{m}\cdot\text{s}$)
μ_t	Turbulent viscosity ($\text{kg}/\text{m}\cdot\text{s}$)
ν	Kinematic viscosity (m^2/s)
ν_t	Subgrid-scale eddy-viscosity
ρ	Density (kg/m^3)
ρ_p	Density of the droplet (kg/m^3)
ζ	Normally distributed random number for the Gaussian distribution
ϕ	Energy spectrum ($\text{m}^2/\text{s}^2/\text{Hz}$)
σ_k	Turbulent Prandtl number for k
σ_ω	Turbulent Prandtl number for ω
ω	Specific turbulence dissipation rate (s^{-1})
τ	Dimensionless time
τ_e	Characteristic lifetime of a turbulent eddy
τ_{ij}	Subgrid-scale stress tensor
τ_{kk}	Isotropic portion of the subgrid-scale stress tensor

τ_p	Droplet relaxation time
Γ_k	Effective diffusivity coefficient of k
Γ_ω	Effective diffusivity coefficient of ω
Δ	Local grid scale

Abbreviations

AEM	Analytical Transmission Electron Microscope
AFM	Advanced Fluid Mechanics
APS	Aerodynamic Particle Sizer
CFD	Computational Fluid Dynamics
CFL	Courant-Friedrichs-Lewy
DNS	Direct Numerical Simulation
DRW	Discrete Random Walk
FLUGIE	Fluids from Undergrads with Influenza Enclosure
HFA	Hot Film Anemometry
HSR	High-Speed Rail
HWA	Hot-Wire Anemometry
IMI	Interferometric Mie Imaging
LAPS	Laser Aerosol Particle Spectrometer
LES	Large Eddy Simulation
MUSCL	Monotone Upstream-Centred Schemes for Conservation Laws

OPC	Optical Particle Counter
PIV	Particle Image Velocimetry
RANS	Reynolds Averaged Navier-Stokes
RH	Relative Humidity
RMS	Root-Mean-Square
RNG	Renormalization Group
RSM	Reynolds Stress Model
SARS	Severe Acute Respiratory Syndrome
SFS	Sediment Feeding System
SGS	Subgrid-Scale
SIMPLE	Semi-Implicit Method for Pressure-Linked Equations
SMPS	Scanning Mobility Particle Sizer
SST	Shear Stress Transport
TEB	Thompson Engineering Building
TKE	Turbulent Kinetic Energy
URANS	Unsteady Reynolds Averaged Navier-Stokes
WALE	Wall-Adapting Local Eddy-Viscosity
WHO	World Health Organization

Chapter 1

1 Introduction

1.1 Background

In recent years, infectious respiratory diseases, including Severe Acute Respiratory Syndrome (SARS) and different types of influenza, have received a great deal of attention worldwide. In each year, 200-500 thousand people die because of seasonal influenza (Aliabadi et al., 2011). In November, 2002, SARS emerged initially in Guangdong province, South China, and then spread rapidly around the world and eventually caused around 1,000 deaths (World Health Organization, 2003). Figure 1.1 shows the timeline of the SARS outbreak in 2003. From March to June, hundreds of new cases appeared continuously every month and in total, more than 8,000 cases were found around the world (Banos & Lacasa, 2007).

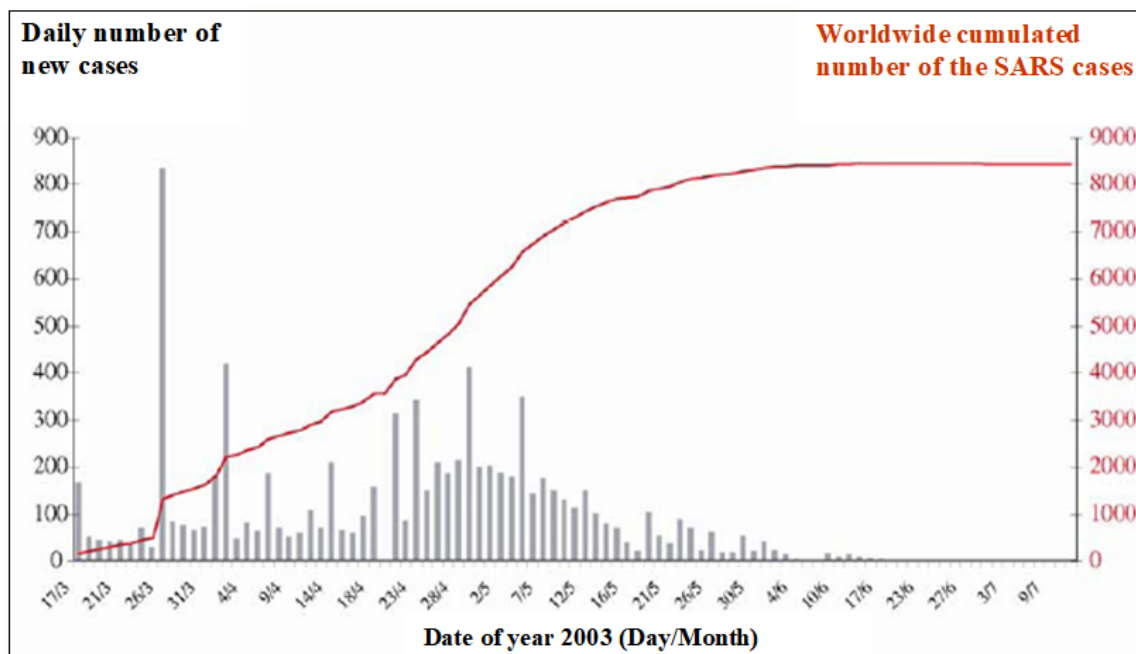


Figure 1.1: The SARS outbreak timeline in 2003 (adapted from Banos & Lacasa (2007)).

However, compared to the outbreak of Spanish influenza in 1918, the impact of SARS was negligible. It was estimated by the World Health Organization (WHO) that from 1918 to 1920, there were 20 million people killed worldwide, and approximately one-quarter of the global population infected by the pandemic of Spanish influenza (Luk et al., 2001). Besides the severe influence on human health, respiratory diseases will also affect the global economy devastatingly. As a conservative estimation, it could cost US\$800 billion per year globally to prevent and treat avian influenza (Gupta et al., 2009). During 2002-2003, the outbreak of SARS resulted in a total loss of around US\$25.3 billion for the China's economy, of which 70% was the loss in the tourism industry (Hai et al., 2004).

Due to the catastrophic impact on human health and global economy, it is significantly important to study, predict and control the transmission of infectious respiratory diseases. Since people spend most of their time in the indoor environment daily, it will be fairly easy for them to be infected by influenza or other types of pandemics. Generally, it is identified that most of the indoor infections are caused by direct or indirect contact (Beggs, 2003). Direct contact, also known as person-to-person contact, means that people may get infected through touching other people who are carrying infectious viruses. Infections will occur rapidly and spread widely in the route of direct contact, especially in the nosocomial environment, if healthcare workers take care of patients without washing their hands effectively (Ayliffe et al., 1988). The indirect contact infection, is through the intermediate inanimate objects and work surfaces. For instance, the medical apparatuses, such as endoscopes and implants, will be polluted by the micro-organisms if they are not disinfected, which will result in infection of the patients (Ostrowsky, 2007 & Arbuthnott, 1992).

An airborne transmission of viruses has been recognized as the main cause of the infection of respiratory diseases in the indoor environment. One of the major sources of airborne viruses is human expiratory activity, which includes breathing, coughing, speaking and sneezing (Morawska, 2006). Such forced exhalation can produce thousands of droplets with various sizes at a high velocity, which are transported by the flow field. Infectious micro-organisms, including viruses, pathogens, bacteria, etc., are contained in the droplet nuclei (Beggs, 2003). Compared to the breathing and speaking processes, coughing and

sneezing can produce higher concentrations of droplets and, therefore, provide higher possibilities to infect others. During coughing and sneezing, the diameters of most droplets produced from the mouth are around 10 μm and some are even larger than 100 μm (Duguid, 1944). After leaving the mouth, the larger droplets fall to the ground first, while the smaller droplets propagate in the air with the diameter decreasing and eventually becoming droplet nuclei, due to evaporation.

1.2 Literature Review

A literature review is provided to introduce the previous work done of the airborne transmission processes during coughing in terms of both the experimental and numerical aspects.

1.2.1 Experimental studies

Coughing can be considered as a multiphase buoyant turbulent flow (Bourouiba et al., 2014). Various factors may affect the spread of the cough flow, such as the cough direction, mouth opening area, expired transient velocity, ambient temperature and relative humidity (RH) (Gupta et al., 2009). As a common symptom for most infections of respiratory diseases, coughing has been investigated more extensively than other forced expiratory behaviours in terms of the flow characteristics and droplet dispersion (Xie et al., 2007). Such information is helpful for a health care organization to find a way to reduce the infection possibility of respiratory diseases. Many previous studies have been conducted to investigate the process of airborne transmission during coughing experimentally. Wei and Li (2017) conducted an experiment in a cuboid water tank to simulate the characteristics of the cough jet. They divided the cough jet into two stages, the starting-jet and interrupted-jet stages, and investigated the influence of different inlet boundary conditions on the dynamic development for both stages. They also developed a protocol to model the droplet transport by using the glass beads which have similar sizes to cough droplets. Chao et al (2009) applied the particle image velocimetry (PIV) and interferometric Mie imaging (IMI) techniques to measure the velocity of the cough flow near the mouth and the droplet size, respectively. Savory et al. (2014) constructed an experimental cough chamber, named FLUGIE (Fluids from Undergrads with Influenza

Enclosure), in order to study the aerodynamics and droplet dispersion of the cough flow far downstream of the mouth, by using the PIV approach. They also recruited the participants who were infected by influenza and used bioaerosol sampling cassettes to collect the droplets from their coughs to quantify the content of the infectious viruses. Similar works were done by Mohamed et al. (2017) and Dudalski et al (2018) who experimentally studied the velocity field of the cough flow produced by both influenza-infected and recuperated human subjects through the PIV and hot-wire anemometry (HWA) measurements. They also employed swabs to collect the nasal mucus from the subjects in order to identify the species of the pathogen as well as to quantify the viral content. Other experimental techniques, such as aerodynamic particle sizer (APS) and high speed camera, were also used to investigate the characteristics of the cough flow and droplet propagation as well as the droplet size (Yang et al., 2007 & Bourouiba et al., 2014).

1.2.2 Numerical studies

Compared with experimental techniques, numerical approaches are relatively more efficient, economical and convenient to use (Kannan, 2015). Numerical approaches are applied extensively in engineering to simulate physical phenomena and to solve practical problems via solving a set of governing equations. One of the numerical methods, which is specially used in the field of fluid mechanics, is the computational fluid dynamics (CFD). The CFD method is developing rapidly and is used in a wide variety of practical applications, such as the production of automobiles, aircraft and ships. By using the CFD method, various fluid phenomena, including different types of laminar and turbulent flows, radiation, heat transfer, etc., can be simulated within an acceptable range of numerical accuracy. Many studies about CFD modelling on the airborne transmission process during coughing were conducted. Aliabadi et al (2010) carried out a CFD simulation of the cough flow by using the unsteady Reynolds Averaged Navier-Stokes (URANS) approach and analyzed the impact of the ambient RH and expired volume on droplet dispersion, heat and mass transfer. In their study, the renormalization group (RNG) k - ϵ model and the Lagrangian discrete phase model were used to solve the turbulence of the flow field and to track the droplets, respectively. Zhu et al (2006b) also did a CFD simulation to investigate the coughing process in a still indoor environment. They simplified the transient cough

flow to be steady, and applied the standard $k-\varepsilon$ turbulence model and Lagrangian method to solve the flow field and droplet dispersion. The experimental data using three different experimental techniques were used to validate the numerical results, which are a PIV system in a styrene-board chamber to measure the velocity of the flow field, a digital video camera in a still thermostatic chamber to record the droplet dispersion process, and a mask to quantify the amount of saliva sprayed during the coughing process. Zhang & Li (2012) studied the droplet dispersion during the coughing process in a high-speed rail (HSR) carriage by using CFD modelling. The carriage was designed to be occupied by 48 passengers which were simulated by 3-dimensional thermal manikins. Four cases under various boundary conditions were studied in order to take into account different surrounding situations occurring in a HSR carriage. They also implemented the URANS approach with the RNG $k-\varepsilon$ model and the Lagrangian discrete phase model to predict the aerodynamic behaviour of the flow field and droplet trajectories, respectively.

In most of the numerical work, the URANS approach has been used to simulate the dynamic development of the flow field. This approach considers the ensemble-averaged component of the flow problem instead of the instantaneous field and requires less computational cost than the direct numerical simulation (DNS) and large eddy simulation (LES) approaches. A turbulence model is needed when using the URANS approach. In some of the previous studies, the RNG $k-\varepsilon$ model has been used successfully to predict the development of the flow field of coughing, due to its superiority in modelling the flow with different Reynolds numbers (Aliabadi et al., 2010 & Zhang & Li, 2012). Other researchers have implemented the standard $k-\varepsilon$ model to solve the flow field (Zhu et al., 2006a).

However, the URANS approach has some limitations. First, the ensemble-averaged field of the flow is obtained from the calculations of the turbulence models based on the governing equations (Berlemont et al., 1990), of which the coefficients are empirical and may influence the accuracy of the simulated results. Furthermore, the fluctuation of the droplets can be approximated by the stochastic tracking model which only takes the random effects of turbulence on the droplet dispersion into consideration and does not solve the coherent structures of the turbulence (Béghein et al., 2005). Besides the URANS approach, the DNS and LES methods are available in CFD modelling to solve the time-dependent

fluid problem. The DNS method resolves the turbulence over the whole range of temporal and spatial scales and, hence, provides the highest accuracy. However, the computational cost is very high, which is not suitable for the present study. The LES method resolves the large scales of turbulence with more precision and only models the small scales of turbulence directly through the subgrid-scale (SGS) turbulence model and, therefore, predicts the fluid phenomena more accurately compared to the URANS method.

1.3 Motivation

Currently, no numerical study of the dynamic development of human cough flow has been conducted by using the LES approach due to the following challenges: (1) the computational cost is much higher than that of the URANS approach; (2) it is difficult to specify the turbulent fluctuations at the inlet for the flow field properly; (3) it is necessary to define the appropriate conditions for the droplets to obtain statistically valid results (Deevy et al., 2008 & Béghein et al., 2005). Furthermore, no comparison of the results between different numerical methods is provided. To better understand the dynamic characteristics of the flow field of coughing, including the velocity variation and the streamwise penetration, and to obtain more accurate numerical results, both the URANS and LES approaches are carried out in the present study for comparison purposes. Such a CFD investigation will analyze the dynamic characteristics of human cough flow, therefore, making significant contributions to our understanding of the dynamic development of human cough flow and to the prevention of respiratory disease transmission.

1.4 Thesis Scope

The present study is aimed at numerically investigating the dynamic development of human cough flow in terms of the flow field and the droplets. In the study of the flow field of coughing, two 3-dimensional simulations using the URANS and LES approaches under the same boundary and ambient conditions are carried out. The numerical results are validated by the experimental data obtained from the measurements by the PIV and HWA techniques, as well as the published data (Wei & Li, 2017). The numerical results of the velocity magnitude contours, the spatially averaged velocity on the PIV field of view and the 2-dimensional velocity magnitude at the midpoint of each cough flow are compared

with the relevant PIV measurements. Similarly, the numerical results of the velocity u component, the peak velocity U_p and the power spectral density at the hot-wire probe location are compared with the HWA measurements. Furthermore, the numerical results regarding the streamwise penetration of the flow field are compared with the experimental work of Wei & Li (2017).

In the study of the droplets produced by coughing, three 3-dimensional simulations using the LES approach and discrete phase model are performed. A total of 2084 droplets in the diameter range of 3-750 μm are injected from 0.042-0.136 *secs*. Two out of the three simulations are conducted under different ambient RH, i.e. 50% and 80%, respectively, in order to analyze the effect of the ambient RH on the droplet dispersion and evaporation. Another two simulations are carried out under different inlet time-dependent cough velocities with the peak values of 22.06 and 10.81 m/s, respectively, to examine the influence of the inlet cough velocity on the droplet dispersion and evaporation. The dispersion process of the droplets is investigated in two aspects, including the contours of the droplet diameters and the penetration distance of the droplets from the mouth. The evaporation process of the droplets is also analyzed in two aspects, the droplet size distribution at different time and the variation of the overall mean droplet diameter with time.

1.5 Objectives

There are three primary objectives of this thesis:

(1) To numerically investigate the dynamic characteristics, such as the velocity variation, streamwise penetration and power spectral density, of the flow field of coughing in a quiescent environment. Two CFD approaches, the URANS and LES, are used. The comparison of the results between these two numerical methods is provided, including the time history of the velocity magnitude contours.

(2) To validate the numerical results of the flow field with the experimental data. The experimental data are obtained from the research article (Wei & Li, 2017) and the PIV and HWA measurements conducted by the author's colleagues from the Advanced Fluid

Mechanics (AFM) research group (Western University) (Mohamed, 2017 & Dudalski et al., 2018). In the experiments, both sick, recuperated and healthy participants have been recruited.

(3) To numerically investigate the characteristics of droplet dispersion and evaporation. The simulations using different time-dependent cough velocities at the inlet and the ambient RH are carried out to study the effects of those conditions on the dispersion and evaporation processes of the droplets produced by coughing.

A secondary objective is to conduct a CFD simulation on a steady-state, turbulent, round free jet. The simulations using the Reynolds Averaged Navier-Stokes (RANS) approach with various turbulence models are performed with the same boundary conditions in order to determine the most appropriate model to be used in the URANS modelling on the flow field of coughing. The experimental data (Xu & Antonia, 2002) is used to validate the numerical results. More details are shown in Appendix A.

1.6 Thesis Organization

The thesis is in the Integrated Article format.

Chapter 1 presents a general introduction about the serious effects of infectious respiratory diseases on human race and how indoor infections occur through human expiratory activity. A literature review of the previous studies in terms of the experimental and numerical work on human cough flow is included. The motivation, scope, objectives and organization of the present study are provided as well in the individual sections.

Chapter 2 discusses the flow field of coughing. The simulations using two CFD approaches, URANS and LES, are performed for comparison purposes. The dynamic characteristics, such as the velocity variation with time, the streamwise penetration and the power spectral density, are analyzed. The experimental data from the literature and the PIV and HWA measurements are used to validate the numerical results.

Chapter 3 discusses the droplets produced by coughing. The discrete phase model based on the Lagrangian equation is used to simulate the performance of the droplet dispersion

and evaporation. The simulations using different time-dependent cough velocities at the inlet and the ambient RH are conducted to analyze the influence of those conditions on the dispersion and evaporation processes of the droplets.

Chapter 4 presents the conclusions of the present study. The comparison of the two CFD methods, the validation of the numerical results, as well as the overall dynamic characteristics of human cough flow in terms of both the flow field and the droplets are summarized. The recommendations for future work regarding the modifications and improvements of the CFD modelling of human cough flow are also provided.

The next chapter will analyze the dynamic characteristics of the flow field of coughing by using both the URANS and LES approaches, and the numerical results will be validated by comparing with some experimental data.

References

- Aliabadi, A. A., Rogak, S. N., Bartlett, K. H., & Green, S. I. (2011). Preventing airborne disease transmission: review of methods for ventilation design in health care facilities. *Advances in Preventive Medicine, 2011*, 1–21.
- Aliabadi, A. A., Rogak, S. N., Green, S. I., & Bartlett, K. H. (2010). CFD simulation of human coughs and sneezes: a study in droplet dispersion, heat, and mass transfer. In *Proceedings of the ASME 2010 International Mechanical Engineering Congress & Exposition (IMECE2010)*, 1051–1060.
- Arbuthnott, J. P. (1992). Staphylococcus. In D. Greenwood, R. C. B. Slack, & J. F. Peutherer (Eds.), *Medical Microbiology* (14th ed). Churchill Livingstone.
- Ayliffe, G. A. J., Babb, J. R., Davies, J. G., & Lilly, H. A. (1988). Hand disinfection: a comparison of various agents in laboratory and ward studies. *Journal of Hospital Infection, 11*(3), 226–243.
- Banos, A., & Lacasa, J. (2007). Spatio-temporal exploration of SARS epidemic. *Cybergeo: European Journal of Geography, 408*.
- Beggs, C. B. (2003). The airborne transmission of infection in hospital buildings: fact or fiction? *Indoor and Built Environment, 12*(1–2), 9–18.
- Béghein, C., Jiang, Y., & Chen, Q. Y. (2005). Using large eddy simulation to study particle motions in a room. *Indoor Air, 15*(4), 281–290.
- Berlemont, A., Desjonqueres, P., & Gouesbet, G. (1990). Particle Lagrangian simulation in turbulent flows. *International Journal of Multiphase Flow, 16*(1), 19–34.
- Bourouiba, L., Dehandschoewercker, E., & Bush, J. W. M. (2014). Violent expiratory events: on coughing and sneezing. *Journal of Fluid Mechanics, 745*, 537–563.
- Chao, C. Y. H., Wan, M. P., Morawska, L., Johnson, G. R., Ristovski, Z. D., Hargreaves, M., Mengersen, K., Corbett, S., Li, Y., Xie, X., & Katoshevski, D. (2009). Characterization of expiration air jets and droplet size distributions immediately at the mouth opening. *Journal of Aerosol Science, 40*(2), 122–133.

- Deevy, M., Sinai, Y., Everitt, P., Voigt, L., & Gobeau, N. (2008). Modelling the effect of an occupant on displacement ventilation with computational fluid dynamics. *Energy and Buildings*, 40(3), 255–264.
- Dudalski, N., Mohamed, A. F. A., Savory, E., & Mubareka, S. (2018). Experimental measurements of far field cough airflows produced by healthy and influenza-infected subjects. In *Proceedings of the Canadian Society for Mechanical Engineering International Congress 2018*, Toronto, Canada.
- Duguid, J. P. (1944). The size and the duration of air-carriage of respiratory droplets and droplet-nuclei. *J Hyg*, 44, 471–479.
- Gupta, J. K., Lin, C. H., & Chen, Q. (2009). Flow dynamics and characterization of a cough. *Indoor Air*, 19(6), 517–525.
- Hai, W., Zhao, Z., Wang, J., & Hou, Z.-G. (2004). The short-term impact of SARS on the Chinese economy. *Asian Economic Papers*, 3(1), 57–61.
- Kannan, B. T. (2015). Computation of an axisymmetric jet using OpenFOAM. *Procedia Engineering*, 127, 1292–1299.
- Luk, J., Gross, P., & Thompson, W. W. (2001). Observations on mortality during the 1918 influenza pandemic. *Clinical Infectious Diseases*, 33(8), 1375–1378.
- Mohamed, A. F. A. (2017). *Experimental Measurements of Far Field Cough Airflows Produced by Healthy and Influenza-Infected Human Subjects*. M. E. Sc. Thesis, Department of Mechanical and Materials Engineering, The University of Western Ontario.
- Mohamed, A. F. A., Dudalski, N., Lin, W. E., Savory, E., & Mubareka, S. (2017). The far-field of coughs produced by healthy and influenza-infected human subjects. In *Physmod 2017 - International Workshop on Physical Modelling of Flow and Dispersion Phenomena*, École Centrale de Nantes, France.
- Morawska, L. (2006). Droplet fate in indoor environments, or can we prevent the spread of infection? *Indoor Air*, 16(5), 335–347.

- Ostrowsky, B. (2007). Epidemiology of healthcare-associated infections. In W. R. Jarvis (Ed.), *Bennett and Brachman's Hospital Infections* (5th ed, pp. 3–24). Philadelphia: Lippincott Williams & Wilkins.
- Savory, E., Lin, W. E., Blackman, K., Roberto, M. C., Cuthbertson, L. R., Scott, J. A., & Mubareka, S. (2014). Western cold and flu (WeCoF) aerosol study – preliminary results. *BMC Research Notes*, 7(1), 563.
- Wei, J., & Li, Y. (2017). Human cough as a two-stage jet and its role in particle transport. *PLoS ONE*, 12(1), 1–15.
- World Health Organization (WHO). (2003). Severe acute respiratory syndrome (SARS): status of the outbreak and lessons for the immediate future. *Communicable Disease Surveillance and Response*, 1–10.
- Xie, X., Li, Y., Chwang, A. T. Y., Ho, P. L., & Seto, W. H. (2007). How far droplets can move in indoor environments - revisiting the Wells evaporation-falling curve. *Indoor Air*, 17(3), 211–225.
- Xu, G., & Antonia, R. A. (2002). Effect of different initial conditions on a turbulent round free jet. *Experiments in Fluids*, 33(5), 677–683.
- Yang, S., Lee, G. W. M., Chen, C.-M., Wu, C.-C., & Yu, K.-P. (2007). The size and concentration of droplets generated by coughing in human subjects. *Journal of Aerosol Medicine*, 20(4), 484–494.
- Zhang, L., & Li, Y. (2012). Dispersion of coughed droplets in a fully-occupied high-speed rail cabin. *Building and Environment*, 47(1), 58–66.
- Zhu, S., Kato, S., & Yang, J.-H. (2006a). Investigation into airborne transport characteristics of airflow due to coughing in a stagnation indoor environment. *ASHRAE Transaction Research*, 112, 123–133.
- Zhu, S., Kato, S., & Yang, J.-H. (2006b). Study on transport characteristics of saliva droplets produced by coughing in a calm indoor environment. *Building and Environment*, 41(12), 1691–1702.

Chapter 2

2 CFD Modelling of the Flow Field of Coughing

2.1 Introduction

Coughing is one of the common forced expiratory activities which play a key role in transmitting airborne viruses of respiratory diseases in the indoor environment. Human cough flow is generally considered as a multiphase incompressible turbulent free jet flow which consists of a flow field as a continuous phase and the droplets as a discrete phase (Bourouiba et al., 2014). Several parameters, such as the mouth opening area, time-dependent expired flow rate, fluid flow direction, the ambient temperature and relative humidity (RH), affect the transport characteristics of human cough flow and are not unique due to the physiological variability for different people (Gupta et al., 2009). The schematic description of the flow field of coughing is illustrated in Figure 2.1.

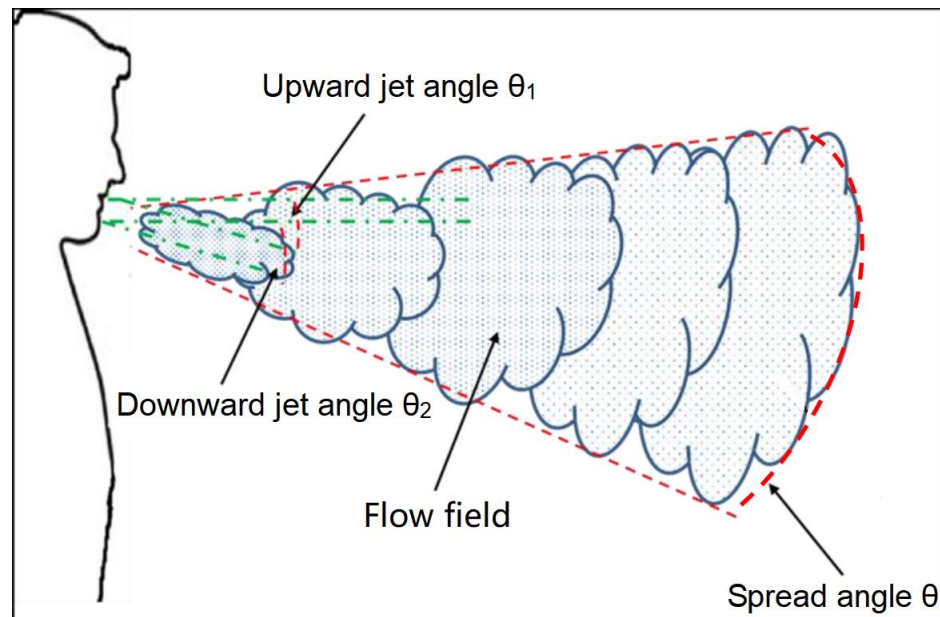


Figure 2.1: Schematic of the flow field of coughing (Mohamed, 2017 (with author's permission)).

2.1.1 Dynamic characteristics of turbulent free jet flows

In order to clearly recognize the complicated structures and to easily understand the phenomenon of human cough flow, the flow field is sometimes approximated as a turbulent round free jet (Xie et al., 2007), which is regarded as the simplest form of turbulent jets. A steady turbulent free jet is defined as a jet flow that is issued from a nozzle exit into an environment with the same fluid, which can be quiescent or have a velocity, and propagates freely without any effect of the solid boundaries (Bisoi et al., 2017). This type of flow is of great interest for a variety of practical engineering applications, such as chemical processes, combustion and pollutant discharge, as well as mixing, cooling and drying processes (Abdel-Rahman, 2010). Figure 2.2 shows the schematic description of a steady round free jet, in which there are three different regions depending on the streamwise distance to the nozzle exit: the near-field (initial region), the intermediate-field (transition region), and the far-field (fully-developed region). The near-field is usually referred to the region of $0 \leq x/d \leq 6$ (x and d indicate the distance in streamwise direction and the diameter of the round nozzle exit, respectively), and is also named as the potential core zone. In this region, the flow characteristics are almost the same as those at the nozzle exit and are not influenced by the growing annular shear layer (Gohil et al., 2014), where most of the mixing and interactions between the jet flow and the ambient fluid take place. The intermediate-field is located at the region of $6 \leq x/d \leq 30$, also known as the interaction zone. The near- and intermediate-fields together constitute the developing region, which normally dominates the dynamic performance in the far-field and the practical applications of a turbulent jet due to the significant impact of the upstream conditions on mass, momentum and heat transfer (Abdel-Rahman, 2010). The far-field is the region of approximately $x/d \geq 30$ (Fielder, 1998), and is also known as the self-similar or fully-developed region. Most interest has been concentrated on the far-field state because eventually it will be achieved by all the turbulent jets, for which the dynamic behaviour is simpler to characterize. Furthermore, a virtual origin is illustrated in Figure 2.2, which is defined as the intersection of two boundary lines of the jet flow (Flora & Goldschmidt, 1969). It is different from the nozzle exit and might be located inside or outside the nozzle. The location of the virtual origin (X_0) depends on the conditions of the jet flow at the nozzle exit (Mi & Nathan, 2009). Figure 2.2 also shows clearly that as the jet flow spreads

downstream, the velocity profile in the radial direction keeps changing, and the most significant velocity gradient occurs at the shear layer. As shown in Figure 2.2, the velocity along the centreline of the jet flow is known as the centreline velocity u_c , and r_u is called the half-width, which is defined as the distance between the centreline and a radial plane where the mean flow velocity U_0 is half the corresponding centreline velocity u_c (Darisse et al., 2013). The half-width r_u generally grows in a linear trend with a slope named the spreading rate, in the streamwise direction. Throughout the process of the jet propagation, the large eddies decompose into smaller and smaller eddies with turbulence structures decaying and the molecular viscous force being more dominant, whilst energy transfers from the large-scale turbulence structures to smaller structures. The processes of vortex formation and energy transfer are vital for the entrainment and mixing of the ambient environment, and it is noteworthy that with the shear layer becoming thicker, the vortex formation becomes weaker. Shinnee et al. (2008) and Matsuda and Sakakibara (2005) investigated the near-field region of turbulent round free jets in order to study the impacts of the entrainment and mixing caused by the vortical structures on the jet flow development, and found that the large-scale turbulence structures dominated the dynamic development of the jet flow.

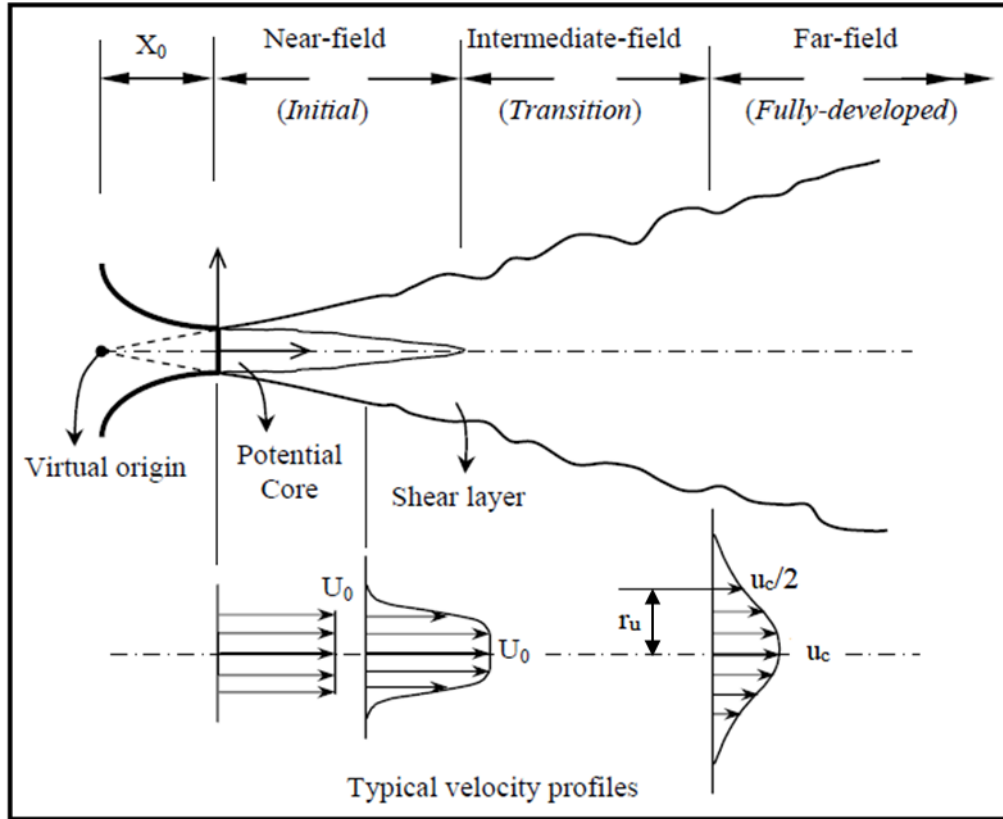


Figure 2.2: Schematic structures of a steady turbulent round free jet (adapted from Abdel-Rahman (2010)).

Studies on turbulent round free jets focus on two main parts, which include the effects of the inlet boundary conditions and the ambient conditions on the flow dynamic characteristics in the developing and fully-developed regions. The mean velocity profile, turbulence intensity and Reynolds number at the nozzle exit are commonly defined as the inlet boundary conditions for a turbulent free jet. The dynamic performance of free jet flows is also dependent on the ambient conditions including the absence or presence of walls around the flows, the temperature, the RH and backflow turbulence intensity of the ambient environment. Quinn (2006) examined an isothermal, incompressible turbulent free round jet with two types of nozzle exit, a sharp-edged orifice and a contoured nozzle. From his study, it was inferred that, the mean velocity profile had a saddle-backed shape at the sharp-edged orifice, and a top-hat shape at the contoured nozzle. It was found the mean velocity profile at the near-field region, including the nozzle exit, is affected by the vena contracta phenomenon (Ghahremanian & Moshfegh, 2013) which describes a short

increase of the streamwise mean velocity and occurs just downstream of the nozzle exit (Mi et al., 2001a & Mi et al., 2001b). Xu and Antonia (2002) also conducted experiments on free jet flows injected from a pipe and a conventional contraction to investigate the influences of different types of nozzle exit on the jet flow development, and demonstrated that for the pipe jet, the large-scale turbulence structures formed much farther downstream, and the jet flow reached the far-field region much slower, compared to the contraction jet. Therefore, it can be concluded that the geometric shape of the nozzle exit affects the turbulence structures in both near- and far-field regions, and the impact of the geometric shape of the nozzle exit is more significant on the near-field structures.

In order to examine the effect of the Reynolds number at the nozzle exit on the dynamic characteristics of turbulent free jet flows, several studies were carried out by employing different experimental techniques (Dowling & Dimotakis, 1990; Pitts, 1991; Kwon & Seo, 2005). It was found that in the near-field region, the exit Reynolds number had a strong influence on several turbulence characteristic parameters, where it should be emphasized that the larger the exit Reynolds number, the more significant the influence. However, the flow development was found to be almost independent of the exit Reynolds number. Similarly, the effect of the velocity profile at the nozzle exit on the free jet flow behaviour was also investigated experimentally (Richards & Pitts, 1993 & Ferdman et al., 2000) where it was concluded that compared with the far-field region, the near-field behaviour is affected much more severely by the velocity profile at the exit of the nozzle.

To sum up, compared with the near-field region of turbulent free jet flows, more interest was focused on the far-field region (Abdel-Rahman, 2010). However, conflicting results regarding the effects of the inlet boundary conditions on far-field characteristics exist. Some works supported that the dynamic development in far-field region of all the jet flows was identical and independent of the inlet boundary conditions, i.e. universal self-similarity (Antonia & Zhao, 2001; Pitts, 1991; Dowling & Dimotakis, 1990; Richards & Pitts, 1993), while other works claimed that the far-field development was not universal, and was strongly dependent on the inlet boundary conditions (Mi et al., 2001; George, 1989; Boersma et al., 1998).

2.1.2 Numerical studies on turbulent free jet flows

When examining human cough flow, it is useful to first analyze the characteristics of turbulent free jets, since the flow field of coughing will fall in this general category of flows. Many numerical studies have been carried out to computationally characterize the dynamic behaviour of such flows. The Reynolds Averaged Navier-Stokes (RANS) approach is one of the most popular methods available in the computational fluid dynamics (CFD) simulations because it can be used to model different types of flows, and has a lower computation cost than other approaches (Smith et al., 2004). Belonging to the RANS approach, various turbulence models are available to account for the effect of turbulent random motions of the fluid, including zero-equation model (mixing length model), one-differential-equation model (Spalart-Almaras model), two-differential-equation models (standard, realizable and renormalization group (RNG) $k-\varepsilon$ models and standard, baseline and shear stress transport (SST) $k-\omega$ models) and seven-differential-equation model (Reynolds stress model (RSM)). Chang and Lin (1989) developed a numerical methodology using the mixing length model (Prandtl, 1925) to simulate a free jet flow, and found that the mixing length model over-predicted some of the turbulence parameters, such as the spreading rate and mean velocity, compared with the experimental data (Rodi, 1972). Kannan (2015) applied the standard $k-\varepsilon$ model to numerically investigate the dynamic development of a turbulent free jet and validated the results with the experimental work of Panchapakesan and Lumley (1993). It was demonstrated that the standard $k-\varepsilon$ model also over-predicted some turbulence quantities, which was caused by the dissipation (Kannan, 2015). Other turbulence models such as the realizable $k-\varepsilon$ model, the SST $k-\omega$ model and the RSM were also examined to predict the performance of turbulent free jet flows (Shih et al., 1995; Ghahremanian & Moshfegh, 2013; Pérez et al., 2005; Kannan et al., 2009).

There is a universal problem for most RANS turbulence models in the prediction of the far-field behaviour of turbulent free jet flows, which is named the round-jet/plane-jet anomaly (Ghahremanian & Moshfegh, 2013). Based on the finding for planar jet flows, the prediction of the spreading rate is reasonable, but for axisymmetric jet flows, the spreading rate is estimated unsatisfactorily. Furthermore, the process of vortex stretching, which is the primary mechanism of energy transfer from large-scale to small-scale eddies, is absent

in most RANS turbulence models (Ghahremanian & Moshfegh, 2013). Compared with the RANS approach, the large eddy simulation (LES) method gives a more accurate prediction by resolving large turbulence scales of free jet flows. However, numerical studies of such flows by applying the LES method are very limited due to the huge computational cost. Di Venuta et al. (2018) presented a numerical study of a free jet of air with different Reynolds numbers by using the LES method and compared their results with the experimental data obtained from both the particle image velocimetry (PIV) and hot film anemometry (HFA) techniques (Gori et al., 2013 & Gori et al., 2014). The numerical results showed a remarkably good agreement to the experimental data in both the instantaneous and mean velocity fields, which strongly validated the effectiveness of the LES method in prediction of turbulent free jet flows. Cetin et al. (2017) computationally explored the effect of the inlet boundary conditions on dynamic characteristics of free jets by applying the LES approach, and demonstrated a significant dependence of the near-field behaviour on the inlet boundary conditions, which was also inferred in some experimental studies (Antonia & Zhao, 2001, Pitts, 1991, Dowling & Dimotakis, 1990 & Richards & Pitts, 1993). Bisoi et al. (2017) presented detailed turbulence characteristics, such as the formation of vortical and coherent structures and energy transfer, of a 3-dimensional turbulent free jet obtained from the LES simulation, as well as compared the velocity field with that from other numerical works using the direct numerical simulation (DNS) method (Stanley et al., 2002 & Klein et al., 2003). Gohil et al. (2014) performed a LES simulation on a round free jet and analyzed the development of flow structures. The dynamic characteristics of the jet flow, including the velocity variation and turbulence parameters, in both the near- and far-field regions were compared with the experimental data in the literature and the comparison showed a reasonable agreement. Some other numerical works also investigated the effect of the Reynolds number at the nozzle exit as well as other inlet boundary conditions on the behaviour of turbulent free jet flows using the LES method (Ranga Dinesh et al., 2010, Bogy & Bailly, 2006 & Kim & Choi, 2009).

The flow field of coughing is often approximated as a turbulent free air jet ejected from the mouth opening, which is regarded as a round nozzle exit, into a quiescent environment with air. In this case, numerical works of turbulent free jet flows are instructive to investigate the dynamic characteristics of the flow field of coughing. Among the available

CFD methods, the RANS approach is less time-consuming for the simulation, and there are various turbulence models to select. Therefore, it has become the most popular method to model jet flows. Compared to the RANS approach, the LES method predicts the development of jet flows more accurately since it resolves the large turbulence scales and only models the small scales through the subgrid-scale (SGS) turbulence model. However, previous numerical works applying the LES method are limited due to the high computational cost, and none of the works provides the comparison between the jet flow predictions using the RANS and LES approaches. More importantly, human cough is actually a transient phenomenon, which means that the dynamic characteristics of the cough flow are varying with time (Piirilä & Sovijärvi, 1995 & Bucher, 1958), so a steady-state turbulent round free jet flow is not able to characterize the transient development of the human cough flow. Therefore, a study is carried out in the present work to numerically investigate the flow field of coughing by both the unsteady RANS (i.e. URANS) and LES methods for comparison purposes. The SST $k-\omega$ model is used with the URANS approach, and the dynamic Smagorinsky-Lilly model is employed as the SGS model in the LES method. The experimental measurements obtained from the PIV and the hot-wire anemometry (HWA) techniques (Dudalski et al., 2018 & Mohamed, 2017) and the work of Wei & Li (2017) are used to validate the numerical results.

2.2 Numerical Methodology

The evolution of the flow field of coughing is time-dependent. So, the dynamic characteristics, including the velocity field and turbulence parameters, are varying with time. Therefore, the CFD simulations in the present study are conducted under a transient condition. Both the URANS and LES simulations employ the same computational domain and grid, time step as well as the boundary and ambient conditions, in order to maintain consistency for a fair comparison.

2.2.1 Governing equations

2.2.1.1 The URANS approach

The URANS approach is based on the Reynolds-averaged Navier-Stokes equations, of which the velocity component is decomposed as:

$$u_i = \bar{u}_i + u'_i \quad (2.1)$$

where \bar{u}_i and u'_i ($i=1, 2, 3$) represent the mean and fluctuating velocity components, respectively. The mass and momentum conservation equations are obtained by taking an ensemble average for flow variables in the instantaneous equations, and are written as:

$$\frac{\partial \rho}{\partial t} + \frac{\partial}{\partial x_i} (\rho \bar{u}_i) = 0 \quad (2.2)$$

$$\frac{\partial}{\partial t} (\rho \bar{u}_i) + \frac{\partial}{\partial x_j} (\rho \bar{u}_i \bar{u}_j) = -\frac{\partial p}{\partial x_i} + \frac{\partial}{\partial x_j} \left[\mu \left(\frac{\partial \bar{u}_i}{\partial x_j} + \frac{\partial \bar{u}_j}{\partial x_i} - \frac{2}{3} \delta_{ij} \frac{\partial \bar{u}_l}{\partial x_l} \right) \right] + \frac{\partial (-\rho \overline{u'_i u'_j})}{\partial x_j} \quad (2.3)$$

where ρ is the density, p is the pressure, and μ is the molecular viscosity of the injected fluid, which is the mixture of air and water vapour, and x_i represents the Cartesian coordinates. The term of $-\rho \overline{u'_i u'_j}$ represents the turbulent Reynolds stress, which describes the effect of fluctuations on the flow, and must be modelled to close Eqn. (2.3) (ANSYS, 2013). The Boussinesq hypothesis (Hinze, 1975) is used, as shown in the following equation.

$$-\rho \overline{u'_i u'_j} = \mu_t \left(\frac{\partial \bar{u}_i}{\partial x_j} + \frac{\partial \bar{u}_j}{\partial x_i} \right) - \frac{2}{3} \left(\rho k + \mu_t \frac{\partial \bar{u}_k}{\partial x_k} \right) \delta_{ij} \quad (2.4)$$

where μ_t is the turbulent viscosity, which is related to the turbulent kinetic energy (k) and its dissipation rate (ε) by,

$$\mu_t = \rho C_\mu \frac{k^2}{\varepsilon} \quad (2.5)$$

where C_μ is a constant with the value of 0.09, and k and ε are obtained by a turbulence model.

The selection of the turbulence model depends on several factors, including the advantages and limitations of the model, the required time and accuracy of the prediction, the physics of the specific flow as well as the consideration with regard to previous numerical studies of the similar problem (Ghahremanian & Moshfegh, 2013). The SST $k-\omega$ model by Menter (1994) combines the capabilities of both $k-\varepsilon$ and $k-\omega$ models, i.e. the freestream independence in the far-field region of the $k-\varepsilon$ model and robust formulation in the near-wall region of the $k-\omega$ model by transforming the governing equations of the $k-\varepsilon$ model into

a form of k - ω model (ANSYS, 2013). The SST k - ω model is more reliable in the prediction of a wide variety of flows, including free jets, airfoils, adverse pressure gradient flows and transonic shock waves, than standard k - ω model (Pérez et al., 2005 & Ghahremanian & Moshfegh, 2013). Therefore, the SST k - ω model is employed to predict the flow field of coughing in this study.

The governing equations of the SST k - ω model (Menter, 1994) are shown below,

$$\frac{\partial}{\partial t}(\rho k) + \frac{\partial}{\partial x_i}(\rho k \bar{u}_i) = \frac{\partial}{\partial x_j} \left(\Gamma_k \frac{\partial k}{\partial x_j} \right) + G_k - Y_k \quad (2.6)$$

$$\frac{\partial}{\partial t}(\rho \omega) + \frac{\partial}{\partial x_j}(\rho \omega \bar{u}_j) = \frac{\partial}{\partial x_j} \left(\Gamma_\omega \frac{\partial \omega}{\partial x_j} \right) + G_\omega - Y_\omega + D_\omega \quad (2.7)$$

where G_k and G_ω are the production terms of turbulent kinetic energy (k) and specific dissipation rate (ω), Γ_k and Γ_ω are the effective diffusivity coefficients of k and ω , and Y_k and Y_ω are the dissipation terms of k and ω , respectively. The D_ω represents the damped cross-diffusion derivative term. The above terms are expressed as the following equations. More details about the governing equations of the SST k - ω turbulence model are shown in Appendix B.

Table 2.1: Governing equations of the SST k - ω turbulence model.

Term	Governing equation	Equation number
G_k	$G_k = -\rho \overline{u'_i u'_j} \frac{\partial \bar{u}_j}{\partial x_i}$	(2.8)
G_ω	$G_\omega = \alpha \frac{\omega}{k} G_k$	(2.9)
Γ_k	$\Gamma_k = \mu + \frac{\mu_t}{\sigma_k}$	(2.10)
Γ_ω	$\Gamma_\omega = \mu + \frac{\mu_t}{\sigma_\omega}$	(2.11)
Y_k	$Y_k = \rho \beta^* f_\beta k \omega$	(2.12)
Y_ω	$Y_\omega = \rho \beta f_\beta \omega^2$	(2.13)
D_ω	$D_\omega = 2(1 - F_1) \rho \frac{1}{\omega \sigma_{\omega,2}} \frac{\partial k}{\partial x_j} \frac{\partial \omega}{\partial x_j}$	(2.14)

2.2.1.2 The LES approach

In recent CFD studies, the LES and DNS approaches have become more and more popular and feasible due to the development of computational processing techniques (Ranga Dinesh et al., 2010). Both these two numerical methods are able to resolve turbulence scales in a specific type of flow and, therefore, provide more accurate predictions than the URANS approach. In the DNS method, the whole range of time and length scales of turbulence are resolved directly and turbulence is not modelled. However, the required computational expense is highly related to the turbulent Reynolds number Re_t (ANSYS, 2013), where it should be emphasized that the higher the Reynolds number of the flow, the higher the computational cost it demands. Hence, this causes the applications of the DNS method to be very limited. While the LES approach computes the large turbulence scales directly and only models the small scales through the SGS model, therefore, falls between the URANS and DNS methods with respect to the fraction of resolved turbulence scales. It is assumed that the large eddies transport most of the energy, mass and momentum, and their scale dimensions are solely dependent on flow geometry and boundary conditions imposed, while the small eddies tend to be more universal and isotropic and, hence, less dependent on flow geometry. Compared with the DNS, the LES approach can predict flows with higher Reynolds numbers using much less computational time and, therefore, it has become more extensively employed.

The basic principle of the LES method is to separate and resolve the large eddies that contain most of the energy through the spatially-filtered mass and momentum equations (Navier-Stokes equations), defined as

$$\frac{\partial \tilde{u}_i}{\partial x_i} = 0 \quad (2.15)$$

$$\frac{\partial \tilde{u}_i}{\partial t} + \tilde{u}_j \frac{\partial \tilde{u}_i}{\partial x_j} = -\frac{1}{\rho} \frac{\partial \tilde{p}}{\partial x_i} + \nu \frac{\partial^2 \tilde{u}_i}{\partial x_j^2} - \frac{\partial \tau_{ij}}{\partial x_j} \quad (2.16)$$

where τ_{ij} represents the SGS stress tensor, describing the impact of small turbulence scales, and is expressed as

$$\tau_{ij} = \widetilde{u_i u_j} - \tilde{u}_i \tilde{u}_j \quad (2.17)$$

It is noteworthy that the filtered Navier-Stokes equations are similar to those of the URANS model. However, the integration is in space (spatial-filtering) and not over time (time-averaging) as in the case of the URANS model (Salim et al., 2011).

The SGS stress results in the exchange of momentum between the large (resolved) and small (subgrid) scales of motion (Bisoi et al., 2017), and needs to be modelled. Belonging to the LES approach, various SGS turbulence models are available, including the dynamic kinetic energy SGS model (Kim & Menon, 1997), the Smagorinsky-Lilly model (Smagorinsky, 1963 & Lilly, 1992), the Wall-Adapting Local Eddy-Viscosity (WALE) model (Nicoud & Ducros, 1999) and the dynamic Smagorinsky-Lilly model (Germano et al., 1991 & Lilly, 1992). In the present study, the dynamic Smagorinsky-Lilly model is adopted to model the SGS stress. This model considers the Smagorinsky model constant, C_S , as a function of space and time over a fairly wide range in order to avoid the damping of turbulent fluctuations in the presence of mean shear and in transitional flows (ANSYS, 2013). More details about the dynamic Smagorinsky-Lilly model are shown in Appendix C.

2.2.1.3 Energy equation

In order to solve the heat transfer between the cough flow and the ambient environment, the energy equation is required and is in the following form (Nijemeisland & Dixon, 2004),

$$\frac{\partial(\rho e)}{\partial t} + \nabla \cdot (\vec{u} \rho e) = \nabla \cdot (k_{eff} \nabla T - \sum_j \vec{J}_j \int_{T_{ref}}^T c_{p,j} dT) \quad (2.18)$$

where e represents the total energy, and is given as the following equation.

$$e = h + \frac{u^2}{2} \quad (2.19)$$

where h , p , ρ and u are the sensible enthalpy, pressure, density and velocity of the injected fluid, respectively.

The details about the energy equation are shown in Appendix D.

2.2.2 Computational domain and grid

In order to compare with the experimental data, a 3-dimensional computational domain used for the simulations is generated with the same dimensions as the experimental cough chamber, named as FLUGIE (Fluids from Undergrads with Influenza Enclosure), in which the PIV and HWA techniques are used to carry out the measurements by the author's colleagues (Dudalski et al., 2018 & Mohamed, 2017). The details about the FLUGIE chamber is shown in Appendix E.

The computational domain is in a cuboid shape and is illustrated as Figure 2.3, in which the “x”, “y” and “z” axes represent the axial (streamwise), lateral and vertical directions, respectively. The inlet is a circular orifice of diameter $d=0.0217$ m, representing the average human mouth diameter (Gupta et al., 2009). The centre of the inlet is denoted by $(0, 0, 0)$, which is also the origin of the coordinate system.

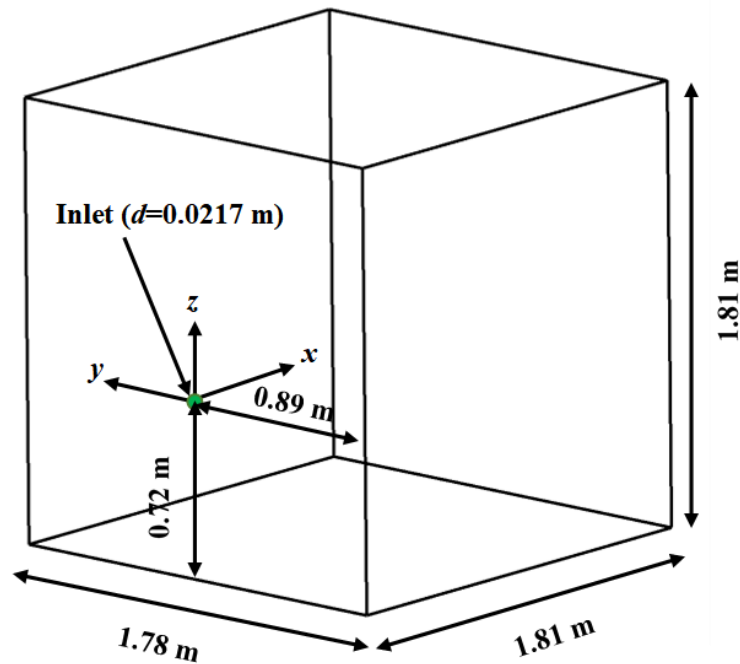


Figure 2.3: Schematic of the computational domain along with its dimensions.

The computational domain and grid are generated by using ICEM CFD 16.0. Irregular unstructured polyhedral grids are implemented to reduce the computational expense

without lowering the accuracy and to improve the residual convergence. To characterize the dynamic development of the flow field of coughing more effectively, the grids are created in non-uniform sizes, as exhibited in Figure 2.4, where it can be clearly seen that the grid in the cone region is much finer than that in the global region (outside of the cone region). Since the flow field spreads in the cone region with higher velocity gradients, the finer grid is used to predict the dynamic characteristics more accurately by capturing more details from the smaller computational cells. Both the URANS and LES simulations employ the same computational grid resolution, which is 1 mm at the inlet and 5 mm in the cone region with the global growing ratio of 1.15. The total number of computational cells is approximately 7.3 million. The grid independence tests for both the URANS and LES simulations are shown in Appendix H.

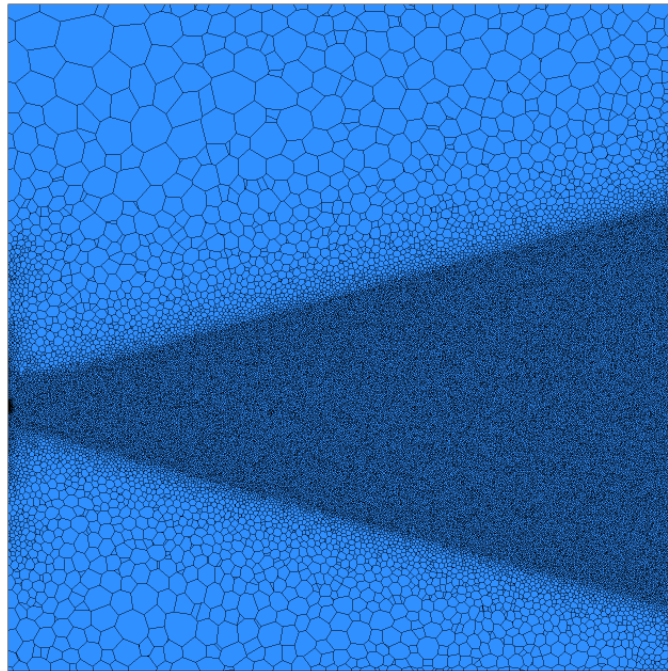


Figure 2.4: Grid distribution on the x - z plane ($y=0$) of the computational domain.

2.2.3 Boundary and ambient conditions

The numerical prediction of the dynamic characteristics of the flow field of coughing is affected by the boundary conditions, which should closely match the physical reality. In

the present study, conditions acting on the inlet, six walls of computational domain, as well as the ambient environment need to be specified.

The transient velocity profile imposed at the inlet is implemented as the inlet boundary condition to account for the time-dependent velocity of the flow at the human mouth (Gupta et al., 2009). The velocity direction is set as normal to boundary, which satisfies that the fluid is issued from the inlet into the domain with the velocity in the streamwise direction. The profile of the time-dependent velocity imposed at the inlet is shown as Figure 2.5. It can be seen that the flow field lasts 0.61 *secs* with the peak velocity u_{ip} (around 22.06 *m/s*) occurring at $t_{ip}=0.066$ *secs*. Based on Zhu et al. (2006), the temperature and turbulence intensity at the inlet are defined as 32 °C (305.15 K) and 10% of the temporal mean inlet velocity u_m , respectively, and u_m is calculated by the following equation (Wei & Li, 2017),

$$u_m = \frac{1}{t_{iss}} \int_0^{t_{iss}} u(t) dt \quad (2.20)$$

where t_{iss} represents the cough duration, which is 0.61 *secs*. In the present study, u_m is 8.808 *m/s*, and the mean flow Reynolds number is 13,084, which indicates that the onset of the injected flow is fully turbulent in nature. The hydraulic diameter is set as 0.0217 m, which is equal to the average human mouth diameter (Gupta et al., 2009). For the LES approach, the spectral synthesizer algorithm (Kraichnan, 1970 & Smirnov et al., 2001) is selected to generate the synthetic turbulence at the inlet, through creating a velocity vector field without divergence from the summation of 100 Fourier harmonics (ANSYS, 2013).

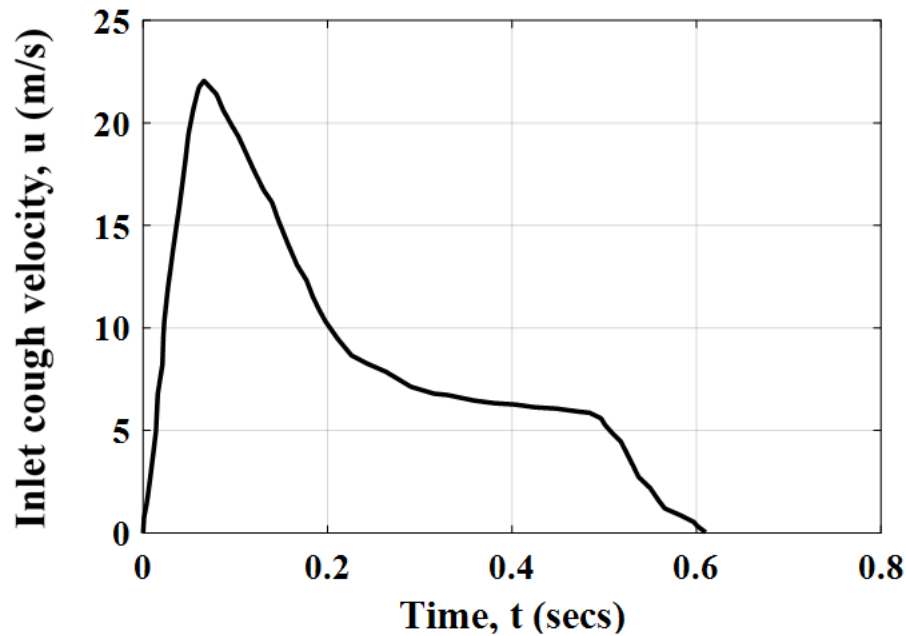


Figure 2.5: Inlet transient velocity profile (reproduced from Gupta et al. (2009)).

All the six walls of the computational domain are defined as no-slip adiabatic walls. For the ambient conditions, the temperature is set as 21.5°C (294.65 K) and the mass fraction of water vapour is 0.8% based on 50% RH, which is considered to be in the range of thermal comfort level (Balaras et al., 2007). The surrounding fluid velocity is set as zero due to the quiescent ambient condition. The fluid injected from the inlet is defined as two-species alveolar air, which is usually considered as the flow caused by human expiratory activity, e.g. coughing, breathing, speaking and sneezing. The two species include air and water vapour, with the mole fraction 93.8% and 6.2%, respectively (Saladin, 2003). The properties of the injected fluid are shown in Appendix F.

2.2.4 CFD solver

The commercial CFD packages, FLUENT 16.0 is used to carry out the simulation and CFD-Post 16.0 is used to post-process the results. A finite volume method is employed to solve the governing equations with double precision. The pressure-based solver is adopted since it is suitable for incompressible flows. The pressure-based solver is conceived based on the projection method (Chorin, 1968) which satisfies the mass conservation of the velocity field via solving a pressure equation derived from the continuity and momentum

equations. The basic principle of the pressure-based solver is to repeatedly solve the entire set of governing equations, which are nonlinear and coupled to each other, for each iteration in the simulation process until the solution converges.

In the simulations using both the URANS and LES methods, the algorithm of the Semi-Implicit Method for Pressure-Linked Equations (SIMPLE) by Patankar et al. (1972), is employed as the pressure-velocity coupling method. Such an algorithm solves the velocity correction explicitly, while solving for the pressure correction and momentum equation implicitly, hence providing more accurate velocity corrections. Furthermore, the SIMPLE algorithm can obtain a converged solution with less computational time, and allow for larger time step sizes, i.e. Courant-Friedrichs-Lewy (CFL) number greater than 1, for an unsteady flow problem. For the pressure interpolation, the second-order scheme is used as it can acquire acceptable solutions for most cases (ANSYS, 2014), and for the gradient evaluation, the least squares cell-based scheme is performed in order to obtain a more accurate second-order interpolation on irregular unstructured polyhedral grids which are applied in the present study. To solve the temporal discretization, the bounded second order implicit formulation is carried out as it can provide a higher accuracy and better stability than other types of formulation. A time step size of 0.001 *secs* is used to reduce the computational expense. Both the URANS and LES simulations are run for 4 *secs* in total of the flow time which is sufficient to characterize the dynamic development of the flow field of coughing in the computational domain. The residual convergence criterion is set as 10^{-6} for the energy equation and 10^{-3} for the other governing equations, including continuity, momentum and species transport equations, etc., and a maximum number of iterations per time step, i.e. inner loop iterations, is set as 100.

For the URANS modelling, the third-order MUSCL (Monotone Upstream-Centred Schemes for Conservation Laws) algorithm (Van Leer, 1979) is used to solve the spatial discretization of momentum, turbulence parameters, i.e. turbulent kinetic energy and specific dissipation rate, water vapour species transport and energy. Such an algorithm can provide a higher spatial accuracy through lowering the numerical diffusion for all types of grids and is, therefore, the best choice for the URANS approach. For the LES modelling, the central differencing discretization scheme is performed for momentum, water vapour

species transport and energy since it minimizes the numerical diffusion and provides the highest accuracy in resolving the large turbulence scales. Therefore, it is considered as the ideal choice for the LES method.

2.3 Results and Discussion

In the following section, the numerical results are analyzed in terms of different dynamic characteristics of the flow field of coughing, including the velocity field, streamwise penetration and power spectral density. The comparison between the URANS and LES approaches are provided in different aspects and then the appropriate modelling method is taken into consideration for further numerical study. Results of the velocity field and power spectral density are validated by the experimental data from the PIV and HWA measurements (Dudalski et al., 2018 & Mohamed, 2017), whilst results regarding the streamwise penetration are compared with the experimental work of Wei & Li (2017).

2.3.1 Velocity field

2.3.1.1 Comparison of the results from the URANS and LES approaches

The contour of the velocity magnitude plays a very important role in numerically analyzing the velocity field of cough flow since it provides a clear visualization of the velocity variation with time, which makes the dynamic development of the flow field of coughing more graphic and easier to understand. The comparisons of the velocity magnitude contours at the x - z plane ($y=0$) between the URANS and LES approaches are shown in Figures 2.6-2.9, where the red cross symbol represents the centreline location of (1, 0, 0), and the black one denotes the point (1, 0, -0.22) where the hot-wire probe is located. The results at four different time steps, including 0.05 *secs*, 1 *sec*, 2 *secs* and 3 *secs*, are presented to illustrate the dynamic development of the flow field with time. From the figures, it is found that as time progresses, the contours from the two modelling approaches become very different. The velocity magnitude from the URANS approach varies symmetrically and regularly, which means that the flow field spreads in a uniform way, while the velocity magnitude from the LES approach has an irregular and non-uniform variation.

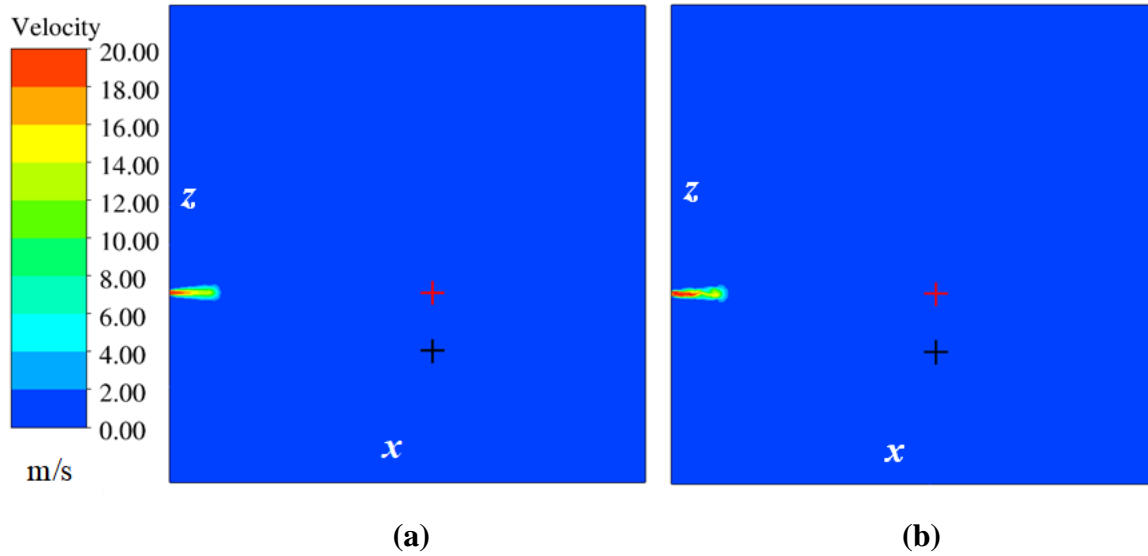


Figure 2.6: Contours of the velocity magnitude at $t = 0.05$ secs for (a) URANS method and (b) LES method. + is at $(1, 0, 0)$ and + is at $(1, 0, -0.22)$. The coordinates are in the unit of metres.

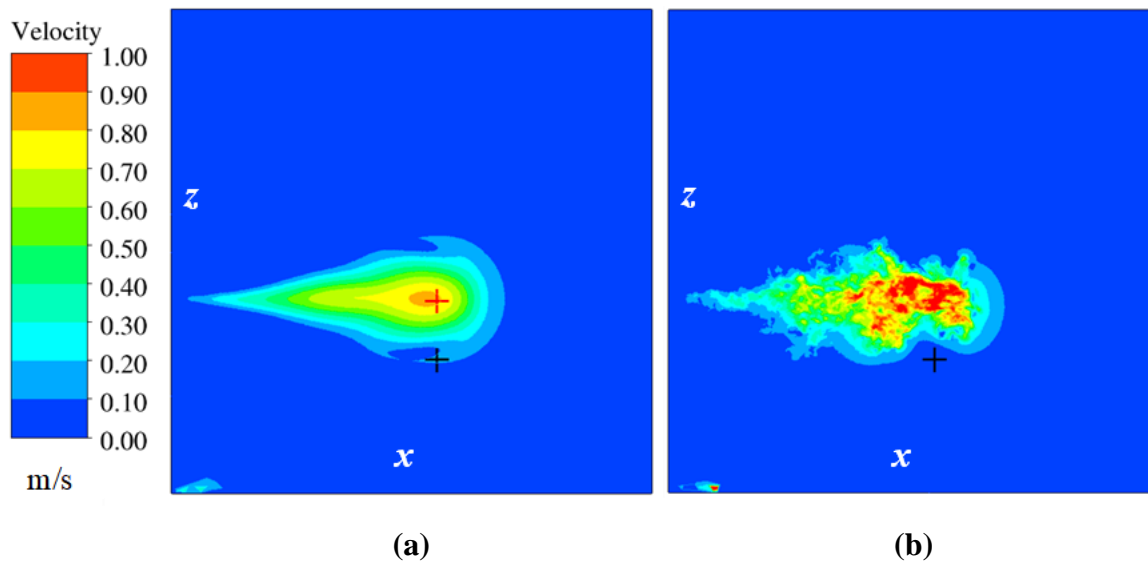


Figure 2.7: Contours of the velocity magnitude at $t = 1$ sec for (a) URANS method and (b) LES method.

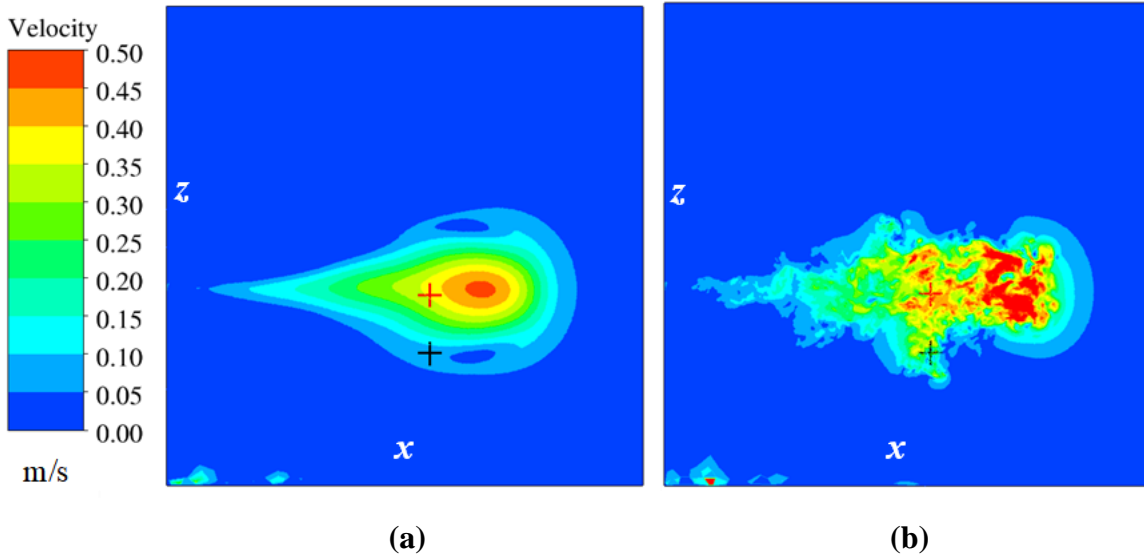


Figure 2.8: Contours of the velocity magnitude at $t = 2$ secs for (a) URANS method and (b) LES method.

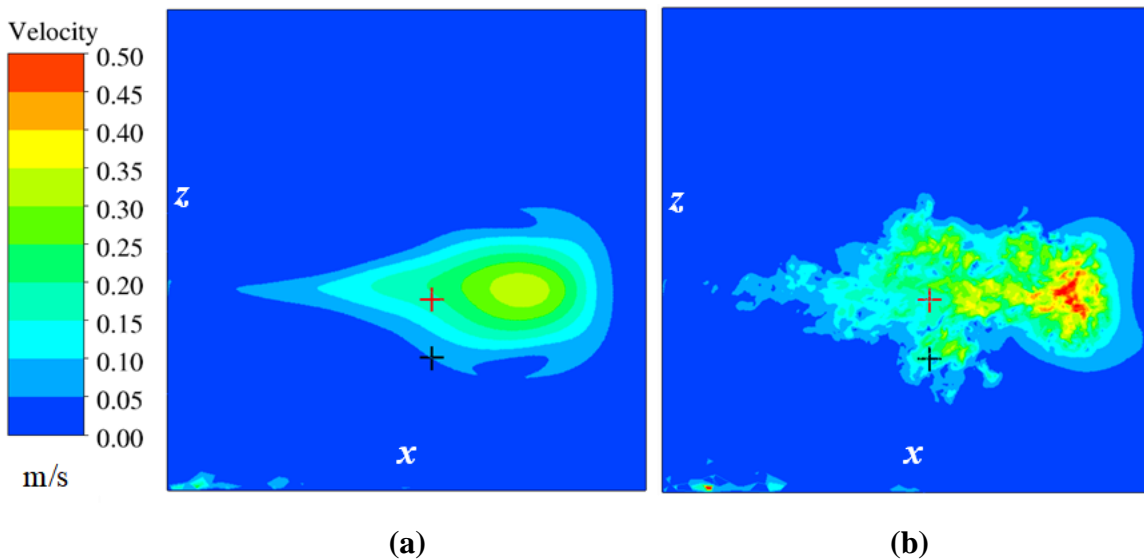


Figure 2.9: Contours of the velocity magnitude at $t = 3$ secs for (a) URANS method and (b) LES method.

2.3.1.2 Comparison with the experimental data from the PIV measurements

To validate the numerical model, the numerical results obtained from the LES approach are compared with the experimental data from the PIV measurements by Mohamed (2017).

The PIV system is a type of non-intrusive experimental technique which has been employed extensively to measure the 2-dimensional physical quantities in the research field of fluid mechanics. A sequence of instantaneous velocity magnitude contours generated from the PIV measurement, which is from one cough of a healthy human subject, are shown in Figure 2.10. The PIV technique gives a rectangular field of view with the dimension of 0.141 m in length and 0.340 m in width, and the data are obtained with a sampling frequency of 14.5 Hz, i.e. 0.069 *secs* of time step. The locations of (1, 0, 0) and (1, 0, -0.22) are denoted by two red cross symbols in the figure. It can be seen that during the time from 0.47-1.20 *secs*, the majority of the flow field of coughing falls in the region between the two given points. Although the human subject was required to cough horizontally, there was still a small angle between the centreline of the test chamber and the fluid flow direction, which is also known as the upward jet angle θ_I and is caused by the unawareness of the human subject. The effect of θ_I on the velocity field can be neglected as θ_I is very small, which is approximately 6.3° . To compare with the PIV measurement, the velocity magnitude contours obtained from the LES modelling are presented in Figure 2.11 with the field of view in the same dimension. Since the direction of the inlet velocity is set in the horizontal (streamwise) direction, $\theta_I = 0$. In order to account for θ_I in the presence of the PIV contour series, the points of (1, 0, 0) and (1, 0, -0.22) are shifted upward with the angle of 6.3° . It is found that the variation of the predicted instantaneous velocity magnitude is more concentrated in the region between the two given points, which infers that the cough flow predicted by the LES approach has a similar spread trend with that measured by the PIV technique and, hence, validates the effectiveness of the LES approach in predicting the variation of the velocity magnitude with time of the flow field of coughing.

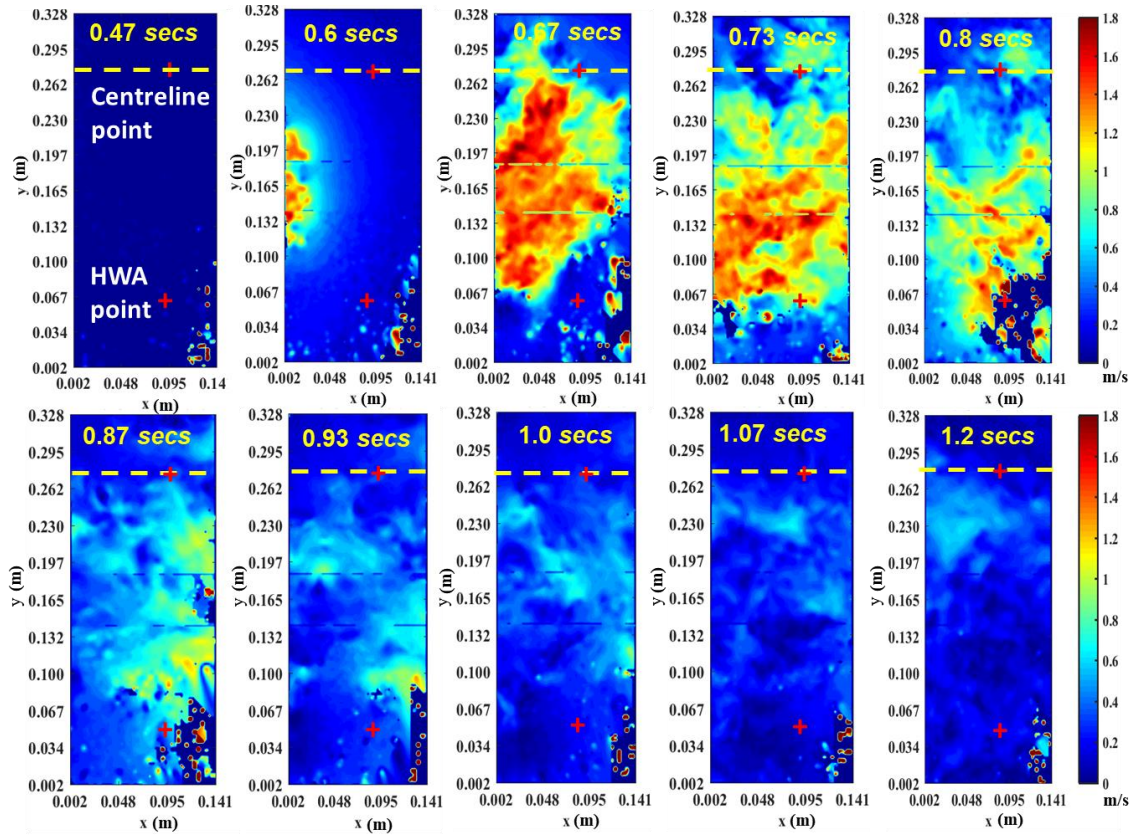


Figure 2.10: Time history of instantaneous velocity magnitude contours obtained from the PIV measurement (Mohamed, 2017 (with author's permission)).

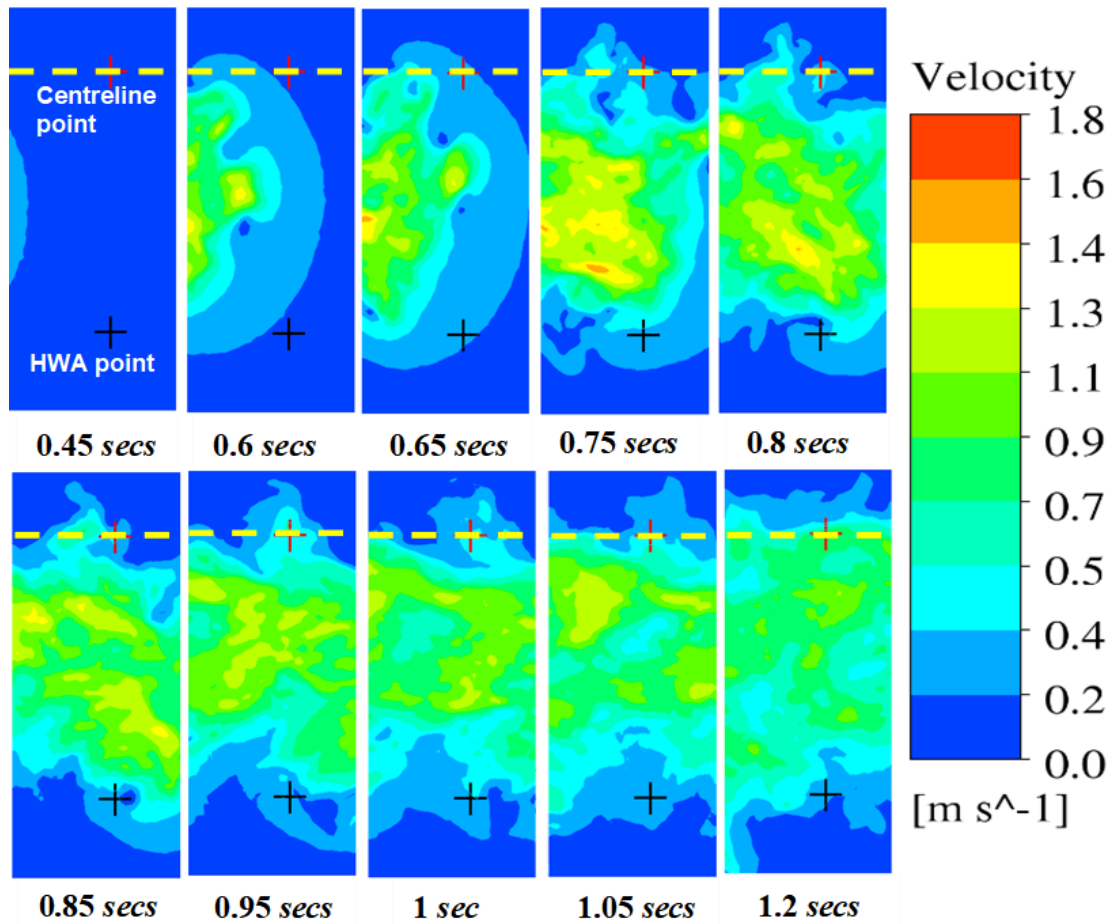


Figure 2.11: Time history of instantaneous velocity magnitude contours obtained from the LES modelling.

The experimental data obtained from the PIV measurements by Dudalski et al. (2018) are also used to validate the numerical results. A rectangular field of view with the dimensions of 0.09 m in length and 0.48 m in width was generated by the laser sheet, which is provided by the YAG double-pulsed laser system (Stamhuis, 2006), and is located 1 m downstream in the FLUGIE chamber (see Figure 2.12) in order to measure the 2-dimensional velocity vectors at the 1,836 sampling points in total that are evenly distributed on that PIV field of view.

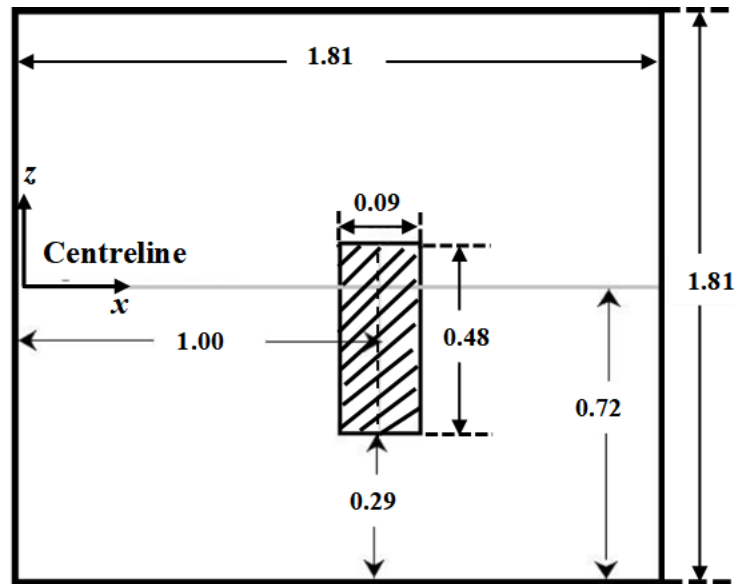


Figure 2.12: A schematic of the x - z plane ($y=0$) of the FLUGIE chamber with the PIV field of view (shaded part, all dimensions are in metres) (adapted from Dudalski et al. (2018)).

In the winter of 2018, 7 influenza-infected participants in total were recruited for the experimental studies and 13 sets of cough data were selected from the PIV measurements by Dudalski et al. (2018). The variation of the spatial average of 2-dimensional velocity magnitude with time of these 13 coughs is shown in Figure 2.13, where the numerical results obtained from the field of view with the same dimension and position are also provided for comparison. It is found that for the 13 coughs, the peak value of the spatially averaged velocity varies in the range 0.20-0.77 m/s, and for the LES and URANS modelling, the peak values are fairly close, which are 0.50 and 0.52 m/s, respectively.

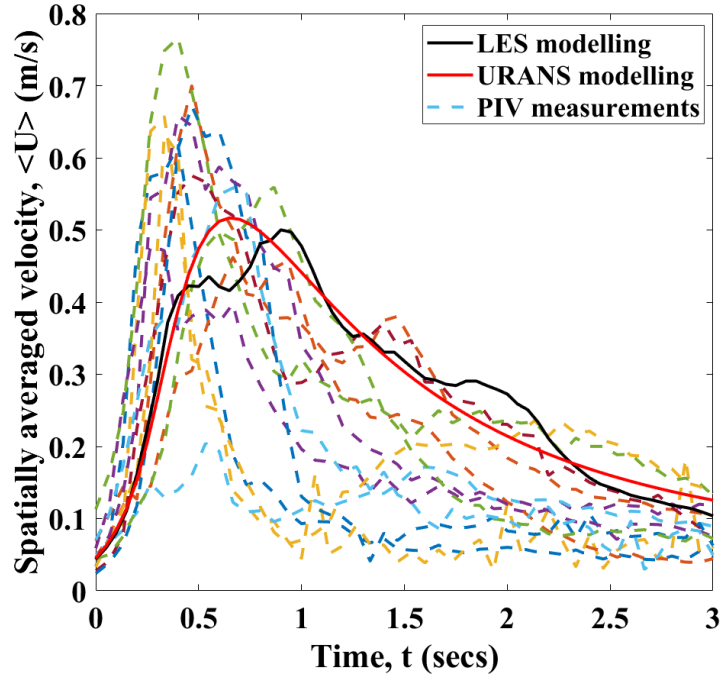


Figure 2.13: Comparison of the spatially averaged velocities between the numerical and PIV results on the PIV field of view.

Another comparison of the time history of 2-dimensional velocity magnitude at the midpoint, which is located 1 m downstream, of each cough flow is presented in Figure 2.14, where the PIV data are also obtained from the 13 coughs measured from the same participants as Figure 2.13 (Dudalski et al., 2018). To obtain a more generalized comparison for a better result analysis, the time history of the velocity magnitude is analyzed by employing a normalization algorithm for all the cough data and numerical results. The following equations are used for the normalization purpose,

$$U = \frac{u}{u_{1p}} \quad (2.21)$$

$$\tau = \frac{t}{t_{1p}} \quad (2.22)$$

where u and t represent the local instantaneous velocity magnitude and the corresponding time, whilst u_{1p} and t_{1p} are the initial peak velocity magnitude and the time when the peak occurs (Dudalski et al., 2018), respectively.

It is found from Figure 2.14 that the PIV profiles give a fluctuated trend of the velocity magnitude, which indicates that the flow field of coughing is a highly unsteady turbulent phenomenon. For the LES modelling, the profile also contains a lot of fluctuations, which is due to the unsteady instantaneous flow field of motion that the LES approach solves for. However, since the URANS approach considers the ensemble-averaged component of motion, the profile shows a smooth variation trend without any fluctuation. From Figure 2.14, it can also be seen that the profile obtained from the LES modelling closely resembles the PIV profiles, with the LES modelling providing more sampling points between the same two time steps, in compare to the PIV data. This is due to the difference in the sampling frequency employed for both the techniques; with the LES approach having a sampling frequency of 1000 Hz and the PIV technique having a sampling frequency of 14.5 Hz. Furthermore, from Figure 2.14, a secondary peak of the normalized velocity magnitude (U) is observed from the LES profile. This secondary peak has a similar value as the initial peak but occurs at a later time, which is not surprising as such secondary peaks are also observed from some of the PIV profiles.

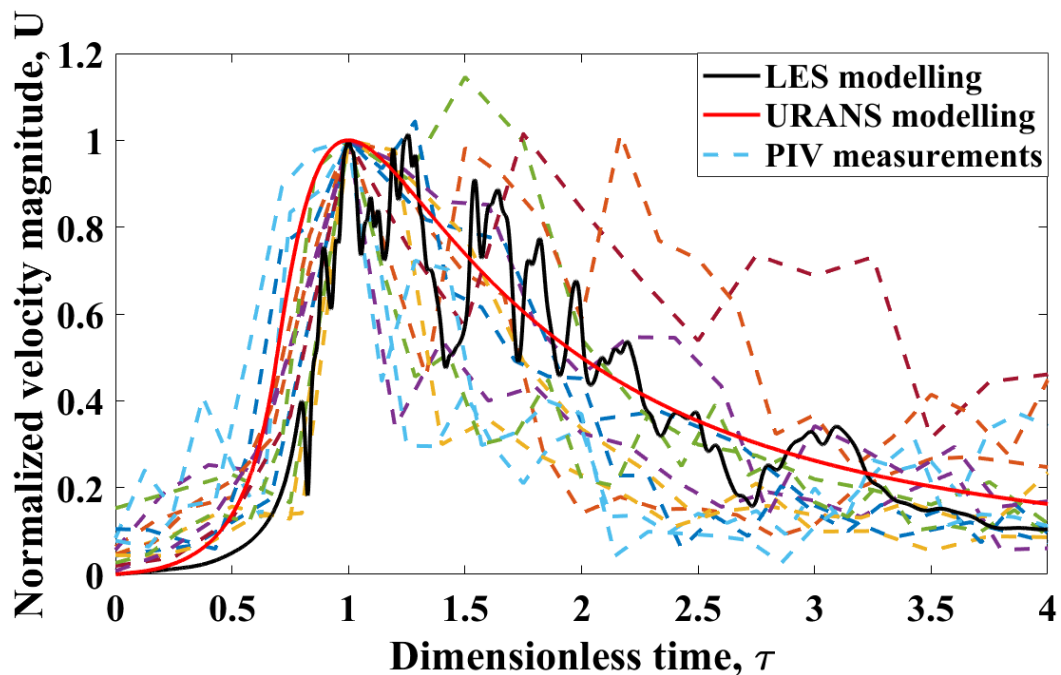


Figure 2.14: Comparison of the normalized velocity magnitude at the midpoint of each cough flow between the numerical and PIV results.

2.3.1.3 Comparison with the experimental data from the HWA measurements

Unlike the PIV technique, the hot-wire anemometry (HWA) needs to locate a measurement probe inside of the experimental domain and, hence, can be classified as an intrusive technique. This type of technique has been applied extensively in fluid mechanics research to measure various physical quantities, including velocity, turbulence and temperature, in a wide range of magnitude, fluctuation and direction (Tropea & Yarin, 2007). It can be conducted at a high frequency, normally several hundreds of Hz, to form a very small time step size. The HWA measurements, which include 11 sets of cough data and were obtained in the winter of 2017 (Mohamed, 2017), are used to validate the numerical results from both the LES and URANS approaches. These 11 sets of cough data have evident peak velocities $u_{pk} \geq 0.2$ m/s and, therefore, are considered to have good qualities for the validation of the numerical results. The axial velocity u is measured by the hot-wire probe, which is located at 1 m downstream and 0.22 m lower than the centreline of the FLUGIE chamber, within 10% uncertainty. The sampling frequency is 1000 Hz, which gives a time step of 0.001 *secs*.

To obtain a more generalized comparison for a better result analysis, the time history of velocity u is analyzed in a moving average way, and a normalization algorithm is employed to make sure the peak value is unity 1 for all the cough data and the numerical results. The details about the moving average methodology are shown in Appendix G. The following equations are used for the normalization purpose.

$$U = \frac{\langle u \rangle - u_s}{u_{pk} - u_s} \quad (2.23)$$

$$\tau = \frac{t - t_s}{t_{pk} - t_s} \quad (2.24)$$

where $\langle u \rangle$ and t represent the local moving average velocity and the corresponding time, u_s and t_s are the moving average velocity at the start of cough acceleration and the corresponding time, whilst u_{pk} and t_{pk} are the peak moving average velocity and the corresponding time.

Figure 2.15 (a) shows the comparison of the normalized variation of the velocity u component with time at the location of the hot-wire probe, i.e. (1, 0, -0.22) in metres, between the 11 sets of cough data and numerical results, where $\tau = 0$ represents the normalized time when the velocity u starts to increase with an obvious acceleration. It is found from Figure 2.15 (a) that the LES approach gives a good agreement with the HWA measurements for the trend of the velocity u variation, however, the URANS approach shows a smooth profile without any fluctuation due to the ensemble-averaged flow field of motion it solves for. To make a more simplified comparison, the data from 11 coughs are represented by a general trend curve, which is generated by the rational fitting model with the polynomial degree being 5 (The MathWorks, 2017), as shown in Figure 2.15 (b). It can be seen that the LES approach shows a variation trend, which is close and fluctuating around the fitting curve, therefore, giving a very good velocity u prediction and validates the effectiveness of the LES approach in predicting the velocity field of the flow field of coughing.

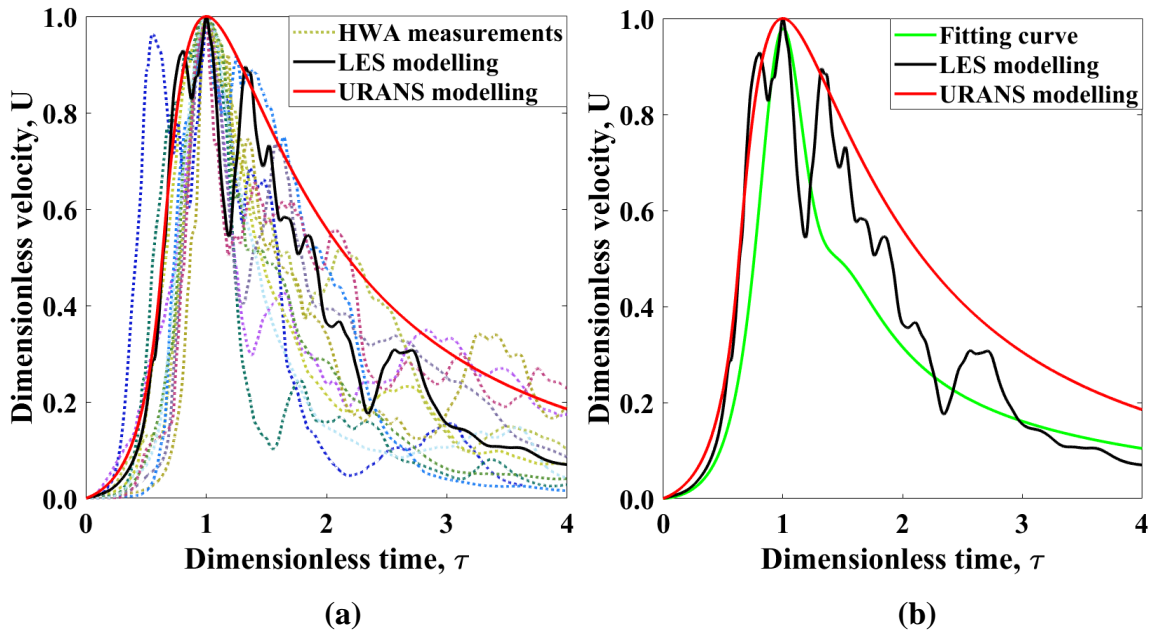


Figure 2.15: Comparison of the normalized velocity u component with (a) the raw data from 11 coughs and (b) the fitting model.

The peak velocity U_p of the flow field of coughing measured at the hot-wire probe location is plotted in Figure 2.16, where 51 sets of cough data in total obtained from different

participants in the winter of 2017 are included (Mohamed 2017). The peak velocity U_p and corresponding time T_p are calculated by

$$U_p = u_{pk} - u_s \quad (2.25)$$

$$T_p = t_{pk} - t_s \quad (2.26)$$

A fitting curve U_{p1} , which is generated by the following equation, is used to statistically fit all the 51 sets of cough data. It can be seen from the figure that the peak velocity U_p varies in the range of 0-1.3 m/s among all the HWA measurements, and the peak time T_p even extends to appropriately 11 secs for the very weak coughs ($U_p \ll 0.2$ m/s). The points obtained from both the URANS and LES modelling are located around the fitting curve, which give a reasonably good prediction of the peak velocity. The U_p and T_p are 0.83 m/s and 0.76 secs for the URANS modelling, and are 0.98 m/s and 0.86 secs for the LES modelling, respectively.

$$U_{p1} = a/T_p^b, \quad a = 0.31, \quad b = 1.00, \quad R^2 = 0.541 \quad (2.27)$$

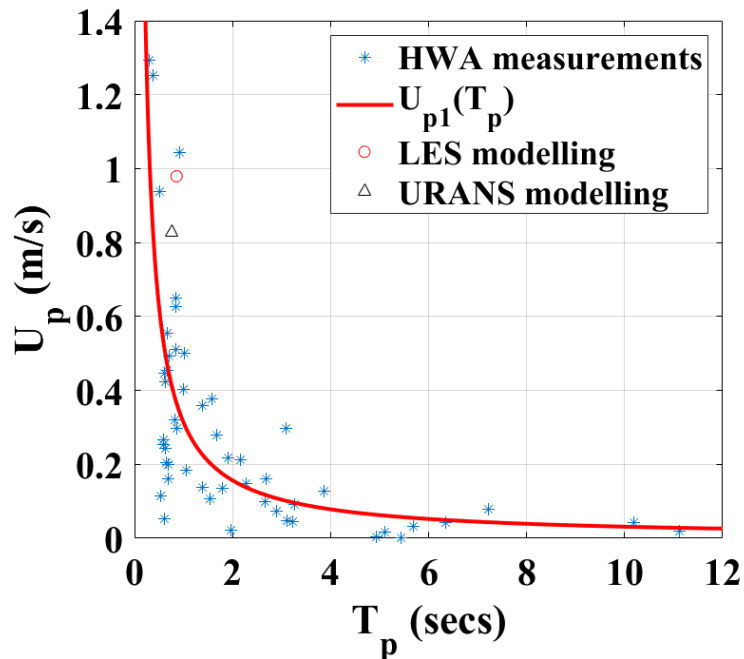


Figure 2.16: The general trend of the peak velocity for all the 51 coughs.

2.3.2 Streamwise penetration and maximum jet width

The streamwise penetration describes the variation of the longest flow distance along the streamwise direction with time and is very important in studying the dynamic characteristics of the flow field of coughing. The streamwise penetration obtained from the LES modelling is compared with the experimental work of Wei & Li (2017) who employed a cuboid water tank system to simulate the dynamic development of the flow field of coughing. A nozzle with a diameter of 0.01 m was used as the inlet to discharge dyed water horizontally into the tank. They used a combination of gamma-distribution-probability functions given by Gupta et al (2009) to represent the discharged time-dependent cough velocity profile, which was controlled by a servo motor system. Another two temporal profiles, including a sinusoidal and pulsation profiles, were also employed to investigate the effect of different inlet velocity profiles on the dynamic characteristics of the flow. In their study, the flow field of coughing was divided into two stages, which include the starting-jet and interrupted-jet stages. The starting-jet represents the stage when the cough starts and the fluid is being issued with an inlet transient velocity profile. After the fluid supply is terminated, the flow field of coughing enters the interrupted-jet stage and spreads in the ambient environment with the turbulence scale increasing. Figure 2.17 gives the visualizations of the starting-jet and interrupted-jet stages of the flow field of coughing obtained from the LES modelling. The transition from the starting-jet stage to the interrupted-jet stage takes place at the time of 0.61 *secs*, which is the end of the cough duration, as shown in Figure 2.17 (b).

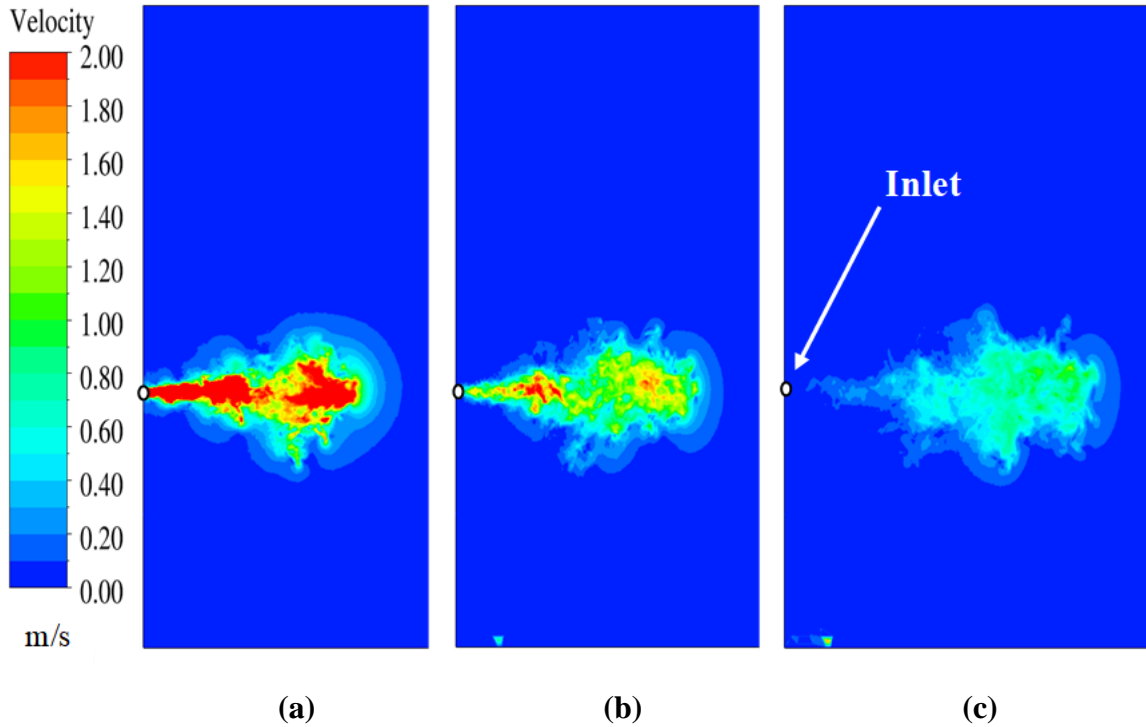


Figure 2.17: Visualizations of the starting-jet and interrupted-jet stages of the flow field of coughing obtained at (a) 0.30 secs, (b) 0.61 secs, and (c) 1.20 secs.

In the experimental work, three different inlet conditions were used for the cough velocity profile in order to examine the influence of those conditions on the streamwise penetration, as shown in Table 2.2, where u_m is the temporal mean inlet velocity, calculated by Eqn. (2.20), Q represents the cough expired volume, and A and d are the area and diameter of the inlet, respectively. The inlet diameters d for the experimental work and LES modelling are 0.01 m (i.e. diameter of the nozzle) and 0.0217 m (i.e. the average human mouth diameter) (Gupta et al., 2009), respectively.

Table 2.2: Inlet conditions used in the experiment and LES modelling.

Case number	$Re_m = \frac{u_m d}{\nu}$	$\frac{Q}{A \times d}$
Exp. 1	5200	100
Exp. 2	5200	150
Exp. 3	7900	150
LES	13084	248

The streamwise penetration x_p from the LES modelling is obtained based on the velocity magnitude contours, as shown in Figure 2.18, where the red cross symbol denotes the point at which the velocity is within 10% of the local peak velocity magnitude. The distance from the inlet to the marked location can be regarded as the longest flow distance along the streamwise direction, also known as the streamwise penetration. The comparison of the variation of streamwise penetration with time in the starting-jet stage between the LES modelling result and three sets of experimental data is provided in Figure 2.19 (a), where the streamwise penetration and flow time are presented in a dimensionless way in order to keep all these four sets of data in the same comparing status. It can be seen clearly that the LES modelling profile gives a fairly good agreement with the three experimental profiles, which manifests that the LES approach provides a satisfactory prediction of the near-field flow field of coughing.

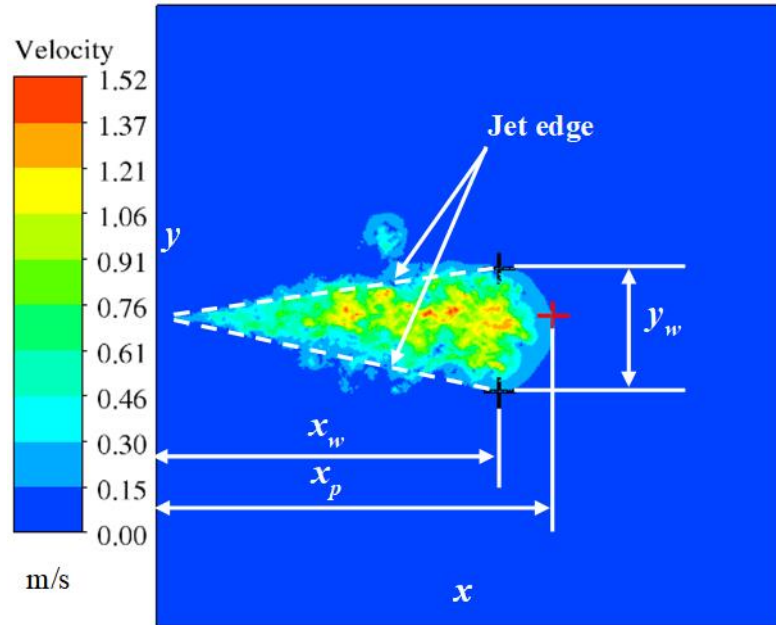


Figure 2.18: Illustration of the jet edge, the streamwise penetration distance x_p , the lateral maximum jet width y_w and the corresponding axial distance x_w on the x - y plane ($z=0$).

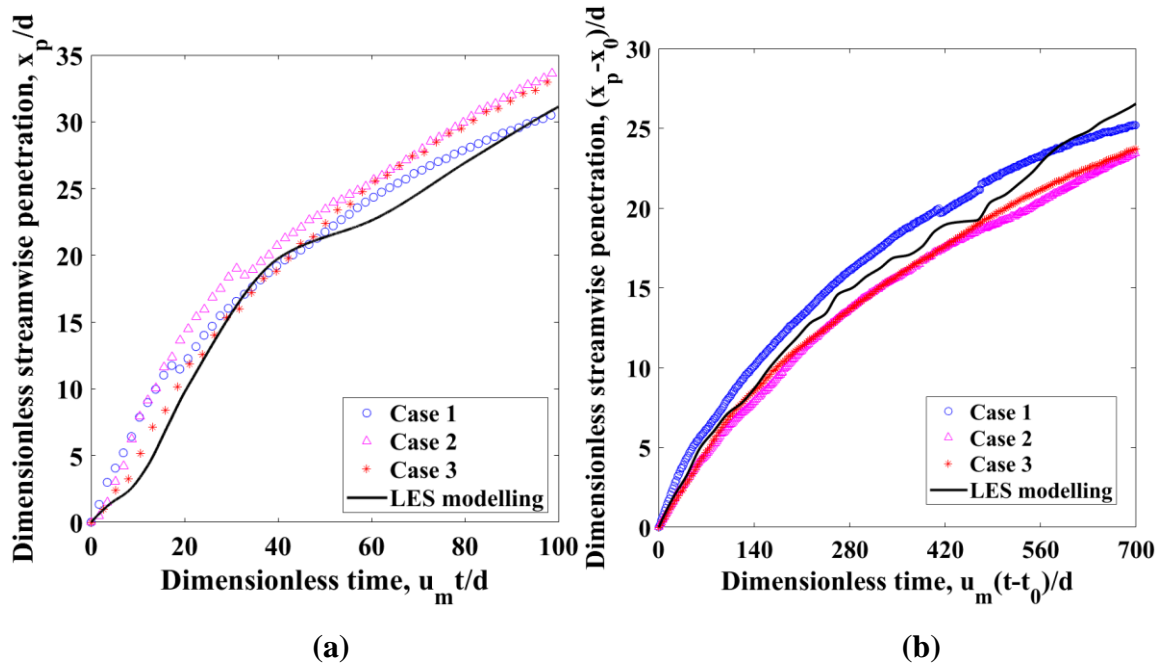


Figure 2.19: Comparison of the streamwise penetration as a function of time (a) at the starting-jet stage and (b) at the interrupted-jet stage.

Figure 2.19 (b) illustrates the comparison of the variation of streamwise penetration with time in the interrupted-jet stage, where two constants x_0 and t_0 are introduced to keep the comparison starting from (0, 0). The x_0 represents the penetration origin in the interrupted-jet stage, and x_0/d is constant for a given case, being in the range of 30.9-46.7 for the three experimental cases and 49.8 for the LES modelling. Similarly, the t_0 is the temporal origin, whilst the value of u_{mt_0}/d changes in 101.9-221.4 for the three experimental cases and equals 263.8 for the LES modelling. It is found that the LES modelling profile also gives a good agreement with the experimental data, even though the inlet conditions for these four cases are different, which infers that the far-field development will not be significantly affected by the inlet conditions, and validates the effectiveness of the LES approach in predicting the streamwise penetration of the flow field of coughing.

The maximum jet width is defined as the approximate maximum distance between the two jet edges on the velocity magnitude contour. In the present study, the jet edge is considered as the region where the velocity is within 10% of the local peak velocity magnitude, as illustrated in Figure 2.18. The vertical width z_w is obtained by using the same mechanism on the velocity magnitude contour on the x - z plane ($y=0$). In the interrupted-jet stage (i.e. no momentum supply), the maximum jet width maintains its growth as time progresses, due to the entrainment of the ambient air. The variation of the maximum jet width versus time (t) in both the vertical (z_w) and lateral (y_w) directions, as well as the corresponding axial (streamwise) distance x_w obtained from the LES modelling are presented in a normalized form in Figure 2.20. The z_{wn} and y_{wn} are the dimensionless maximum jet width in vertical and lateral directions, respectively, with the expressions of

$$z_{wn} = \frac{z_w - z_0}{d} \quad (2.28)$$

$$y_{wn} = \frac{y_w - y_0}{d} \quad (2.29)$$

where z_0 and y_0 are the vertical and lateral width origins in the interrupted-jet stage, whilst the constant values of z_0/d and y_0/d are 11.3 and 15.0, respectively. The dimensionless time τ is calculated by

$$\tau = \frac{u_{ip}(t-t_0)}{d} \quad (2.30)$$

where u_{ip} and d represent the inlet peak velocity (i.e. 22.06 m/s) and the inlet diameter (i.e. 0.0217 m), respectively. The t_0 is the temporal origin, and the constant value of t_0/d is 660.8. It is found that the lateral width is approximately 22% higher than the vertical width, which is due to the non-homogeneity of the velocity field. Both z_{wn} and y_{wn} grow with time in a roughly linear trend as seen from Figure 2.20 (a), and the equations to those trendlines are expressed as

$$z_1 = a_1\tau + b_1, a_1 = 0.0047, b_1 = 0.0728, R^2 = 0.971 \quad (2.31)$$

$$y_1 = a_2\tau + b_2, a_2 = 0.0056, b_2 = 0.0928, R^2 = 0.983 \quad (2.32)$$

Figure 2.20 (b) exhibits the variation of the axial distance (x_w) corresponding to the maximum jet width with time. x_w is normalized by the inlet diameter, as shown in the following equation.

$$x_{wn} = \frac{x_w - x_0}{d} \quad (2.33)$$

where x_0 is the axial distance origin in the interrupted-jet stage, and the constant value of x_0/d is 39.5. It can be seen that x_{wn} increases with time in a roughly second-order polynomial manner, with the equation representing the trendline as

$$x_1 = a_3\tau^2 + b_3\tau + c_3, a_3 = -2 \times 10^{-6}, b_3 = 0.0173, c_3 = 2.0089, R^2 = 0.992 \quad (2.34)$$

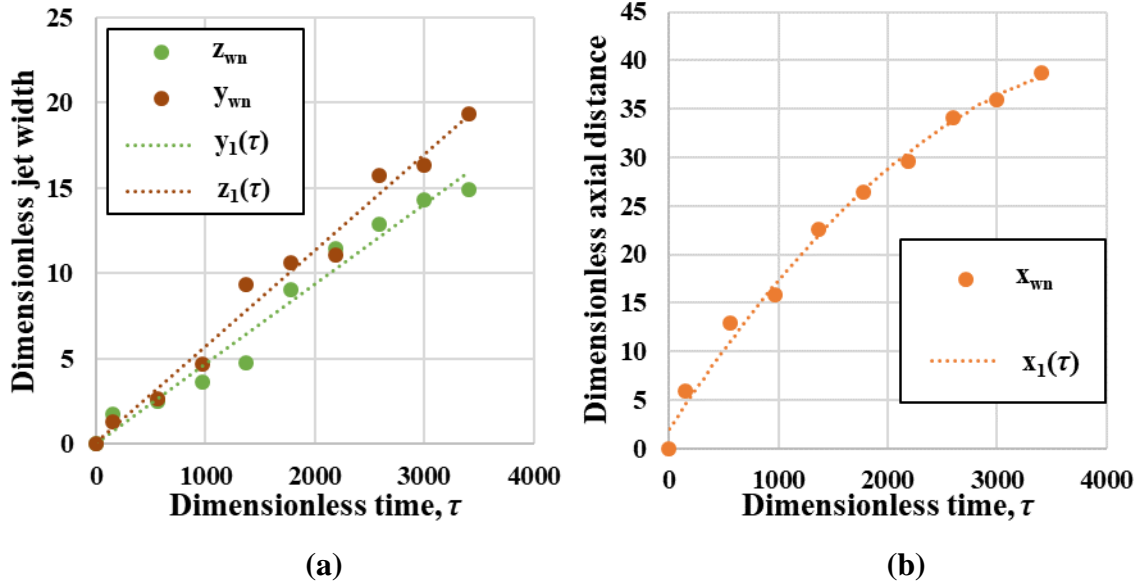


Figure 2.20: (a) Maximum jet width and (b) corresponding axial distance as a function of time in the interrupted-jet stage.

2.3.3 Power spectral density

The power spectral density is a measure of the energy spectrum which describes the distribution of the turbulent kinetic energy among eddies in different sizes (Pope, 2000). Three regions are distinguished by the energy spectrum through the size of eddy (Davidson, 2017). In the first region, eddies are in the large size and contain most of the energy which is extracted from the mean flow. The second region, also known as the inertial subrange, is where the turbulent kinetic energy being transferred per unit time from the large-scale to small-scale eddies. The process of the energy transfer, also called the cascade process, requires the Reynolds number to be high enough to ensure that the flow is fully turbulent in nature, and can be characterized by the Kolmogorov spectrum law (i.e. the $-5/3$ law), as expressed in the following equation,

$$E(\kappa) = C_K \varepsilon^{2/3} \kappa^{-5/3} \quad (2.35)$$

where the size of the eddy, i.e. the length scale, is expressed as $\frac{1}{\kappa}$, and ε and $E(\kappa)$ represent the unit time and transferred energy as a function of κ , respectively. The Kolmogorov

constant C_K has a value around 1.5. In the third region, eddies are isotropic and in the small size, and the dissipation occurs.

Figure 2.21 shows the comparison of the normalized spectral density at the location of the hot-wire probe, i.e. (1, 0, -0.22) in metres, between the LES modelling and the data from 11 coughs measured in the winter of 2017 by the HWA technique (Mohamed, 2017). Each spectrum (ϕ) is normalized by its respective variance value, and the frequency (f) is also scaled by the following equation in order to take into account the different mean velocities of all the cough flows.

$$\phi_n = \frac{\phi}{u'^2} \quad (2.36)$$

$$f_n = f \frac{d}{u_{pk}} \quad (2.37)$$

where u' represents the RMS of the fluctuating velocity component, d is the inlet diameter (i.e. 0.0217 m) and u_{pk} is the peak of the moving average velocity u component at the location of the hot-wire probe.

It is found from Figure 2.21 that all the energy spectra exhibit a decay form with the slope of $-5/3$, which indicates that the rate of energy transfer from the large-scale to small-scale eddies for all the 11 cough flows follows the hypothesis of Kolmogorov decay law, and the LES modelling gives a good prediction of the energy transfer process in the inertial subrange. However, it is pointed out here that these spectral plots are of the residual turbulence of the cough flows and do not represent the whole time history of the cough velocity.

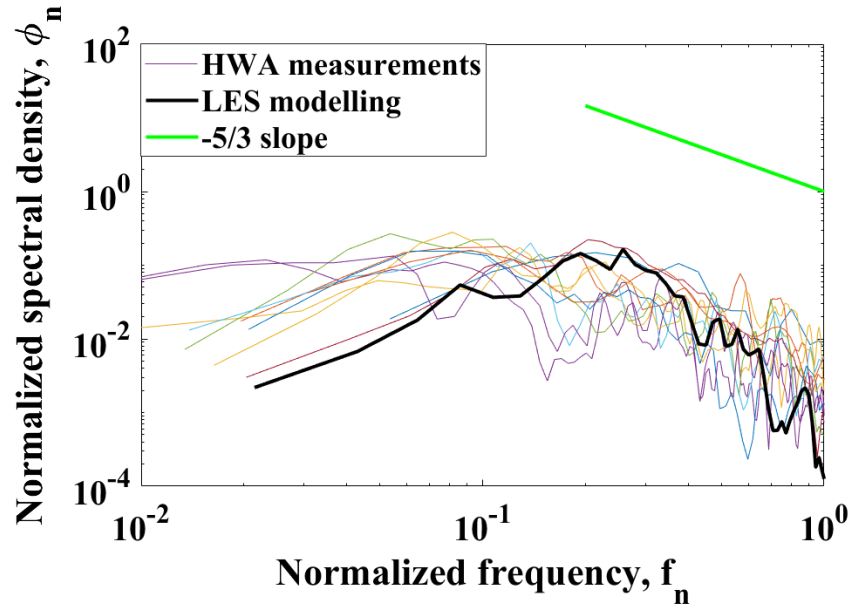


Figure 2.21: Comparison of the normalized spectral density.

Furthermore, it is noted that any signal of power spectral density below the value of $10^{-8} \text{ m}^2/\text{s}^2/\text{Hz}$ can be regarded as an electrical noise and is needed to be filtered for a more accurate analysis (Mohamed, 2017). A low-pass filter, which allows the signal frequencies lower than a certain frequency, also known as the cutoff frequency, to pass without attenuation, while attenuates the signal frequencies higher than the cutoff frequency, is used to filter the pure noise for the 11 sets of cough data. Figure 2.22 shows the comparison of power spectral density with the application of the low-pass filter. For the LES modelling, the cutoff frequency is defined as the frequency below which the turbulent kinetic energy is resolved, and is also distinguished as the frequency at which the power spectral density has an apparent decrease. It can be seen from Figure 2.22 that the power spectral density obtained from the LES modelling has a good agreement to that from the HWA measurements with a cutoff frequency of approximately 50 Hz, beyond which the turbulent kinetic energy is entirely modelled.

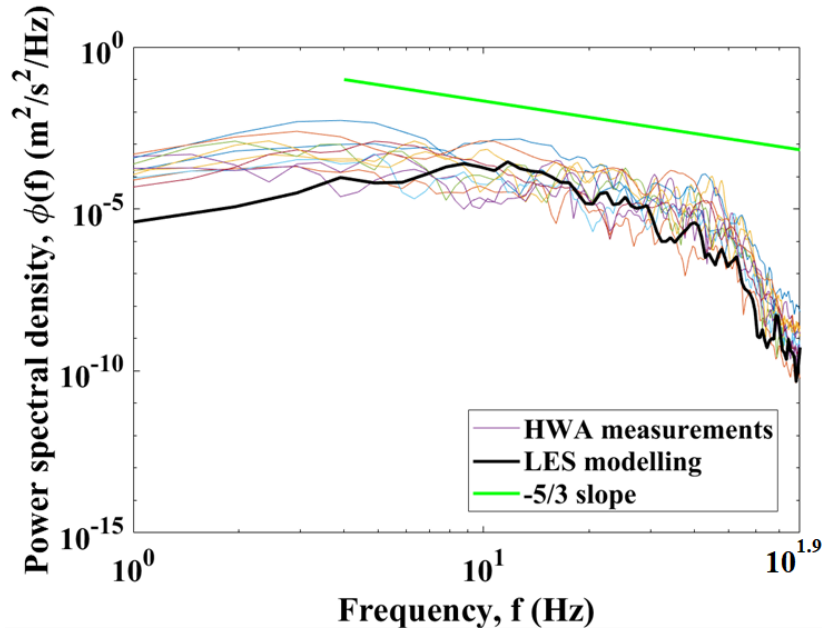


Figure 2.22: Comparison of the power spectral density with the low-pass filter in use.

2.4 Conclusions

The present study provides CFD modelling to numerically investigate the dynamic characteristics of the flow field of coughing, including the velocity field, streamwise penetration and power spectral density. Two modelling approaches, URANS and LES, are compared. The numerical results are validated by the experimental data from the PIV and HWA measurements, as well as the published data.

In the analysis of the velocity field, the contours of velocity magnitudes at different time obtained from the two numerical modelling approaches are compared. It is found that the URANS modelling gives a velocity distribution in a symmetric and regular way, which indicates that the flow field spreads uniformly. However, the LES modelling shows an irregular and non-uniform velocity distribution, which is similar to that from the PIV measurement, and hence, gives a more realistic and accurate prediction of the variation of the velocity magnitude with time of the flow field of coughing. The numerical results are also compared with the PIV measurements in terms of the spatially averaged velocity on the rectangular field of view and 2-dimensional velocity magnitude at the midpoint of each

cough flow. It is found that the LES modelling and the PIV measurements have a similar variation of the velocity with time and the peak values are close, while the URANS modelling exhibits a smooth variation trend without any fluctuation due to the ensemble-averaged flow field of motion it solves for. In the comparison with the HWA measurements, the variation of the velocity u component with time at the location of the hot-wire probe is analyzed in a normalized way in order to obtain a more generalized comparison. The LES modelling gives a very good agreement for the velocity u variation with the eleven sets of cough data obtained by the HWA technique, while the URANS modelling still shows a smooth trend. In summary, based on the investigation of the velocity field, the URANS approach may not be appropriate, compared with the LES approach, to predict the dynamic development of the flow field of coughing. Furthermore, the LES modelling is compared with the work of Wei & Li (2017) regarding the streamwise penetration. Relevant numerical results from the LES modelling are compared with three sets of experimental data under different inlet conditions. The agreement is very good for the normalized profile of streamwise penetration distance in both the starting-jet and interrupted-jet stages, which validates the effectiveness of the LES approach in predicting the streamwise penetration of the flow field of coughing. In the interrupted-jet stage, the maximum jet width is found to grow with time in a roughly linear trend, and the corresponding axial distance increases with time in a roughly second-order polynomial manner. The power spectral density obtained from the LES modelling and HWA measurements is also compared to investigate the energy transfer from the large-scale to small-scale eddies at the location of hot-wire probe. It is found that all the energy spectra have a universal decay with the slope of $-5/3$, which indicates that the energy transfer process in the inertial subrange follows the Kolmogorov hypothesis. Moreover, in the comparison of the power spectral density with a low-pass filter being introduced, the LES modelling gives a good agreement with the eleven sets of experimental cough data with a cutoff frequency of around 50 Hz. In conclusion, based on the comparison with the URANS approach and the experimental data, the LES approach can predict the dynamic development of the flow field of coughing reasonably well.

For future work, different conditions, including the transient cough velocity profile at the inlet, the ambient RH, etc., should be investigated for the influences on the dynamic

characteristics of the flow field of coughing. Furthermore, more voluntary participants are needed for the cough data collection and, therefore, more experimental data can be used to validate the numerical results.

The next chapter will discuss the droplets produced by coughing in terms of the droplet dispersion and evaporation. The LES approach and the Lagrangian discrete phase model will be used for the CFD modelling to predict the flow field and the droplets, respectively. Different inlet and ambient conditions, including the time-dependent cough velocity at the inlet and the ambient RH, will be analyzed in terms of the effects of those conditions on the dispersion and evaporation processes of the droplets.

References

- Abdel-Rahman, A. A. (2010). A review of effects of initial and boundary conditions on turbulent jets. *WSEAS transactions on Fluid Mechanics*, 5(4), 257–275.
- ANSYS, Inc. (2013). *ANSYS Fluent Theory Guide 15.0*.
- ANSYS, Inc. (2014). *ANSYS Fluent User's Guide 15.0*.
- Antonia, R. A., & Zhao, Q. (2001). Effect of initial conditions on a circular jet. *Experiments in Fluids*, 31(3), 319–323.
- Balaras, C. A., Dascalaki, E., & Gaglia, A. (2007). HVAC and indoor thermal conditions in hospital operating rooms. *Energy and Buildings*, 39(4), 454–470.
- Bisoi, M., Das, M. K., Roy, S., & Patel, D. K. (2017). Large eddy simulation of three-dimensional plane turbulent free jet flow. *European Journal of Mechanics, B/Fluids*, 65, 423–439.
- Boersma, B. J., Brethouwer, G., & Nieuwstadt, F. T. M. (1998). A numerical investigation on the effect of the inflow conditions on the self-similar region of a round jet. *Physics of Fluids*, 10(4), 899–909.
- Bogey, C., & Bailly, C. (2006). Large eddy simulations of round free jets using explicit filtering with/without dynamic Smagorinsky model. *International Journal of Heat and Fluid Flow*, 27(4), 603–610.
- Bourouiba, L., Dehandschoewercker, E., & Bush, J. W. M. (2014). Violent expiratory events: on coughing and sneezing. *Journal of Fluid Mechanics*, 745, 537–563.
- Bucher, K. (1958). Pathophysiology and pharmacology of cough. *Pharmacological Reviews*, 10(1), 43–58.

- Cetin, M. O., Meinke, M., & Schröder, W. (2017). Numerical analysis of the impact of exit conditions on low Mach number turbulent jets. *International Journal of Heat and Fluid Flow*, *67*, 1339–1351.
- Chang, K., & Lin, R. (1989). A comparison of turbulence models for uses in calculations of free jets and flames. In *27th Aerospace Sciences Meeting*.
- Chorin, A. J. (1968). Numerical solution of Navier-Stokes equations. *Mathematics of Computation*, *22*(104), 745–762.
- Darisse, A., Lemay, J., & Benaïssa, A. (2013). LDV measurements of well converged third order moments in the far field of a free turbulent round jet. *Experimental Thermal and Fluid Science*, *44*, 825–833.
- Davidson, L. (2017). *Fluid Mechanics, Turbulent Flow and Turbulence Modeling*. Göteborg, Sweden: Chalmers University of Technology.
- Di Venuta, I., Petracci, I., Angelino, M., Boghi, A., & Gori, F. (2018). Numerical simulation of mass transfer and fluid flow evolution of a rectangular free jet of air. *International Journal of Heat and Mass Transfer*, *117*, 235–251.
- Dowling, D. R., & Dimotakis, P. E. (1990). Similarity of the concentration field of gas-phase turbulent jets. *Journal of Fluid Mechanics*, *218*(1), 109.
- Dudalski, N., Mohamed, A. F. A., Savory, E., & Mubareka, S. (2018). Experimental measurements of far field cough airflows produced by healthy and influenza-infected subjects. In *Proceedings of the Canadian Society for Mechanical Engineering International Congress 2018*, Toronto, Canada.
- Ferdman, E., Ötügen, M. V., & Kim, S. (2000). Effect of initial velocity profile on the development of round jets. *Journal of Propulsion and Power*, *16*(4), 676–686.
- Fielder, H. E. (1998). Control of free turbulent shear flows. In M. G. El-Hak, A. Pollard, & J. P. Bonnet (Eds.), *Flow Control: Fundamentals and Practices* (pp. 335–429). Germany: Springer-Verlag.

- Flora, J. J., & Goldschmidt, V. W. (1969). Virtual origins of a free plane turbulent jet. *AIAA Journal*, 7(12), 2344-2346.
- George, W. K. (1989). The self-preservation of turbulent flows and its relation to initial conditions and coherent structures. *Advances in Turbulence*.
- Germano, M., Piomelli, U., Moin, P., & Cabot, W. H. (1991). A dynamic subgrid-scale eddy viscosity model. *Physics of Fluids A: Fluid Dynamics*, 3(7), 1760–1765.
- Germano, M., Piomelli, U., Moin, P., & Cabot, W. H. (1996). A dynamic subgrid-scale eddy viscosity model. *Physics of Fluids A: Fluid Dynamics*, 3(7), 1760–1765.
- Ghahremanian, S., & Moshfegh, B. (2013). Evaluation of RANS models in predicting low Reynolds, free, turbulent round jet. *Journal of Fluids Engineering*, 136(1), 11201.
- Gohil, T. B., Saha, A. K., & Muralidhar, K. (2014). Large eddy simulation of a free circular jet. *Journal of Fluids Engineering*, 136(5), 51205.
- Gori, F., Petracci, I., & Angelino, M. (2013). Flow evolution of a turbulent submerged two-dimensional rectangular free jet of air. Average Particle Image Velocimetry (PIV) visualizations and measurements. *International Journal of Heat and Fluid Flow*, 44, 764–775.
- Gori, F., Petracci, I., & Angelino, M. (2014). Influence of the Reynolds number on the instant flow evolution of a turbulent rectangular free jet of air. *International Journal of Heat and Fluid Flow*, 50, 386–401.
- Gupta, J. K., Lin, C.-H., & Chen, Q. (2009). Flow dynamics and characterization of a cough. *Indoor Air*, 19(6), 517–525.
- Hinze, J. O. (1975). *Turbulence*. McGraw-Hill.
- Kannan, B. T. (2015). Computation of an axisymmetric jet using OpenFOAM. *Procedia Engineering*, 127, 1292–1299.

- Kannan, B. T., Karthikeyan, S., & Sundararaj, S. (2009). Comparison of turbulence models in simulating axisymmetric jet flow. In *Innovative Design and Development Practices in Aerospace and Automotive Engineering* (pp. 401–407). Springer Singapore.
- Kim, J., & Choi, H. (2009). Large eddy simulation of a circular jet: effect of inflow conditions on the near field. *Journal of Fluid Mechanics*, 620, 383.
- Kim, W.-W., & Menon, S. (1997). Application of the localized dynamic subgrid-scale model to turbulent wall-bounded flows. In *35th Aerospace Sciences Meeting & Exhibit*. Reno, NV: American Institute of Aeronautics and Astronautics, Inc.
- Klein, M., Sadiki, A., & Janicka, J. (2003). Investigation of the influence of the Reynolds number on a plane jet using direct numerical simulation. *International Journal of Heat and Fluid Flow*, 24(6), 785–794.
- Kraichnan, R. (1970). Diffusion by a random velocity field. *Physics of Fluids*, 11, 21–31.
- Kwon, S. J., & Seo, I. W. (2005). Reynolds number effects on the behavior of a non-buoyant round jet. *Experiments in Fluids*, 38(6), 801–812.
- Lilly, D. K. (1992). A proposed modification of the Germano subgrid-scale closure method. *Physics of Fluids A: Fluid Dynamics*, 4(3), 633–635.
- Matsuda, T., & Sakakibara, J. (2005). On the vortical structure in a round jet. *Physics of Fluids*, 17(2), 1–11.
- Menter, F. R. (1994). Two-equation eddy-viscosity turbulence models for engineering applications. *AIAA Journal*, 32(8), 1598–1605.
- Mi, J., & Nathan, G. J. (2009). Statistical properties of turbulent free jets issuing from nine differently-shaped nozzles. *Flow, Turbulence and Combustion*, 84(4), 583–606.
- Mi, J., Nathan, G. J., & Luxton, R. E. (2001). Centreline mixing characteristics of jets from nine differently shaped nozzles. *Experiments in Fluids*, 28(1), 93–94.

- Mi, J., Nathan, G. J., & Nobes, D. S. (2001). Mixing characteristics of axisymmetric free jets from a contoured nozzle, an orifice plate and a pipe. *Journal of Fluids Engineering*, 123(4), 878.
- Mi, J., Nobes, D. S., & Nathan, G. J. (2001). Influence of jet exit conditions on the passive scalar field of an axisymmetric free jet. *J. Fluid Mech.*, 432(4), 878.
- Mohamed, A. F. A. (2017). *Experimental Measurements of Far Field Cough Airflows Produced by Healthy and Influenza-Infected Human Subjects*. M. E. Sc. Thesis, Department of Mechanical and Materials Engineering, The University of Western Ontario.
- Nicoud, F., & Ducros, F. (1999). Subgrid-scale stress modelling based on the square of the velocity gradient tensor. *Flow, Turbulence and Combustion*, 62, 183–200.
- Nijemeisland, M., & Dixon, A. G. (2004). CFD study of fluid flow and wall heat transfer in a fixed bed of spheres. *AIChE Journal*, 50(5), 906–921.
- Panchapakesan, N. R., & Lumley, J. L. (1993). Turbulence measurements in axisymmetric jets of air and helium. Part 1. Air jet. *Journal of Fluid Mechanics*, 246(1), 225.
- Patankar, S. V., Spalding, D. B., & Road, E. (1972). A calculation procedure for heat, mass and momentum transfer in three-dimensional parabolic flows. *International Journal of Heat and Mass Transfer*, 15(10), 1787–1806.
- Pérez, C. C., Barreto, C. V., Lopes, G., Carneiro, J. N. E., Abrantes, J. K., Jr, J. M. B., & Nieckele, A. O. (2005). Evaluation of different turbulence models to predict a turbulent free jet. In *18th International Congress of Mechanical Engineering*. Ouro Preto, MG.
- Piirilä, P., & Sovijärvi, A. R. A. (1995). Objective assessment of cough. *European Respiratory Journal*, 8, 1949-1956.
- Pitts, W. M. (1991). Reynolds number effects on the mixing behavior of axisymmetric turbulent jets. *Experiments in Fluids*, 11(2–3), 135–141.

- Pope, S. B. (2000). *Turbulent Flows*. New York: Cambridge University Press.
- Prandtl, L. (1925). Bericht über untersuchungen zur ausgebildeten turbulenz. *Z. Angew. Math. Mech*, 5(2), 136–139.
- Quinn, W. R. (2006). Upstream nozzle shaping effects on near field flow in round turbulent free jets. *European Journal of Mechanics, B/Fluids*, 25(3), 279–301.
- Ranga Dinesh, K. K. J., Savill, A. M., Jenkins, K. W., & Kirkpatrick, M. P. (2010). LES of intermittency in a turbulent round jet with different inlet conditions. *Computers and Fluids*, 39(9), 1685–1695.
- Richards, C. D., & Pitts, W. M. (1993). Global density effects on the self-preservation behaviour of turbulent free jets. *Journal of Fluid Mechanics*, 254(1), 417.
- Rodi, W. (1972). *The Prediction of Free Turbulent Boundary Layers by Use of a Two-Equation Model of Turbulence*. Diss. Imperial College London (University of London).
- Saladin, K. S. (2003). *Anatomy & Physiology* (3rd ed.). New York: McGraw Hill.
- Salim, S. M., Ong, K. C., & Cheah, S. C. (2011). Comparison of RANS, URANS and LES in the prediction of airflow and pollutant dispersion. In *World Congress on Engineering and Computer Science 2011*, 2, San Francisco, USA.
- Shih, T.-H., Liou, W. W., Shabbir, A., Yang, Z., & Zhu, J. (1995). A new k- ϵ eddy viscosity model for high Reynolds number turbulent flows-model development and validation. *Computers & Fluids*, 24(3), 227–238.
- Shinneeb, A.-M., Bugg, J. D., & Balachandar, R. (2008). Quantitative investigation of vortical structures in the near-exit region of an axisymmetric turbulent jet. *Journal of Turbulence*, 9(19), 1–20.
- Smagorinsky, J. (1963). General circulation experiments with the primitive equations I. The basic experiment. *Monthly Weather Review*, 91(3), 99–164.

- Smirnov, R., Shi, S., & Celik, I. (2001). Random flow generation technique for large eddy simulations and particle-dynamics modeling. *Journal of Fluids Engineering*, *123*, 359–371.
- Smith, E. J., Mi, J., Nathan, G. J., & Dally, B. B. (2004). Preliminary examination of a “round jet initial condition anomaly” for the k- ϵ turbulence model. In *15th Australasian Fluid Mechanics Conference*. The University of Sydney, Sydney, Australia.
- Stambuis, E. J. (2006) Basics and principles of particle image velocimetry (PIV) for mapping biogenic and biologically relevant flows. *Aquatic Ecology*, *40*(4), 463-479.
- Stanley, S. A., Sarkar, S., & Mellado, J. P. (2002). A study of the flow-field evolution and mixing in a planar turbulent jet using direct numerical simulation. *Journal of Fluid Mechanics*, *450*, 377–407.
- The MathWorks, Inc. (2017). Rational polynomials. Retrieved from <https://cn.mathworks.com/help/curvefit/rational.html>
- Tropea, C., & Yarin, A. L. (2007). Springer handbook of experimental fluid mechanics. *Springer Science & Business Media*, *1*.
- Van Leer, B. (1979). Toward the ultimate conservative difference scheme. IV. A second order sequel to Godunov’s method. *Journal of Computational Physics*, *32*, 101–136.
- Wei, J., & Li, Y. (2017). Human cough as a two-stage jet and its role in particle transport. *PLoS ONE*, *12*(1), 1–15.
- Xie, X., Li, Y., Chwang, A. T. Y., Ho, P. L., & Seto, W. H. (2007). How far droplets can move in indoor environments - revisiting the Wells evaporation-falling curve. *Indoor Air*, *17*(3), 211–225.
- Xu, G., & Antonia, R. A. (2002). Effect of different initial conditions on a turbulent round free jet. *Experiments in Fluids*, *33*(5), 677–683.

Zhu, S., Kato, S., & Yang, J.-H. (2006). Study on transport characteristics of saliva droplets produced by coughing in a calm indoor environment. *Building and Environment*, *41*(12), 1691–1702.

Chapter 3

3 CFD Modelling of the Droplets Produced by Coughing

3.1 Introduction

Violent expiratory activity, which includes coughing, sneezing and speaking, has been regarded as one of the major sources of respiratory disease transmission (Bourouiba et al., 2014). Such forced exhalation can release thousands of droplets in various sizes, which carry different infectious agents, including viruses, pathogens, fungi and bacteria, various physiological electrolytes as well as a variety of cells (Atkinson et al., 2009). During the airborne transmission, the pure water portion of the droplets will evaporate and the droplet nuclei, which consist of various microorganisms and were first reported by Wells (1934), will remain, as shown in Figure 3.1. It is found that as the liquid evaporates, the non-evaporative content of a droplet concentrates gradually and forms a droplet nucleus. Other than the ambient relative humidity (RH) and temperature, which affect the evaporation rate (Wells, 1955), the droplet size also has a significant influence on the evaporation process. Wells (1934, 1955) observed the evaporation time for droplets in a wide range of diameters from 1 to 1000 μm , and found that the large droplets with diameter $d_p > 100 \mu\text{m}$ remained airborne for less than 1 *sec* without complete evaporation, while most of the droplets with $d_p < 100 \mu\text{m}$, especially the small droplets with $d_p < 10 \mu\text{m}$, evaporated very quickly and finally evolved into droplet nuclei, which were suspended in the ambient environment and might result in the airborne transmission of respiratory diseases. Figure 3.2 exhibits a falling and evaporation curve (Wells, 1934), which indicates the relationship between the droplet size, falling and evaporation rates. From the curve, it is clear that under the condition with the RH and temperature of the ambient air of 0 and 18 °C, respectively, the droplets with $d_p < 100 \mu\text{m}$ would evaporate completely before precipitating on the ground 2 m away from the source. Lange and Keschischian (1925) also investigated the impact of droplet size on evaporation experimentally by using an artificially atomized eosin solution. It was found that the droplets with $d_p > 200 \mu\text{m}$ fell to the ground in a few seconds, while the droplets with $d_p < 20 \mu\text{m}$ remained suspended in the ambient environment for a few hours with complete evaporation.

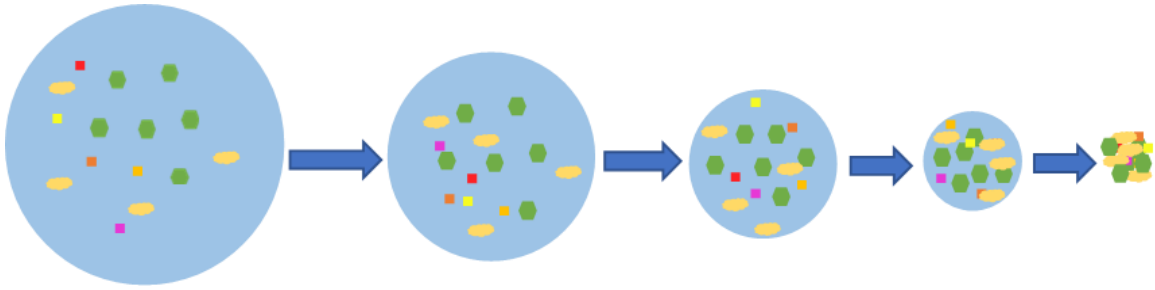


Figure 3.1: Evaporation process of a droplet released by human expiratory activity (adapted from Verreault et al. (2008)).

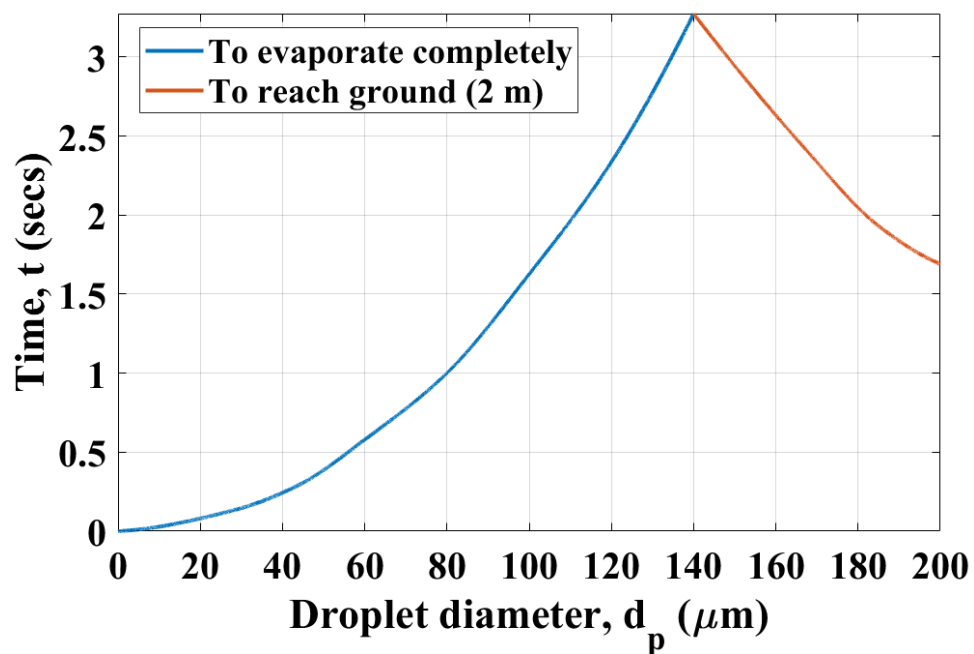


Figure 3.2: Falling and evaporation curve of droplets expelled by human expiratory activity (adapted from Wells (1934)).

3.1.1 Studies of droplet size distribution

A lot of previous studies have focused on the size distribution of respiratory droplets. Some researchers used a glass slide to capture the droplets in front of the human mouth and estimated the size by measuring the circular stain-marks caused by the droplets (Duguid, 1946). By employing this approach, Jennison (1942) found that the droplets released by coughing and speaking were in the diameter range 20-2000 μm with the majority being 100-500 μm . However, Strausz (1926) stated that the size measured by the stain-marks was

three times larger than the actual droplet size and, taking this into consideration, he reported a new diameter range 10-500 μm with most of the droplets being 70-85 μm . To obtain a more accurate measurement, Duguid (1946) conducted a comprehensive experiment by applying a direct micrometry through filtering the droplet nuclei onto the oiled slides to measure the droplets in smaller sizes, and measuring the stain-marks on the glass slides for larger droplets. He found the diameter range was 1-2000 μm with the majority of droplets being 4-8 μm for sneezing and 8-16 μm for coughing. Another technique, named an Optical Particle Counter (OPC), was used by Fairchild and Stampfer (1987), and a much smaller diameter range 0.09-3 μm was detected with a peak distribution smaller than 0.3 μm . Papineni and Rosenthal (1997) also utilized the OPC system, together with an Analytical Transmission Electron Microscope (AEM) to investigate the size of droplets from coughing, breathing and speaking. The OPC measurements demonstrated that most of the droplets had a diameter smaller than 1 μm with an average mode of 0.3 μm , and larger droplets with approximately 8 μm diameter were detected by the AEM technique. It was also found that compared with breathing and speaking, coughing could generally release droplets with larger sizes. However, since the OPC technique could only detect the droplets with very small diameters, it was limited in use. Recently, various techniques were used in experimental studies on the size distribution of respiratory droplets. Chao et al (2009) used an Interferometric Mie Imaging (IMI) method to measure the droplet size, and found that 947-2085 droplets with an average mode diameter of 13.5 μm were generated by coughing, while speaking produced 112-6720 droplets with an average mode diameter of 16.0 μm . All the released droplets were distributed in the diameter range of 2-2000 μm . By applying the Aerodynamic Particle Sizer (APS) and Scanning Mobility Particle Sizer (SMPS) systems, Yang et al (2007) found that the droplets generated by coughing fell in the diameter range of 0.62-15.9 μm with an average mode of 8.35 μm . They also obtained a size distribution of droplet nuclei, which was 0.58-5.42 μm , and most of them were in 0.74-2.12 μm . Lindsley et al (2012) studied the size distribution and quantity of the droplets expelled by coughing from both the influenza-infected and recuperated human subjects through the technique of a Laser Aerosol Particle Spectrometer (LAPS). It was indicated that the average number of droplets each cough was quite similar for the infected subjects (i.e. 900-302,200) and the subjects after recovery (i.e. 1100-308,600). The droplet diameter

was found to range between 0.35 and 10 μm , with the average modes of 0.57-0.71 μm for the infected subjects and 0.57-0.89 μm for the recuperated subjects. To summarize, the size distribution of respiratory droplets obtained from previous studies is listed in Table 3.1.

3.1.2 Studies of droplet dispersion and evaporation

In order to investigate the dynamic characteristics of the droplets produced by coughing, many studies have been carried out by using experimental, numerical and theoretical methods. Zhu et al (2006) employed three different experimental techniques to study the coughing process in a still indoor environment, which include a particle image velocimetry (PIV) system to measure the velocity of the flow field in a styrene-board chamber, a mask to quantify the amount of saliva produced by coughing, and a digital video camera to record the droplet dispersion. It was found that during the coughing process, more than 6.7 mg of the saliva droplets could be released and travel farther than 2 m. The velocity of the droplets was high over a distance of approximately 0.03 m from the inlet, and gradually decreased as the droplets dispersed and moved farther. They also conducted a Computational Fluid Dynamics (CFD) simulation by using the Lagrangian model, and found a significant effect of the droplet size on the dispersion process. The numerical results indicated that for the small droplets with $d_p \leq 30 \mu\text{m}$, the dispersion was more affected by the ambient flow field than by the gravity or inertia, while as the droplet size increased, the impact of the gravity and inertia became more and more significant. Xie et al (2007) theoretically studied the dynamic characteristics of the droplets expelled by coughing, sneezing and breathing through creating a physical model based on the Wells evaporation-falling curve (Wells, 1934). It was found that the droplet size had a dominant effect on the evaporation and dispersion processes of the droplets, i.e. large droplets ($d_p > 100 \mu\text{m}$) would fall to the ground rapidly without complete evaporation while small droplets ($d_p < 100 \mu\text{m}$) would evaporate completely and penetrate a long distance, which was more than 2 m for coughing, more than 6 m for sneezing and less than 1 m for breathing.

Wei and Li (2017) experimentally studied the transport characteristics of cough droplets by employing a Sediment Feeding System (SFS) (Li, 2006) to inject glass beads, which had similar sizes to cough droplets, into a cuboid water tank. A digital video camera was used to record the transport process of the glass beads. They also developed a protocol

based on the Stokes' law, in order to scale the results between the experiment in the water, and the prototype in the air. It was found that, unlike the previous studies, the droplets in different sizes showed a similar maximum penetration distance due to the effect of the leading vortex (Tang et al., 2009 & Bourouiba et al., 2014), which provided a positive velocity component in the vertical direction and carried the droplets farther downstream. Furthermore, the cough duration also had a significant effect on the droplet dispersion, i.e. the longer the cough lasted, the farther the droplets would travel. However, the protocol might introduce error when scaling the data between the glass beads in the water and the actual liquid droplets in the air for large droplets, which were defined as the droplets being 96-114 μm in diameter.

Moreover, the influence of the ambient RH was also investigated. As a result, more droplets and droplet nuclei would remain suspended in the ambient environment at a low RH, which was less than 40%. Aliabadi et al (2010) numerically investigated the impacts of the droplet size and the ambient RH on the droplet evaporation and dispersion by a CFD simulation of human cough flow. In their study, the Lagrangian discrete phase model was used to track a total of 5000 expired droplets in the diameter range 1-500 μm . The numerical results indicated that compared with large droplets, small droplets evaporated more rapidly and were less influenced by the gravity, therefore, having a longer penetration distance. Furthermore, a low RH accelerated the evaporation process, which was consistent with the conclusion given by Xie et al (2007).

Table 3.1: Summary of size distribution of respiratory droplets.

Study field	Experimental technique	Diameter range, μm	Average mode, μm	Literature
Coughing & speaking	Glass slide	20-2000	100-500	(Jennison, 1942)
Coughing & speaking	Glass slide	10-500	70-85	(Strausz, 1926)
Coughing, sneezing & speaking	Oiled slide & glass slide	1-2000	8-16 for coughing & 4-8 for sneezing	(Duguid, 1946)
Exhaled breathing	OPC	0.09-3	< 0.3	(Fairchild & Stampfer, 1987)
Coughing, breathing & speaking	OPC & AEM	≤ 8	0.3	(Papineni & Rosenthal, 1997)
Coughing & speaking	IMI	2-2000	13.5 for coughing & 16.0 for speaking	(Chao et al., 2009)
Coughing	APS & SMPS	0.62-15.9	8.35	(Yang et al., 2007)
Coughing	LAPS	0.35-10	0.57-0.71 for influenza-infected subjects & 0.57-0.89 for recuperated subjects	(Lindsley et al., 2012)

3.1.3 Studies of respiratory pathogen transmission

A respiratory pathogen is defined as a micro-organism, including a bacterium, virus, prion, protozoa, fungus, etc., that can cause infectious respiratory diseases. In order to prevent the spread of the respiratory disease infection, it is necessary to understand the pathways of respiratory pathogen transmission (Gratton et al., 2011). The size of the droplets, which

are produced by human expiratory activity, plays a key role in the transmission of the respiratory pathogen. Based on the size distribution of the expelled droplets, the respiratory pathogen transmission is classified into two ways, airborne and droplet transmission. Airborne transmission is defined as being caused by small droplets that can remain suspended in the ambient air for a prolonged period and which, therefore, can affect a great number of subjects and persist for a long distance from the infection source (Garner, 1996 & Duguid, 1946). Droplet transmission is due to the larger droplets (of diameter $d_p > 100 \mu\text{m}$), which have a propensity to precipitate quickly on the ground (Wells, 1934). Such kind of transmission can only exist for a short distance from the source, usually within 1 m, which is determined by the size of the larger droplets (Garner, 1996), and hence, can only cause infection to those subjects who are in close proximity to the source.

In the physiological field, the transmission of a respiratory pathogen results from the deposition of the pathogen-laden droplets of different sizes. After the droplets are released by the infection source and inhaled by a susceptible subject, the droplets with $d_p > 10 \mu\text{m}$ are more likely to deposit on the surface of the upper airway and are less likely to transmit to the deeper pulmonary region. Conversely, the droplets with $d_p \leq 10 \mu\text{m}$ are more likely to travel with the inhaled airflow and transmit deeper into the respiratory tract (Austin et al., 1979 & Yu & Taulbee, 1975). Compared to upper airway infections, infections occurring at the deeper respiratory tract can cause higher morbidity and mortality (MacFarlane et al., 1993 & Tupasi et al., 1988), which is due to the damage of the lung function and the potential induction of other chronic diseases (Barker et al., 1991). In this case, the value of $10 \mu\text{m}$ is considered as a cutoff size, below which the droplets have a greater possibility of transmitting acute respiratory diseases (Weber & Stilianakis, 2008).

Human expiratory activity, including breathing, coughing, speaking and sneezing, can also determine the transmission of the respiratory pathogen through different factors, such as the number of droplets expelled by different expiratory activities, as well as the frequency of occurrence of the activity (Gralton et al., 2011). It was found that the intermittent expiratory activities (which include speaking, coughing and sneezing and can cause vibration of the vocal cords) are more likely to produce a great number of pathogen-laden droplets (Wainwright et al., 2009), while the continuous expiratory activity, i.e. breathing,

can only produce a small number of droplets carrying pathogen with low concentration (Stelzer-Braid et al., 2009 & Fabian et al., 2008). Furthermore, as one of the most common clinical symptoms of respiratory diseases, coughing occurs more frequently compared to sneezing and, therefore, it is considered as a more efficient way to transmit a respiratory pathogen (Couch et al., 1966).

The viability of different types of pathogen during transmission plays a very important role in the infection capability of respiratory diseases. Although many pathogen-laden droplets can be released by human expiratory activity, the pathogen may be inactivated due to various environmental factors, which can reduce the possibility of infection (Li et al., 2009). Bean et al (1982) found that influenza viruses might survive for different periods on various environmental surfaces, i.e. influenza A and B remained viable for 24-48 hours on nonporous surfaces or on a human hand, but survived less than 8-12 hours on tissues, cloth or paper. Hemmes et al (1960) investigated the viability of influenza and poliomyelitis viruses under different environmental conditions, and noted that the mortality of influenza virus was high at an ambient RH of 50-90% and comparatively low at the 15-40% RH. Conversely, the poliomyelitis virus showed a high survival-rate at the higher RH range and a very low survival-rate at the lower RH range. Moreover, in winter, the temperature and RH of the indoor environment provided the optimal survival conditions for influenza virus. However, the morbidity of poliomyelitis grew during summer due to the best indoor condition for survival of that virus. In addition, other factors, such as the type of pathogen, the concentration of pathogen in the expelled droplets, as well as different indoor places (i.e. hospital, rail cabin, etc.) may also affect the infection due to the respiratory pathogen transmission (Fennelly et al., 2004, Gralton et al., 2011, Ostrowsky, 2007 & Zhang & Li, 2012).

In the present study, a CFD simulation is carried out to investigate the dynamic characteristics, which includes the dispersion and evaporation processes of the droplets produced by coughing. The large eddy simulation (LES) approach is used to predict the flow field of coughing. The Lagrangian discrete phase model using the discrete random walk (DRW) model is employed to track a total 2084 droplets in the diameter range of 3-750 μm (Duguid, 1946). Studies with three different inlet and ambient conditions,

including the time-dependent cough velocity at the inlet and the ambient RH, are conducted to analyze the influence of those conditions on the droplet dispersion and evaporation.

3.2 Numerical Methodology

3.2.1 Governing equations

3.2.1.1 The LES approach

The LES approach is used to predict the turbulence of the flow field of coughing. The basic principle of such approach is to separate and resolve the large eddies that contain most of the energy through the spatially-filtered mass and momentum equations (Navier-Stokes equations), defined as

$$\frac{\partial \tilde{u}_i}{\partial x_i} = 0 \quad (3.1)$$

$$\frac{\partial \tilde{u}_i}{\partial t} + \tilde{u}_j \frac{\partial \tilde{u}_i}{\partial x_j} = -\frac{1}{\rho} \frac{\partial \tilde{p}}{\partial x_i} + \nu \frac{\partial^2 \tilde{u}_i}{\partial x_j^2} - \frac{\partial \tau_{ij}}{\partial x_j} \quad (3.2)$$

where τ_{ij} represents the subgrid-scale (SGS) stress tensor, describing the impact of small turbulence scales, and is expressed as

$$\tau_{ij} = \widetilde{u_i u_j} - \tilde{u}_i \tilde{u}_j \quad (3.3)$$

The SGS stress results in the exchange of momentum between the large (resolved) and small (subgrid) scales of motion (Bisoi et al., 2017), and needs to be modelled. In the present study, the dynamic Smagorinsky-Lilly model is adopted to model the SGS stress. This model considers the Smagorinsky model constant, C_S , as a function of space and time over a fairly wide range in order to avoid the damping of turbulent fluctuations in the presence of mean shear and in transitional flows (ANSYS, 2013). More details about the dynamic Smagorinsky-Lilly model are shown in Appendix C.

3.2.1.2 Energy equation

In order to solve the heat transfer between the cough flow and the ambient environment, the energy equation is required and is in the following form (Nijemeisland & Dixon, 2004),

$$\frac{\partial(\rho e)}{\partial t} + \nabla \cdot (\vec{u}\rho e) = \nabla \cdot (k_{eff}\nabla T - \sum_j \vec{J}_j \int_{T_{ref}}^T c_{p,j} dT) \quad (3.4)$$

where e represents the total energy, is given as the following equation.

$$e = h + \frac{u^2}{2} \quad (3.5)$$

where h , p , ρ and u are the sensible enthalpy, pressure, density and velocity of the injected fluid, respectively.

The details about the energy equation are shown in Appendix D.

3.2.1.3 Discrete phase model

Since the droplet volume fraction is very low in the cough flow, the Eulerian-Lagrangian method is used in this study, where the continuous phase (the flow field) is modelled by the Eulerian method, i.e. by solving the Navier-Stokes equations, while the discrete phase (the droplets) is modelled by the Lagrangian method, i.e. by tracking the motion of the droplets. The discrete phase can exchange mass, momentum and energy with the continuous phase.

The trajectory of a discrete droplet is predicted by stepwise integrating the force balance equation with an implicit integration scheme (see Appendix J for details). The force balance equation equates the forces acting on that droplet with the droplet inertia and is based on Newton's second law of motion, with respect to the discrete time steps, as shown below (ANSYS, 2013),

$$\frac{d\vec{u}_p}{dt} = F_D(\vec{u} - \vec{u}_p) + \frac{\vec{g}(\rho_p - \rho)}{\rho_p} \quad (3.6)$$

where \vec{u} and \vec{u}_p represent the velocity of the continuous and discrete phase, respectively, and ρ and ρ_p are the density of the fluid and droplet, respectively. On the right-hand side, the term of $F_D(\vec{u} - \vec{u}_p)$ is the drag force per unit droplet mass, and

$$F_D = \frac{18\mu}{\rho_p d_p^2} \frac{C_D Re_r}{24} \quad (3.7)$$

where d_p is the diameter of the droplet, μ is the molecular viscosity of the fluid, and Re_r represents the relative Reynolds number, defined as

$$Re_r \equiv \frac{\rho d_p |\vec{u}_p - \vec{u}|}{\mu} \quad (3.8)$$

Based on the Stokes-Cunningham drag law (Ounis et al., 1991), F_D acting on the droplets can be expressed as

$$F_D = \frac{18\mu}{\rho_p d_p^2 C_C} \quad (3.9)$$

A Cunningham correction is made by the factor, C_C , which is obtained from

$$C_C = 1 + \frac{2\lambda}{d_p} (1.257 + 0.4e^{-(1.1d_p/2\lambda)}) \quad (3.10)$$

where λ represents the molecular mean free path. It is noted that, when the Stokes-Cunningham drag law is adopted, C_C will satisfy $C_C = \frac{24}{C_D Re_r}$, according to Eqns. (3.7) and (3.9).

The effect of the turbulence in the continuous phase on the droplet dispersion is accounted for by the use of the stochastic tracking model, which considers the random effects of the instantaneous velocity fluctuations on the droplet trajectory through the stochastic method, The DRW model is used in this study. For the strongly nonhomogeneous flows which are dominated by diffusion, the small droplets should distribute in a uniform way, and the DRW model will predict a tendency for such droplets to concentrate in the regions with low turbulence (ANSYS, 2013). The details about the DRW model are shown in Appendix I. Moreover, during the airborne transmission, two or even more droplets may collide and coalesce together into a new droplet, slightly larger in size. Therefore, the processes of collision and coalescence may also affect the size distribution of droplets and are taken into consideration in the discrete phase model. The present study employs the stochastic collision model to predict the collisions occurring to the droplets produced by coughing. The details about the stochastic collision and coalescence are shown in Appendix K.

3.2.2 Computational domain and grid

The computational domain is in a cuboid shape and is illustrated as Figure 3.3, in which the “x”, “y” and “z” axes represent the axial (streamwise), lateral and vertical directions, respectively. The inlet is a circular orifice of diameter $d=0.0217$ m, representing the

average human mouth diameter (Gupta et al., 2009). The centre of the inlet is denoted by $(0, 0, 0)$, which is also the origin of the coordinate system.

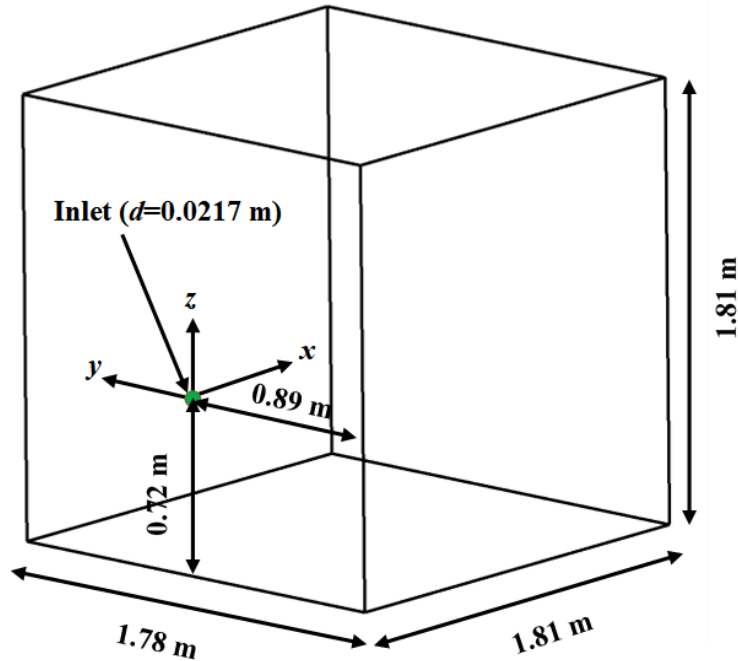


Figure 3.3: Schematic of the computational domain along with its dimensions.

The computational domain and grid are generated by using ICEM CFD 16.0. Irregular unstructured polyhedral grids are implemented to reduce the computational expense without lowering the accuracy and to improve the residual convergence. The grid resolution is 1 mm at the inlet and 5 mm in the cone region with the global growing ratio of 1.15, as exhibited in Figure 3.4, where it can be clearly seen that the grid in the cone region is much finer than that in the global region (outside of the cone region). The total number of computational cells is approximately 7.3 million. The grid independence test for the LES modelling is shown in Appendix H.

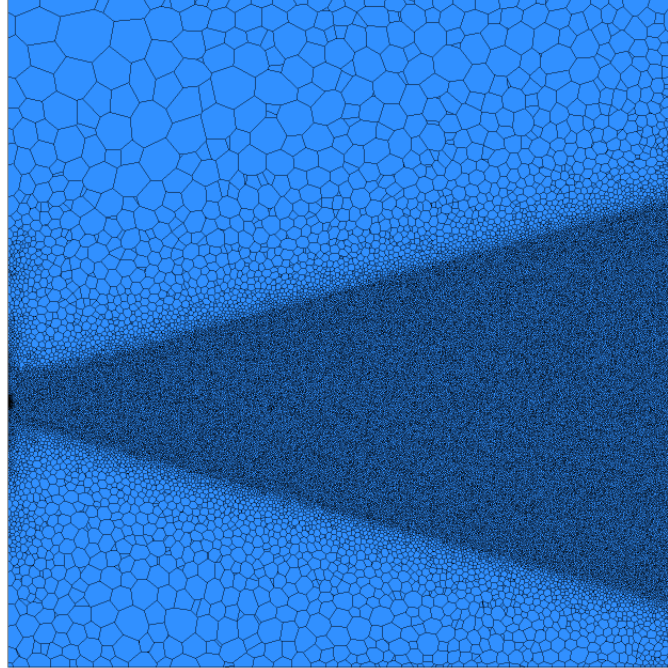


Figure 3.4: Grid distribution on the x - z plane ($y=0$) of the computational domain.

3.2.3 Droplet conditions

The size distribution of the droplets expelled by coughing is not unique, due to the physiological variability of different human subjects (Aliabadi et al., 2010). It is necessary for the CFD modelling to obtain a representative distribution which can cover a wide range of droplet sizes. The present study uses the work of Duguid (1946), from which 2084 droplets in the diameter range of 3-750 μm are considered to be released during one cough. These 2084 droplets are grouped into 15 sizes, and the majority concentrates in the range 6-12 μm , as shown in Table 3.2, where the mass flow rate of each size of droplets are calculated from the following equation,

$$\dot{m}_p = \frac{N\rho_p\pi d_p^3}{6\Delta t} \quad (3.11)$$

where N represents the number of droplets per diameter class, and Δt is the time step size, which is 0.001 *secs*.

This ensemble of droplets is injected in the range 0.042-0.136 *secs* which covers the time corresponding to the peak of the cough velocity, as illustrated in Figure 3.5. The injection

speed is zero, which implies that all the droplets are driven initially by the flow field from the mouth. Less than 30 droplets are set to be injected per time step in order to reduce the occurrence of collision. The droplets are staggered at 0.01 m downstream from the inlet to reduce the possibility of the backflow (Aliabadi et al., 2010). Moreover, each droplet consists of multi-components, i.e. 94% volume fraction of the pure water, which is evaporative, and the remaining 6% is of the same physical properties of the pure water but non-evaporative (Aliabadi et al., 2010). The non-evaporative portion represents the mucus and physiological electrolytes which carry different infectious agents, including viruses, pathogens, fungi and bacteria. During the airborne transmission of the droplets, the pure water will evaporate, and the non-evaporative portion will remain to form a droplet nucleus and suspend in the ambient environment for a longer period. The temperature of the droplets is set as 32 °C (305.15 K) (Zhu et al., 2006).

Table 3.2: Droplet size distribution (reproduced from Duguid (1946)).

Diameter class, μm	Number of droplets (N)	Mass flow rate, kg/sec
3	76	1.07442e-9
6	1041	1.17621e-7
12	386	3.43816e-7
20	127	5.27788e-7
28	47	5.28726e-7
36	45	1.07488e-6
45	38	1.81309e-6
62.5	38	4.85761e-6
87.5	27	9.12003e-6
112.5	32	2.38565e-5
137.5	30	4.08346e-5
175	83	2.35718e-4
225	47	2.74349e-4
375	40	1.10447e-3
750	27	5.74322e-3
Total	2084	7.44083e-3

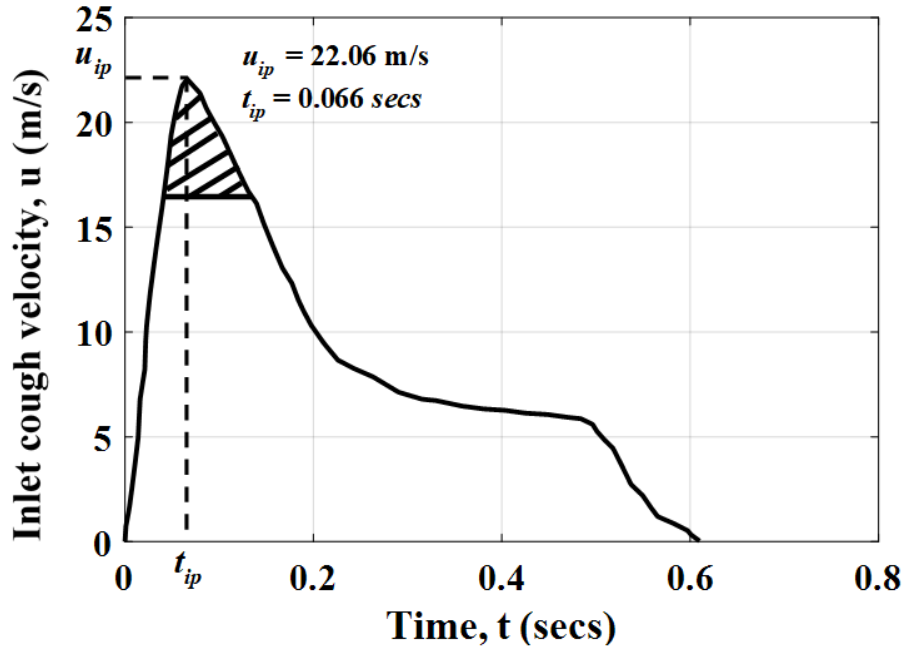


Figure 3.5: Duration of the droplet injection (shaded part) (reproduced from Gupta et al. (2009)).

3.2.4 Boundary and ambient conditions

Three simulations under different inlet and ambient conditions, including the time-dependent cough velocity at the inlet and the ambient RH, are conducted to investigate the impacts of those conditions on the droplet evaporation and dispersion, and are summarized in Table 3.3. Two cough velocity profiles obtained from the work of Gupta et al (2009), as shown in Figure 3.6, are analyzed by Cases #1 and #2. The peak values u_{ip} of the two velocity profiles are 22.06 and 10.81 m/s, corresponding to the time t_{ip} of 0.066 and 0.073 secs, respectively. According to the following equation (Wei & Li, 2017), the temporal mean velocities u_m for the two profiles are 8.81 and 4.79 m/s, respectively.

$$u_m = \frac{1}{t_{iss}} \int_0^{t_{iss}} u(t) dt \quad (3.12)$$

where t_{iss} represents the cough duration, which is 0.61 and 0.40 secs for Cases #1 and #2, respectively. It can be seen that both the peak velocity u_{ip} and the temporal mean velocity u_m for Case #2 are around half of the values for Case #1. Moreover, the influence of the ambient RH is examined by Cases #1 and #3. The mass fractions of water vapour in the

ambient environment are 0.80% and 1.27% corresponding to the RH of 50% and 80%, respectively. For all the three cases, the direction of the inlet cough velocity is set as normal to boundary, which satisfies that the fluid is issued from the inlet into the domain with the velocity in the streamwise direction. Based on Zhu et al. (2006), the temperature of the fluid at the inlet is defined as 32 °C (305.15 K), which is the same as that of the droplets, and the inlet turbulence intensity of the flow field of coughing is 10% of u_m . The hydraulic diameter is set as 0.0217 m, which is equal to the average human mouth diameter (Gupta et al., 2009). The spectral synthesizer algorithm (Kraichnan, 1970 & Smirnov et al., 2001) is selected to generate the synthetic turbulence at the inlet, through creating a velocity vector field without divergence from the summation of 100 Fourier harmonics (ANSYS, 2013). The ambient temperature is defined as 21.5 °C (294.65 K), and the surrounding fluid velocity is set as zero due to the quiescent ambient condition.

For all the three cases, the fluid injected from the inlet is defined as two-species alveolar air, which is usually considered as the flow caused by human expiratory activity, e.g. coughing, breathing, speaking and sneezing. The two species include air and water vapour, with the mole fraction 93.8% and 6.2%, respectively (Saladin, 2003). The properties of the injected fluid are shown in Appendix F.

Table 3.3: Three cases in different inlet and ambient conditions.

Case number	u_{ip} , m/s	u_m , m/s	Ambient temperature, K	Mass fraction of water vapour	Ambient RH
Case #1	22.06	8.81	294.65	0.8%	50%
Case #2	10.81	4.79	294.65	0.8%	50%
Case #3	22.06	8.81	294.65	1.27%	80%

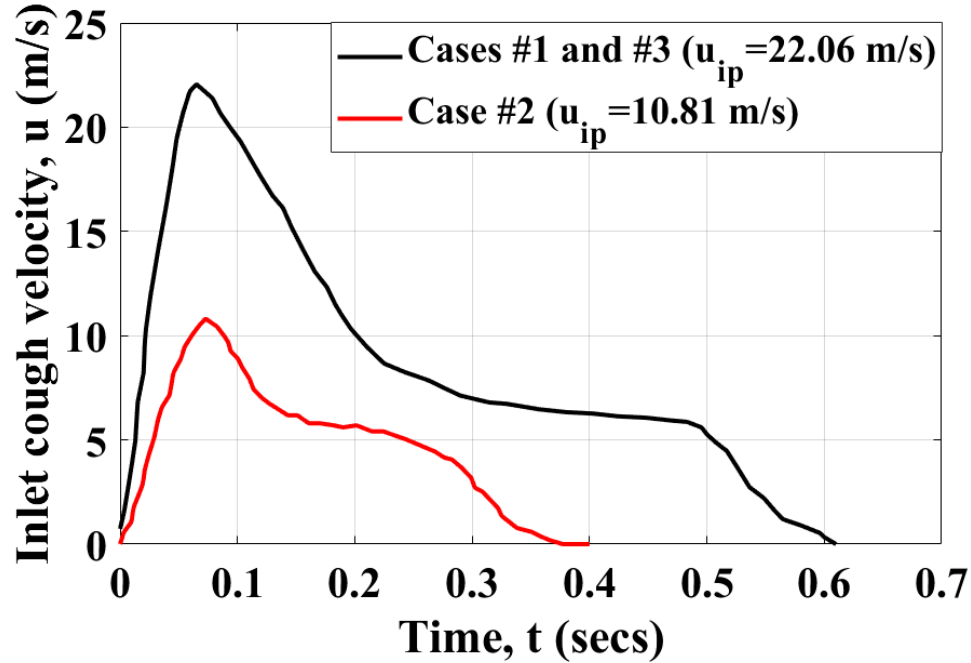


Figure 3.6: Inlet cough velocity profiles employed for Cases #1, #2 and #3 (reproduced from Gupta et al. (2009)).

For all the three cases, all the six walls of the computational domain are defined as no-slip adiabatic walls. The boundary conditions for the discrete phase on the inlet and six walls of the computational domain need to be specified. For the inlet, the “reflect” boundary condition is used, which means the droplet will rebound after colliding with the boundary and, therefore, the backflow of the droplet can be effectively prevented. A restitution coefficient e with the value varying between 0 and 1 determines the amount of momentum that the droplet will retain after the collision, and is defined as (Wakeman & Tabakoff, 1982)

$$e = \frac{\vec{v}_{p2}}{\vec{v}_{p1}} \quad (3.13)$$

where \vec{v}_{p1} and \vec{v}_{p2} represent the velocity of the droplet before and after the collision, respectively. A restitution coefficient equal to 1 infers that the droplet retains all of its momentum when rebounding off the boundary, which can be regarded as an elastic collision. While a restitution coefficient equal to 0 indicates that none of the momentum

will be retained by the droplet after the collision, i.e. an inelastic collision. The value of the restitution coefficient is dependent on the impact angle formed by the collision.

The “trap” boundary condition is employed for all six walls to match the physical reality, which means the droplet will stay at the wall when it collides with the wall. The remaining evaporative portion of the droplet keeps evaporating and passes into the vapour phase, and enters the computational cell which is adjacent to the wall (ANSYS, 2013).

3.2.5 CFD solver

The commercial CFD packages, FLUENT 16.0 is used to carry out the simulation and CFD-Post 16.0 is used to post-process the results. A finite volume method is employed to solve the governing equations with double precision. The pressure-based solver is adopted since it is suitable for incompressible flows. The algorithm of the Semi-Implicit Method for Pressure-Linked Equations (SIMPLE) by Patankar et al. (1972), is employed as the pressure-velocity coupling method. For the pressure interpolation, the second-order scheme is used as it can acquire acceptable solutions for most cases (ANSYS, 2014), and for the gradient evaluation, the least squares cell-based scheme is performed in order to obtain a more accurate second-order interpolation on irregular unstructured polyhedral grids which are applied in the present study. To solve the temporal discretization, the bounded second order implicit formulation is carried out as it can provide a higher accuracy and better stability than other types of formulation. A time step size of 0.001 *secs* is used to reduce the computational expense. The simulation is run for 4 *secs* in total of the flow time which is sufficient to characterize the dynamic development of the droplets produced by coughing in the computational domain. The residual convergence criterion is set as 10^{-6} for the energy equation and 10^{-3} for the other governing equations, including continuity, momentum and species transport equations, etc., and a maximum number of iterations per time step, i.e. inner loop iterations, is set as 100. The central differencing discretization scheme is performed for momentum, water vapour species transport and energy since it minimizes the numerical diffusion and provides the highest accuracy in resolving the large turbulence scales. Therefore, it is considered as the ideal choice for the LES approach.

3.3 Results and Discussion

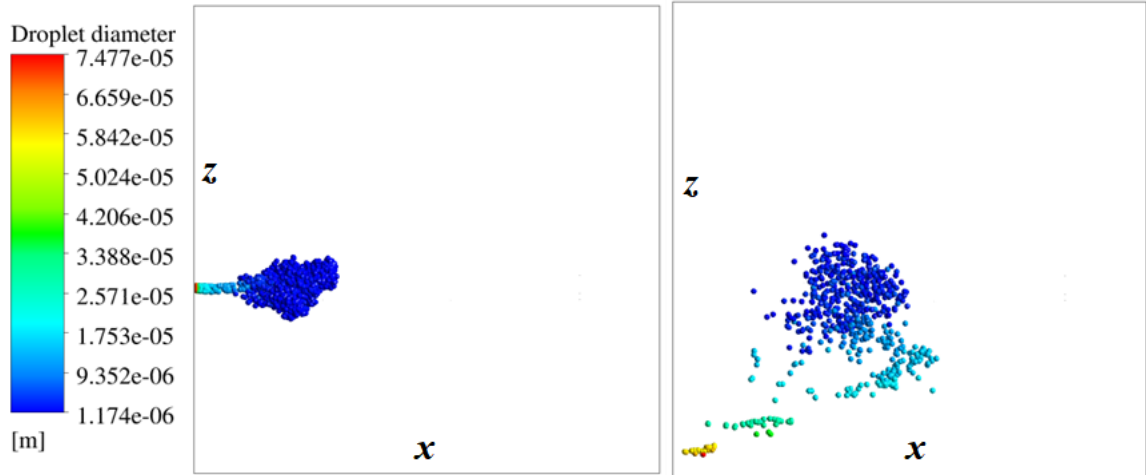
An understanding of the dispersion and evaporation of the exhaled droplets plays an important role not only in investigating the airborne transmission mechanism of the infectious respiratory diseases, but also in developing the effective control methods (Xie et al., 2007). In the present study, the numerical results in terms of the dispersion and evaporation of the droplets produced by coughing under different inlet and ambient conditions are presented. The effect of the time-dependent cough velocity at the inlet is explored in Cases #1 and #2, whilst the influence of the ambient RH is examined in Cases #1 and #3.

3.3.1 Droplet dispersion

The dispersion of droplets produced by coughing is analyzed in two different aspects, including the contours of droplet diameters and the penetration distance of the droplets from the mouth.

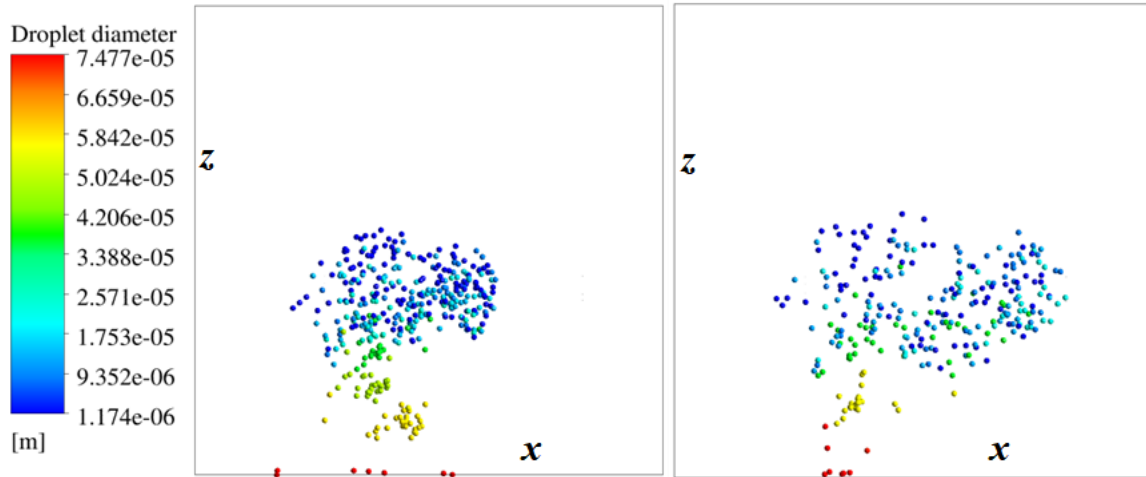
3.3.1.1 Contours of droplet diameters

The contours of droplet diameters give a clear visualization of the transient nature of the location of droplets in various sizes, which, in turn, provides a more graphic and easier understanding of the droplet dispersion process. Figure 3.7, obtained from Case #1, shows the contours of droplet diameters at six different time on the x - z plane ($y=0$), which visualizes a droplet dispersion trend in the streamwise and vertical directions. It should be noticed that at each time, all the droplets within the computational domain are integrated on the x - z plane. It can be seen clearly that at the time 0.15 *secs* (Figure 3.7 (a)), the total 2084 droplets have been injected into the domain. As expected, the larger the diameter, the faster the droplets fall to the ground due to the effect of the gravity. The smaller droplets with the diameter $d_p \leq 10 \mu\text{m}$ remain suspended for a longer period.



(a)

(b)



(c)

(d)

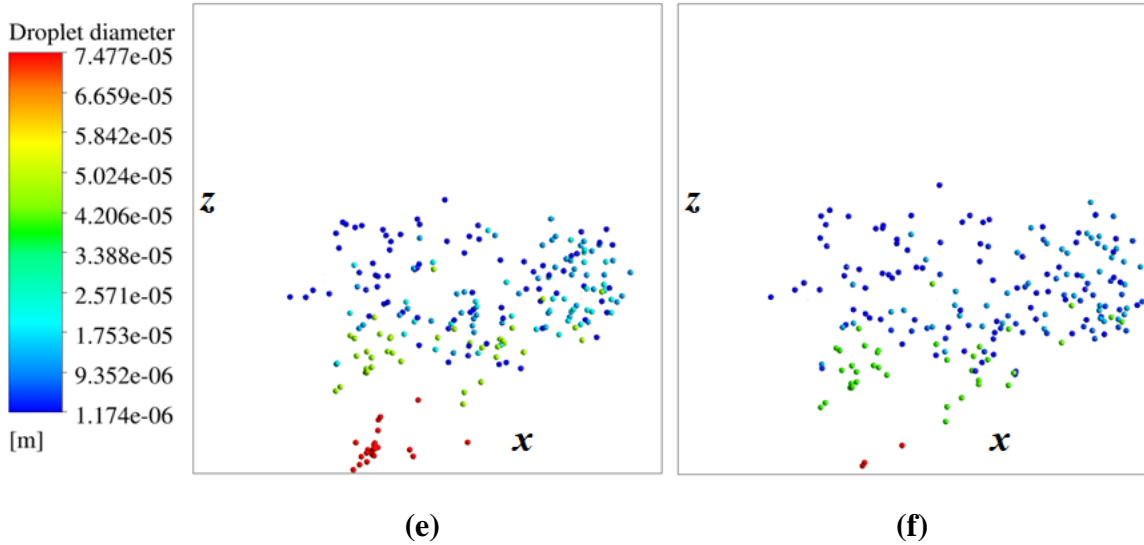
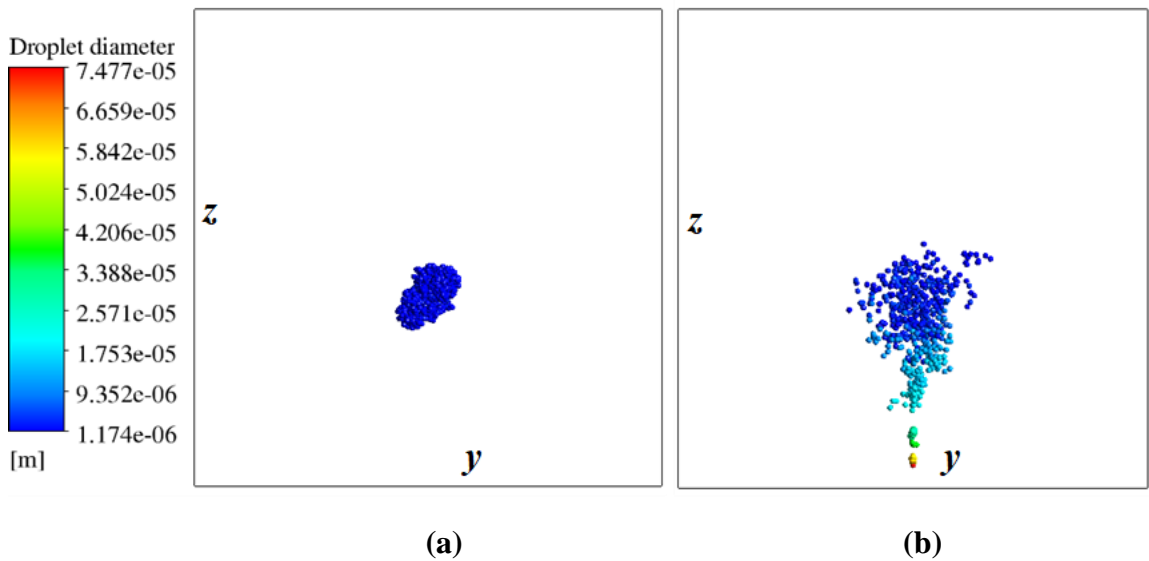


Figure 3.7: Contours of the droplet diameters at (a) 0.15 secs, (b) 0.5 secs, (c) 1 sec, (d) 2 secs, (e) 3 secs and (f) 4 secs on the x - z plane.

Figure 3.8 exhibits the contours of the droplet diameters on the y - z plane ($x=0$) to visualize a droplet dispersion trend in the lateral and vertical directions. At each time, all the droplets within the computational domain are integrated on the y - z plane. It is found that, the smaller droplets display a higher rate of dispersion, which reveals that the drag force becomes more dominant on the droplet than the gravity as the droplet size decreases.



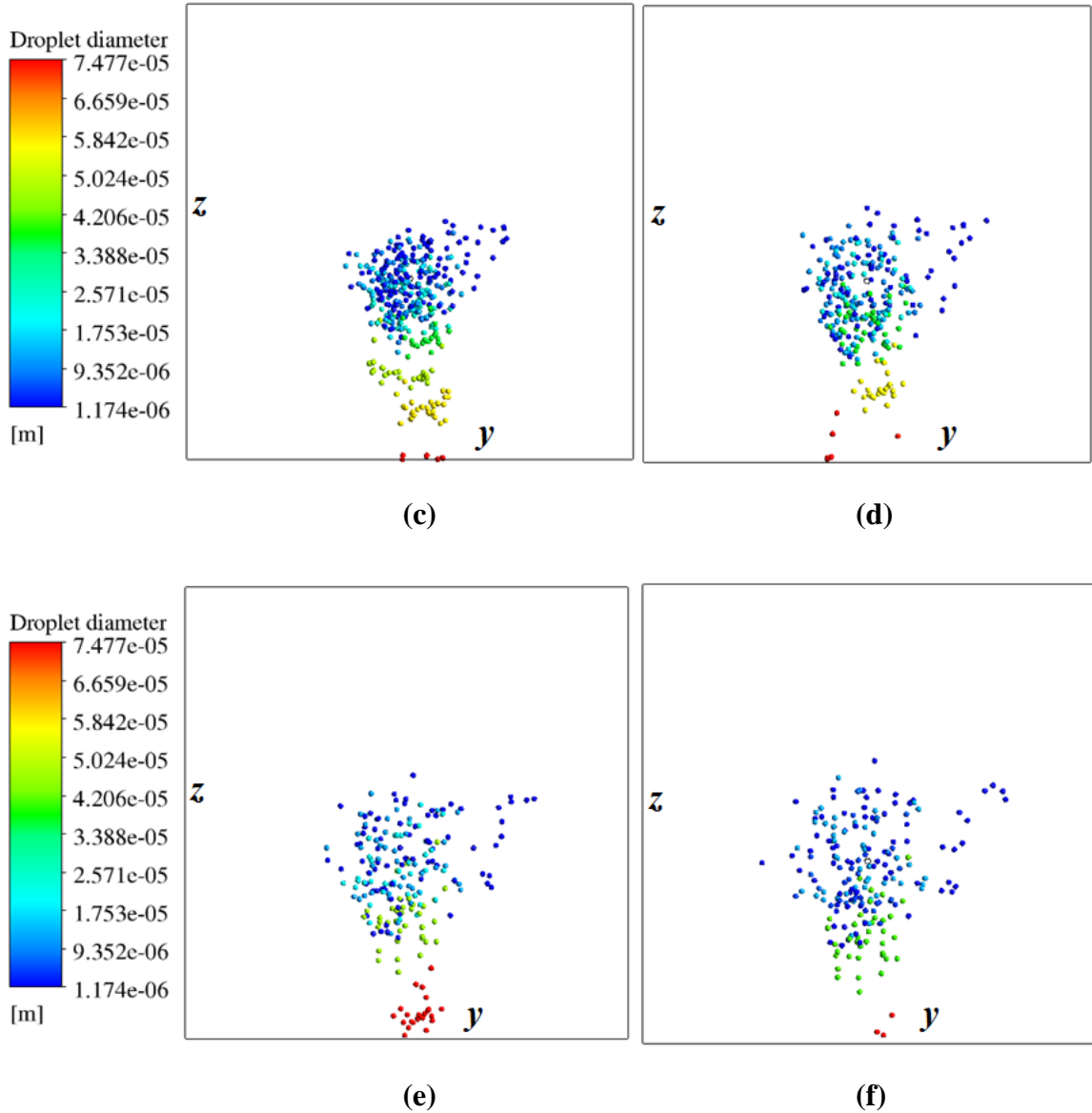


Figure 3.8: Contours of the droplet diameters at (a) 0.15 secs, (b) 0.5 secs, (c) 1 sec, (d) 2 secs, (e) 3 secs and (f) 4 secs on the y-z plane.

3.3.1.2 Effect of the ambient RH

The droplet penetration distance from the mouth can be described by the mean ($\langle l \rangle$) and maximum (l_m) penetrations of the droplets. The mean penetration distance $\langle l \rangle$ is calculated by

$$\langle l \rangle = \frac{\sum_{i=1}^N l_i}{N} \quad (3.14)$$

where N represents the total number of droplets suspended within the computational domain, and l_i is the absolute value of the distance between the current position of the i^{th} droplet and the mouth. Figure 3.9 shows the mean and maximum penetrations of the droplets under two different values of the ambient RH. It can be seen that the mean and maximum penetrations increase with time for both cases, and the increase becomes more and more gradual due to the gradual decrease in the droplet velocity, which is caused by the decrease in the velocity of the flow field. At 4 secs, the values of $\langle l \rangle$ and l_m for the case with a lower RH (Case #1) are around 1.20 and 1.80 m, respectively, which are slightly higher than those for the case with a higher RH (Case #3) (1.14 and 1.65 m, respectively). During the entire 4-second flow time, the case with a lower RH (Case #1) shows higher values of $\langle l \rangle$ and l_m by 3.29% and 9.52% compared to the case with a higher RH (Case #3), respectively. Therefore, a higher RH of the ambient air slightly weakens the droplet penetration.

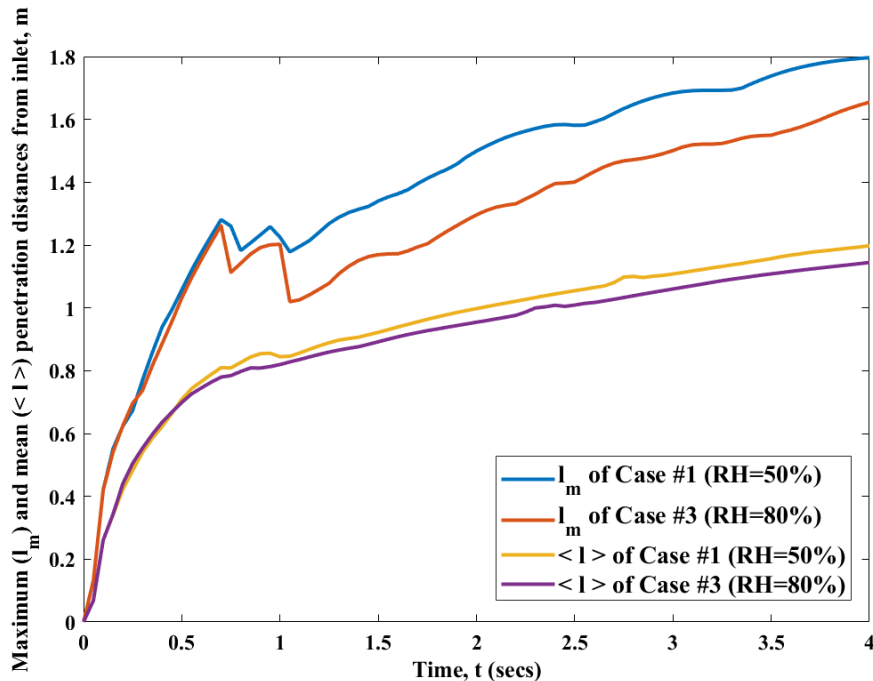


Figure 3.9: Comparison of the maximum penetration distance l_m and mean penetration distance $\langle l \rangle$ of the droplets under different ambient RH.

3.3.1.3 Effect of the inlet cough velocity

The effect of the inlet time-dependent cough velocity on the droplet penetration distance from the mouth is investigated, and the mean and maximum penetrations of the droplets under two different inlet cough velocities are presented in Figure 3.10. From the figure it is found that for both cases, the mean and maximum penetration distances increase more and more gradually with time. At the time of 4 *secs*, the maximum values of $\langle l \rangle$ and l_m for the case with a lower peak velocity (Case #2) are approximately 0.69 and 1.44 m, respectively, which are less than those for the case with a higher peak velocity (Case #1) (1.20 and 1.80 m, respectively). During the entire 4-second flow time, the case with a higher peak velocity (Case #1) gives higher values of $\langle l \rangle$ and l_m by 39.74% and 27.06% in compare to the case with a lower peak velocity (Case #2), respectively. This infers that the inlet cough velocity has a much more significant influence on the penetration of the droplets, in compare to the ambient RH (see Figure 3.9), and as expected the higher the cough velocity, the longer distance the droplets could travel.

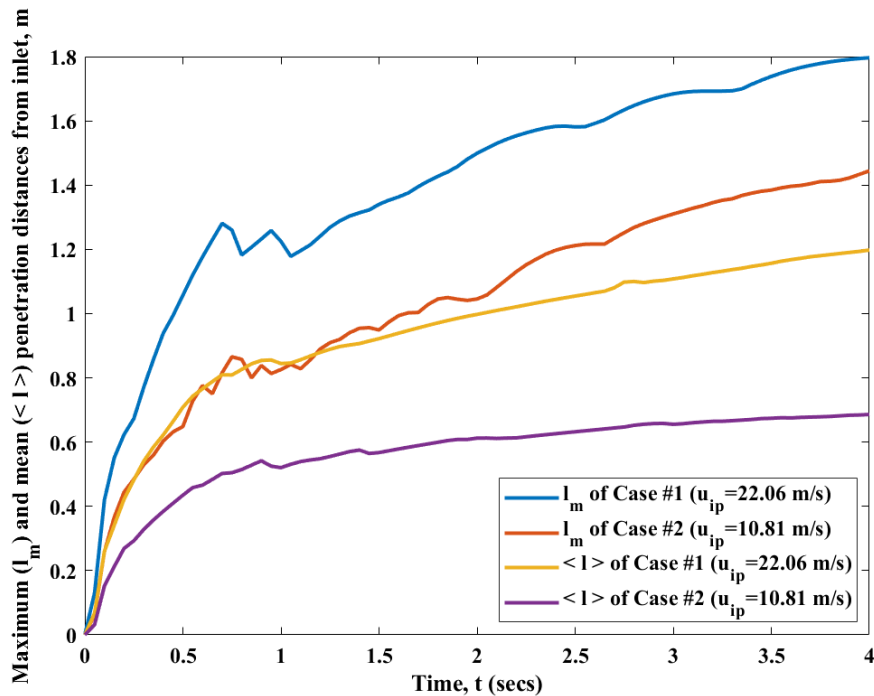


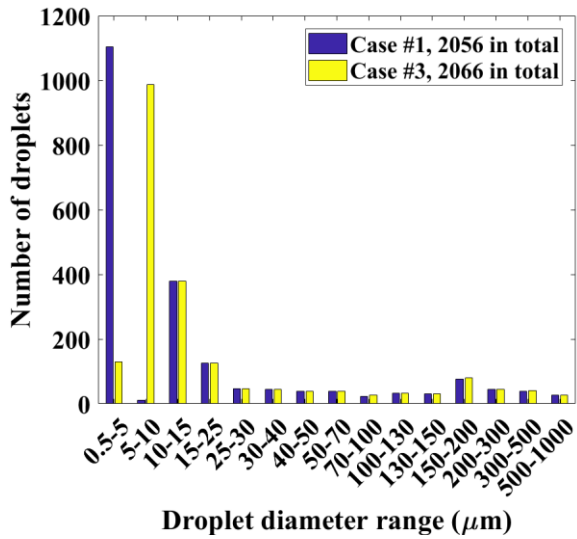
Figure 3.10: Comparison of the maximum penetration distance l_m and mean penetration distance $\langle l \rangle$ of the droplets under different inlet cough velocities.

3.3.2 Droplet evaporation

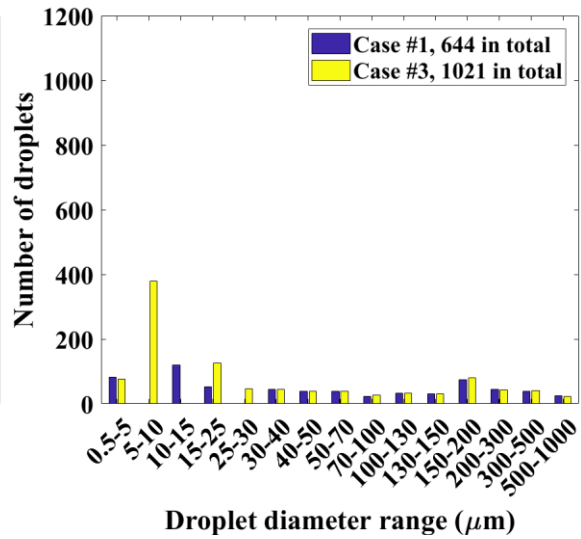
The evaporation of the droplets produced by coughing is also analyzed in two different aspects, the droplet size distribution at different time and the variation of the overall mean droplet diameter with time.

3.3.2.1 Effect of the ambient RH

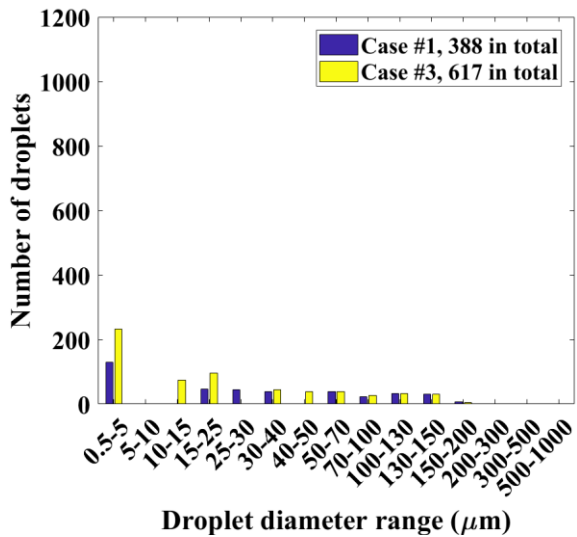
Figure 3.11 shows the comparison of the droplet size distribution at different time between Case #1 (50% RH) and #3 (80% RH). The figure shows the variation of droplet numbers in different diameter ranges with time. At 0.15 *secs* (Figure 3.11 (a)), it can be seen clearly that there are big differences in the droplet numbers between Cases #1 and #3 in the diameter range of 0.5-5 μm and 5-10 μm , compared to other ranges. In the range of 0.5-5 μm , the numbers of droplets for Cases #1 and #3 are 1103 and 129, whereas in the range of 5-10 μm , there are 10 and 987 droplets for Cases #1 and #3, respectively. The droplets are injected into the computational domain from the smallest size (3 μm) to the largest size (750 μm) successively, and the evaporation takes place immediately once the droplets are injected, which results in a decrease of the droplet diameter and an increase of the droplet number in the smaller diameter range. At 0.5 *secs* (Figure 3.11 (b)), the numbers of droplets in the range 0.5-5 μm and 5-10 μm reduces dramatically for both Cases #1 and #3, compared to the previous time, which is due to the coalescence and precipitation of the droplets. Moreover, as time progresses further, the large droplets, which are in the diameter range $d_p \geq 100 \mu\text{m}$, keep evaporating and precipitating on the ground and, as a result, the numbers of droplets decrease gradually to zero.



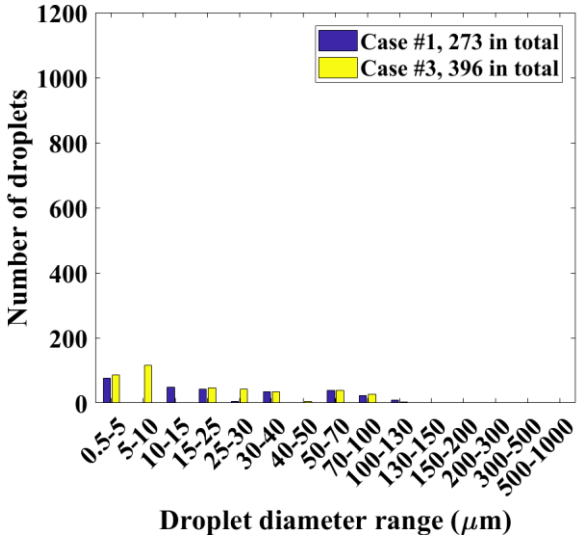
(a)



(b)



(c)



(d)

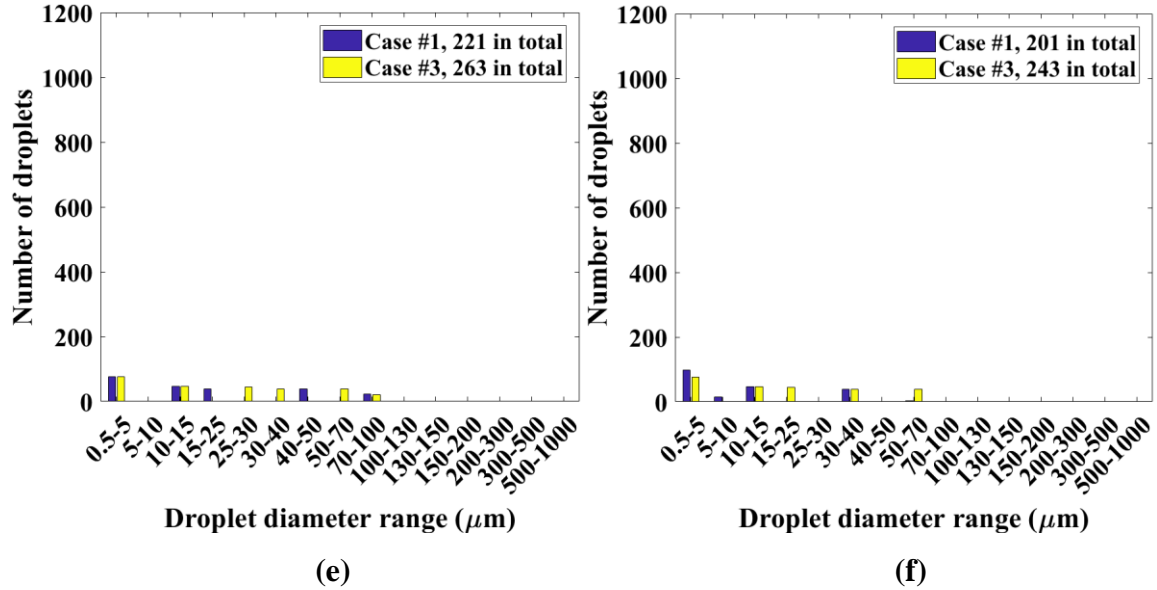


Figure 3.11: Droplet size distributions under different ambient RH at (a) 0.15 secs, (b) 0.5 secs, (c) 1 sec, (d) 2 secs, (e) 3 secs and (f) 4 secs.

The variation of the total number of suspended droplets with time is illustrated in Figure 3.12. All the 2084 droplets are injected into the computational domain by 0.136 secs for both Cases #1 and #3. After 0.136 secs, the total number of droplets suspended within the computational domain keeps reducing as time progresses due to the precipitation of the large droplets. When coalescence occurs to the droplet nuclei, which consist of 6% volume fraction of the non-evaporative water and evolve from the complete evaporation of the droplets (Aliabadi et al., 2010 & Wells, 1934), the new-formed droplet nuclei in larger sizes also fall to the ground without evaporation, which results in a reduction of the number of suspended droplets as well. It can be seen that after approximately 1.1 secs, the variation of the number of suspended droplets with time slows down, but with a steady decline trend, which is due to the dispersion of the droplets. As time progresses, the dispersion rate of the suspended droplets becomes higher (see Figure 3.8), which results in a reduction of the occurrence of droplet coalescence and precipitation. Furthermore, it is found from Figure 3.12 that during the entire flow time, the case with a higher RH (Case #3) shows a 22.74% higher number of droplets than the case with a lower RH (Case #1), which indicates that a higher ambient RH slows down the coalescence and precipitation of the droplets.

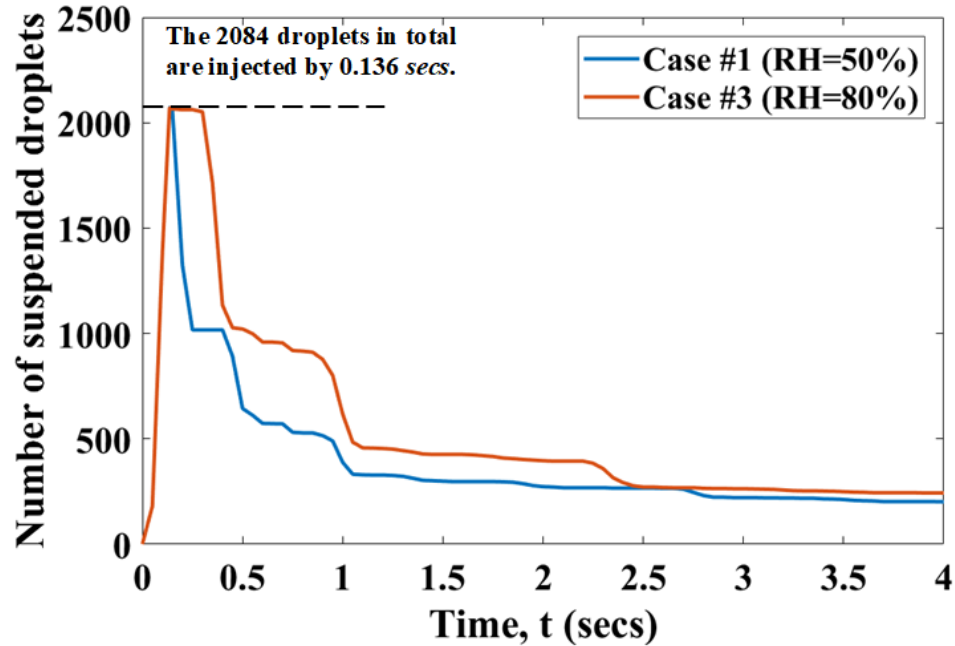


Figure 3.12: Comparison of the time history of total number of droplets suspended within the computational domain under different ambient RH.

Figure 3.13 shows the time history of the overall mean diameter of the droplets for Cases #1 and #3, where $\langle d_p \rangle$, also known as the arithmetic average of the droplet diameter, is calculated by

$$\langle d_p \rangle = \frac{\sum_{i=1}^N d_{pi}}{N} \quad (3.15)$$

where N represents the total number of the droplets suspended within the computational domain, and d_{pi} is the diameter of the i^{th} droplet. From the figure it can be seen that for both Cases #1 and #3, $\langle d_p \rangle$ increases drastically until 0.5 secs, followed by a sharp fall until approximately 1 sec, and then decreases gradually with time. Due to the higher collision rate before 0.5 secs, the number of suspended droplets reduces dramatically, and the diameters of the droplets increase due to the coalescence, which results in a sudden growth of the mean diameter. The subsequent decrease of $\langle d_p \rangle$ is caused by the precipitation and evaporation of the droplets. Furthermore, before approximately 2.3 secs, $\langle d_p \rangle$ is smaller for the case with a higher RH (Case #3) compared to the case with a lower RH (Case #1), which implies that a higher ambient RH results in a lower coalescence rate of the droplets. Then, after 2.3 secs, $\langle d_p \rangle$ for Case #3 exceeds that for Case #1, but still decreases

gradually, which infers that the evaporation of droplets is weakened by a higher RH of the ambient environment.

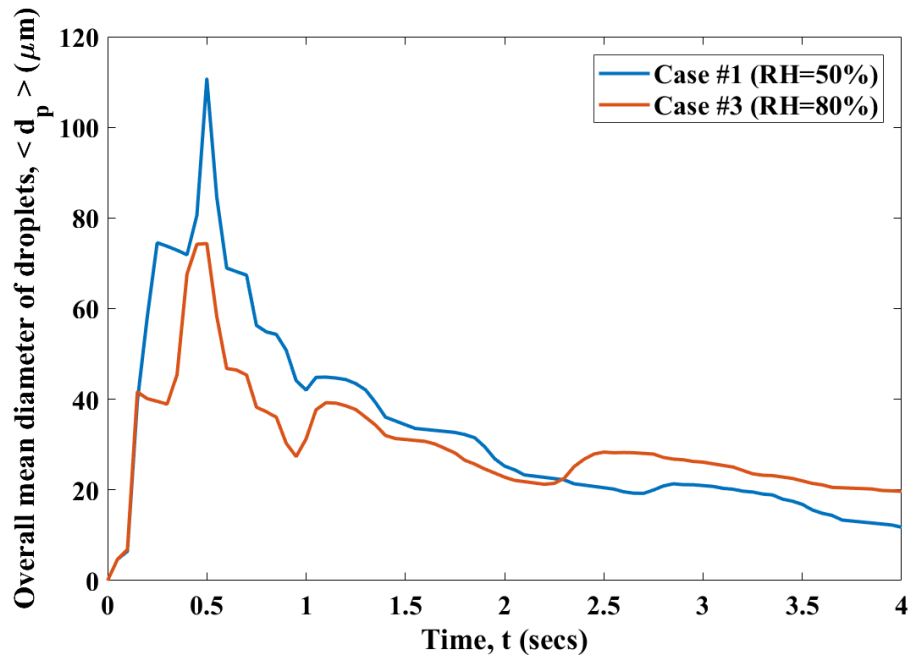
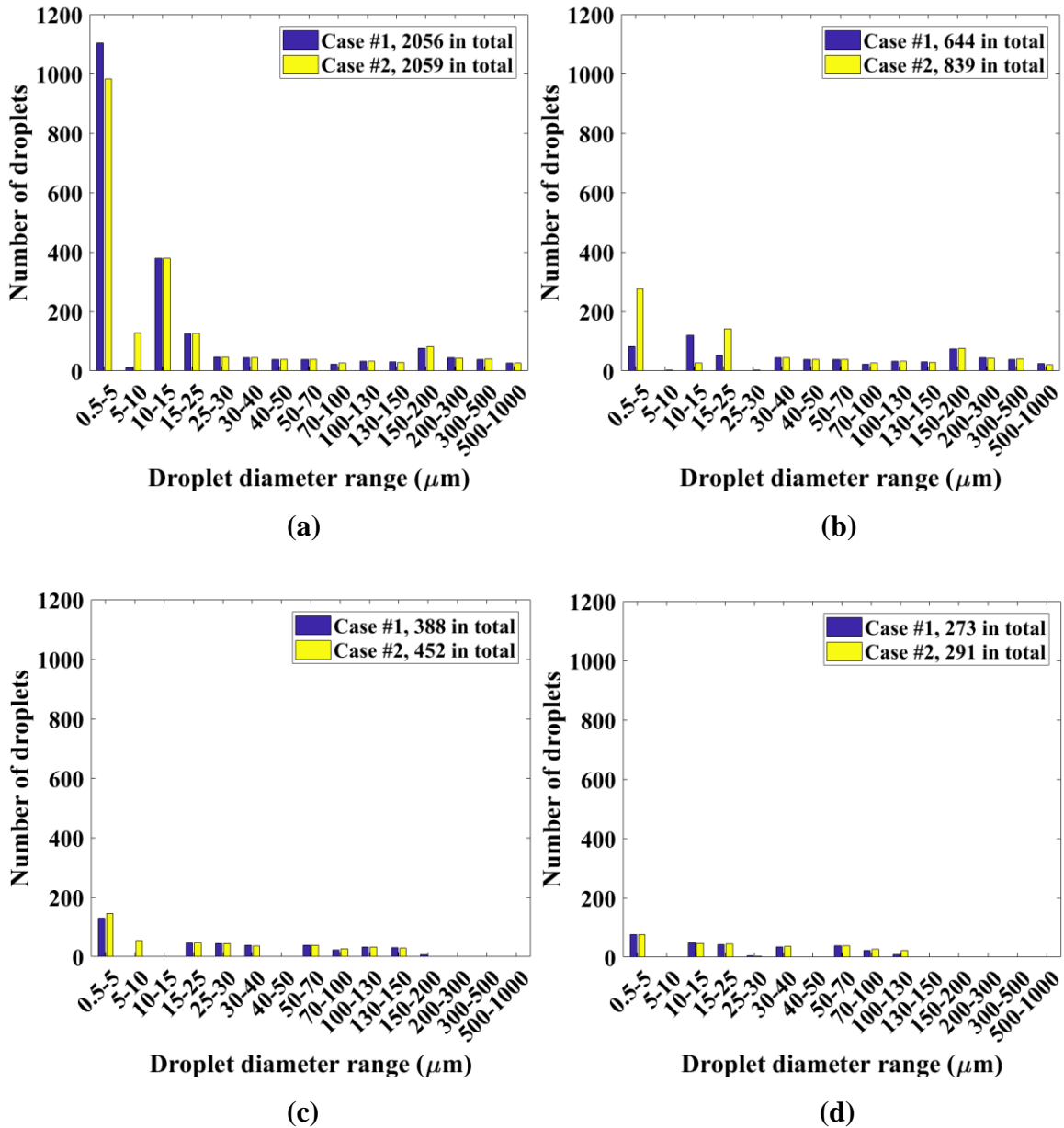


Figure 3.13: Comparison of time history of overall mean diameter of the droplets under different ambient RH.

3.3.2.2 Effect of the inlet cough velocity

In order to investigate the influence of the time-dependent cough velocity at the inlet on the evaporation of the droplets, the droplet size distributions under two different inlet cough velocities at different time are presented in Figure 3.14. It is found that at 0.15 *secs* (Figure 3.14 (a)), the differences in the droplet numbers between the two cases are larger in the diameter ranges of 0.5-5 μm and 5-10 μm , compared to other diameter ranges. In the range of 0.5-5 μm , the number of the droplets is higher for the case with a higher inlet cough velocity (Case #1) than that for the case with a lower inlet cough velocity (Case #2). But, it is just opposite for the diameter range of 5-10 μm between the two cases. Compared to Figure 3.11 (a), it can be seen clearly that at 0.15 *secs*, the difference in number of droplets between Cases #1 and #2 is much smaller than that between Cases #1 and #3, which means that the inlet cough velocity has a much weaker effect on the droplet size distribution than the ambient RH. Furthermore, as time progresses, the differences in droplet size

distribution and total number of suspended droplets between Case #1 and #2 decrease gradually, as shown in Figure 3.14, which infers that the impact of the inlet cough velocity on the dynamic development of the droplets produced by coughing gradually reduces with time.



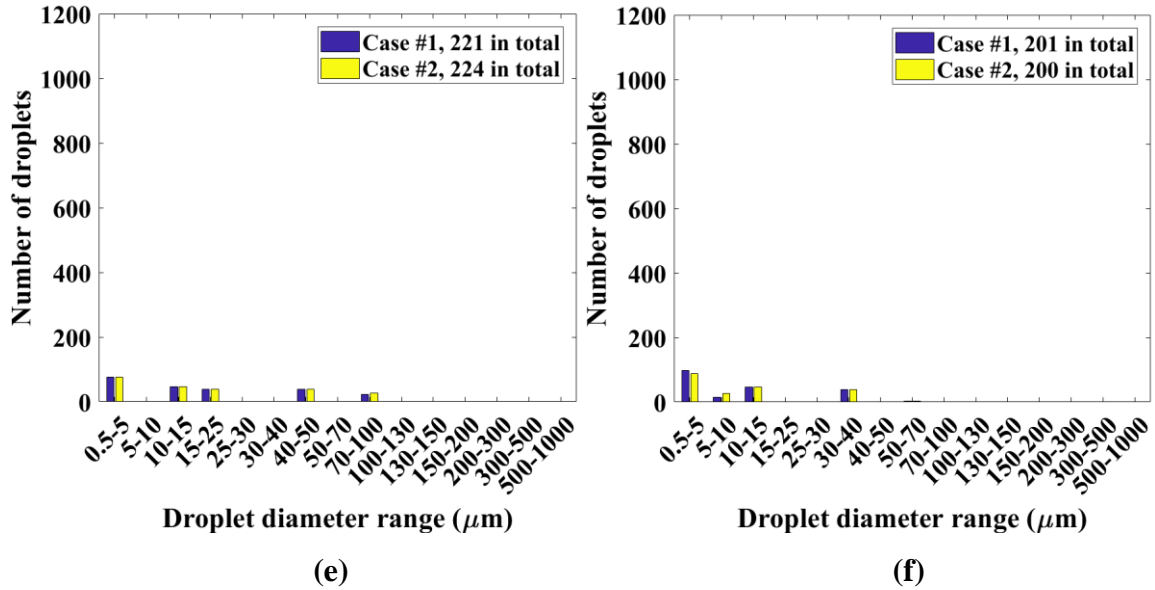


Figure 3.14: Droplet size distributions under different inlet cough velocities at (a) 0.15 secs, (b) 0.5 secs, (c) 1 sec, (d) 2 secs, (e) 3 secs and (f) 4 secs.

The comparison of the time history of total number of droplets suspended within the computational domain between Case #1 and #2 is illustrated in Figure 3.15. It can be seen clearly that the time history profiles for these two cases are almost the same, i.e. a sharp decline from approximately 0.136-1.1 secs and a slow but steady decline from 1.1-4 secs. During the entire 4-second flow time, the case with a lower inlet cough velocity (Case #2) shows a 3.01% higher number of droplets than the case with a higher inlet cough velocity (Case #1), which indicates that the inlet cough velocity has a much less impact on the coalescence and precipitation of the suspended droplets, compared to the ambient RH (see Figure 3.12).

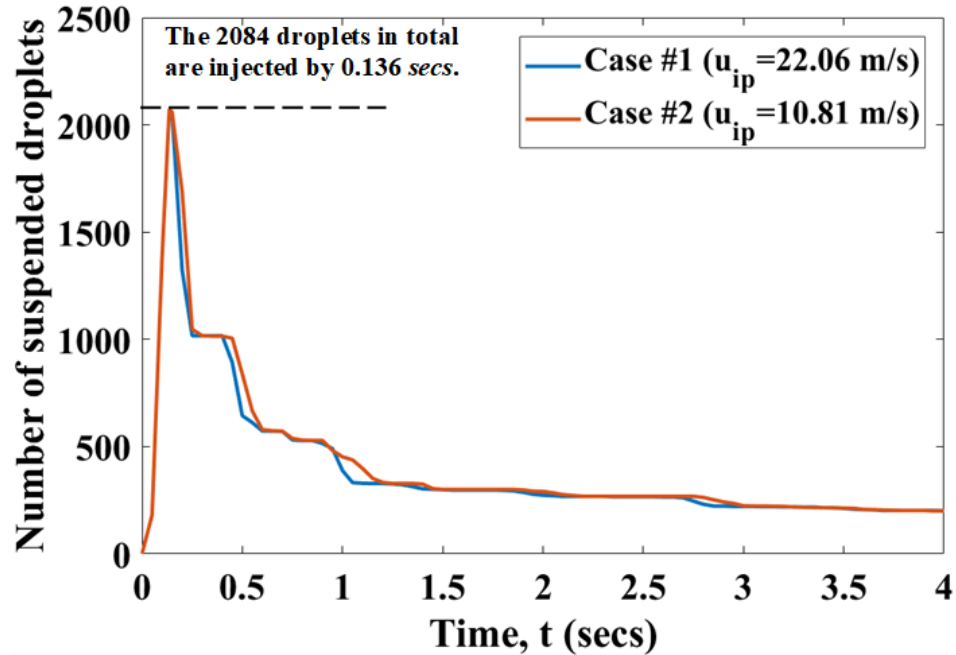


Figure 3.15: Comparison of time history of total number of droplets suspended under different inlet cough velocities.

Figure 3.16 presents the time history of the overall mean diameter of the droplets ($\langle d_p \rangle$) under two different inlet cough velocities. The difference in the variation of $\langle d_p \rangle$ with time between the two cases is very small, except for the peak values, which indicates that the inlet cough velocity does not significantly affect the evaporation of droplets. However, since Case #2 has a lower inlet cough velocity, compared to Case #1, the droplets disperse with a lower velocity in the near-field region, which results in a lower coalescence rate of the droplets. So, the peak value of $\langle d_p \rangle$, which is at 0.5 secs, for Case #2 is lower than that for Case #1.

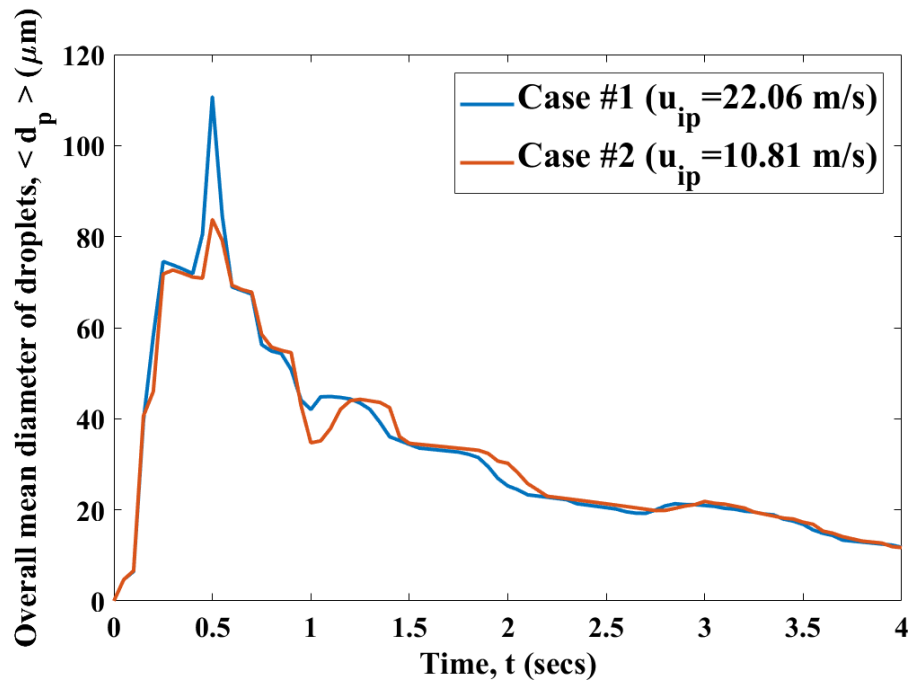


Figure 3.16: Comparison of time history of overall mean diameter of droplets under different inlet cough velocities.

3.4 Conclusions

A numerical study has been carried out to examine the dispersion and evaporation processes of the droplets produced by coughing. The Lagrangian discrete phase model is used to track a total 2084 droplets with the diameter range of 3-750 μm . The effects of the RH of the ambient environment and the inlet time-dependent cough velocity on the droplet dispersion and evaporation are investigated by conducting three simulations under different ambient RH and inlet cough velocities.

The droplet dispersion is investigated based on the contours of the droplet diameters and the penetration distance. It is found that the larger droplets precipitate on the ground as time progresses, which could cause the droplet transmission of the respiratory pathogen, and the precipitating speed depends on the droplet size. Whereas the smaller droplets with the diameter $d_p \leq 10 \mu\text{m}$ remain suspended in the ambient air, which could result in the airborne transmission of the respiratory pathogen. The penetration distance of the droplets grows in a more gradual trend with time, whilst both a higher ambient RH and a lower inlet

cough velocity will weaken the droplet penetration and, therefore, could weaken the respiratory pathogen transmission during coughing in different degrees. Moreover, the inlet cough velocity has a much more significant influence on the droplet penetration, in compare to the ambient RH. The droplet evaporation is examined in terms of the droplet size distribution at different time as well as the variation of the overall mean droplet diameter with time. It is found that the evaporation occurs immediately after the droplets are injected, which results in a gradual decrease of the droplet diameter. A higher ambient RH would slow down the droplet evaporation, which is consistent with the findings of Aliabadi et al (2010) and Xie et al (2007). However, the difference in the change of the droplet diameter with time under different inlet cough velocities is small. So, the inlet cough velocity dose not significantly affect the droplet evaporation. Furthermore, the collision and coalescence of the droplets have a great influence on the droplet size distribution. It is found that the droplets would collide and coalesce together into larger droplets, which results in an increase in the overall mean droplet diameter initially, and then the larger droplets fall to the ground due to the gravity, which makes the number of suspended droplets decrease. Both a higher ambient RH and a lower inlet cough velocity give a lower coalescence rate for the droplets, and the inlet cough velocity shows a much less impact on the coalescence and precipitation of the suspended droplets, compared to the ambient RH.

For future work, additional simulations should be performed under different RH of the ambient air and inlet cough velocities to examine the effects of those conditions on the droplet dispersion and evaporation further. Other cough conditions, such as the cough duration and direction, are also important and need to be investigated. Moreover, the experimental data are required in order to validate the effectiveness of the Lagrangian discrete phase model in predicting the dynamic development of the droplets produced by coughing. The impacts of other drag laws, such as the dynamic drag model, on the modelling performance of the discrete phase model should be analyzed as well.

The next chapter will give an overall summary of the present study, including the work that has been done and the corresponding conclusions. The recommendations for future work

in terms of the modifications and improvements of the CFD modeling of human cough flow will also be provided.

References

- Aliabadi, A. A., Rogak, S. N., Green, S. I., & Bartlett, K. H. (2010). CFD simulation of human coughs and sneezes: a study in droplet dispersion, heat, and mass transfer. *Proceedings of the ASME 2010 International Mechanical Engineering Congress & Exposition (IMECE2010)*, 1051–1060.
- ANSYS, Inc. (2013). *ANSYS Fluent Theory Guide 15.0*.
- ANSYS, Inc. (2014). *ANSYS Fluent User's Guide 15.0*.
- Antonia, R. A., & Zhao, Q. (2001). Effect of initial conditions on a circular jet. *Experiments in Fluids*, 31(3), 319–323.
- Atkinson, J. J., Chartier, Y., Pessoa-Silva, C. L., Jensen, P., Li, Y., & Seto, W.-H. (2009). Natural ventilation for infection control in health-care settings. *WHO Publication/Guidelines*, 77.
- Austin, E., Brock, J., & Wissler, E. (1979). A model for deposition of stable and unstable aerosols in the human respiratory tract. *American Industrial Hygiene Association Journal*, 40(12), 1055–1066.
- Barker, D. J. P., Godfrey, K. M., Fall, C., Osmond, C., Winter, P. D., & Shaheen, S. O. (1991). Relation of birth weight and childhood respiratory infection to adult lung function and death from chronic obstructive airways disease. *BMJ*, 303(671), 675.
- Bean, B., Moore, B. M., Sterner, B., Peterson, L. R., Gerding, D. N., & Balfour, H. H. (1982). Survival of influenza viruses on environmental surfaces. *The Journal of Infectious Diseases*, 146(1), 47–51.
- Bisoi, M., Das, M. K., Roy, S., & Patel, D. K. (2017). Large eddy simulation of three-dimensional plane turbulent free jet flow. *European Journal of Mechanics, B/Fluids*, 65, 423–439.
- Bourouiba, L., Dehandschoewercker, E., & Bush, J. W. M. (2014). Violent expiratory events: on coughing and sneezing. *Journal of Fluid Mechanics*, 745, 537–563.

- Chao, C. Y. H., Wan, M. P., Morawska, L., Johnson, G. R., Ristovski, Z. D., Hargreaves, M., Mengersen, K., Corbett, S., Li, Y., Xie, X., & Katoshevski, D. (2009). Characterization of expiration air jets and droplet size distributions immediately at the mouth opening. *Journal of Aerosol Science*, *40*(2), 122–133.
- Couch, R. B., Cate, T. R., Douglas, R. G. J., Gerone, P. J., & Knight, V. (1966). Effect of route of inoculation on experimental respiratory disease in volunteers and evidence for airborne transmission. *Bacteriological Reviews*, *30*, 517–529.
- Duguid, J. P. (1946). The size and the duration of air-carriage of respiratory droplets and droplet-nuclei. *Journal of Hygiene*, *44*(6), 471–479.
- Fabian, P., McDevitt, J. J., DeHaan, W. H., Fung, R. O. P., Cowling, B. J., Chan, K. H., Leung, G. M., & Milton, D. K. (2008). Influenza virus in human exhaled breath: an observational study. *PLoS ONE*, *3*(7), e2691.
- Fairchild, C. I., & Stampfer, J. F. (1987). Particle concentration in exhaled breath. *American Industrial Hygiene Association Journal*, *48*(11), 948–949.
- Fennelly, K. P., Martyny, J. W., Fulton, K. T., Orme, I. M., Cave, D. M., & Heifets, L. B. (2004). Cough-generated Aerosols of Mycobacterium tuberculosis. *American Journal of Respiratory Critical Care Medicine*, *169*, 604–609.
- Garner, J. S. (1996). Guideline for isolation precautions in hospitals. *Infection Control and Hospital Epidemiology*, *17*(1), 53–80.
- Gralton, J., Tovey, E., McLaws, M. L., & Rawlinson, W. D. (2011). The role of particle size in aerosolised pathogen transmission: A review. *Journal of Infection*, *62*(1), 1–13.
- Gupta, J. K., Lin, C.-H., & Chen, Q. (2009). Flow dynamics and characterization of a cough. *Indoor Air*, *19*(6), 517–525.
- Hemmes, J. H., Winkler, K. C., & Kool, S. M. (1960). Virus survival as a seasonal factor in influenza and poliomyelitis. *Nature*, *188*, 430–431.

- Jennison, M. W. (1942). Atomizing of mouth and nose secretions into the air as revealed by high-speed photography. *Aerobiology*, *17*, 106–128.
- Kraichnan, R. (1970). Diffusion by a random velocity field. *Physics of Fluids*, *11*, 21–31.
- Lange, B., & Keschischian, K. H. (1925). Experimentelle untersuchungen über die bedeutung der tröpfcheninfektion bei der tuberkulose. *Zeitschrift für Hygiene und Infektionskrankheiten*, *104*, 256.
- Li, A. C. Y. (2006). *Theoretical Modeling and Experimental Studies of Particle-Laden Plumes from Wastewater Discharges*. M. Phil. Thesis, The University of Hong Kong.
- Li, S., Eisenberg, J. N. S., Spicknall, I. H., & Koopman, J. S. (2009). Dynamics and control of infections transmitted from person to person through the environment. *American Journal of Epidemiology*, *170*(2), 257–265.
- Lindsley, W. G., Pearce, T. A., Hudnall, J. B., Davis, K. A., Davis, S. M., Fisher, M. A., Khakoo, R., Palmer, J. E., Clark, K. E., Celik, I., Coffey, C. C., Blachere, F. M., & Beezhold, D. H. (2012). Quantity and size distribution of cough-generated aerosol particles produced by influenza patients during and after illness. *Journal of Occupational and Environmental Hygiene*, *9*(7), 443–449.
- MacFarlane, J., Colville, A., Guion, A., MacFarlane, R., & Rose, D. H. (1993). Prospective study of aeriology and outcome of adult lower-respiratory-tract infections in the community. *The Lancet*, *341*(8844), 511–514.
- Nijemeisland, M., & Dixon, A. G. (2004). CFD study of fluid flow and wall heat transfer in a fixed bed of spheres. *AIChE Journal*, *50*(5), 906–921.
- Ostrowsky, B. (2007). Epidemiology of healthcare-associated infections. In W. R. Jarvis (Ed.), *Bennett and Brachman's Hospital Infections* (5th ed, pp. 3–24). Philadelphia: Lippincott Williams & Wilkins.
- Ounis, H., Ahmadi, G., & McLaughlin, J. B. (1991). Brownian diffusion of submicrometer particles in the viscous sublayer. *Journal of Colloid and Interface Science*, *143*(1), 66–277.

- Papineni, R. S., & Rosenthal, F. S. (1997). The size distribution of droplets in the exhaled breath of healthy human subjects. *Journal of Aerosol Medicine*, *10*(2), 105–116.
- Patankar, S. V., Spalding, D. B., & Road, E. (1972). A calculation procedure for heat, mass and momentum transfer in three-dimensional parabolic flows. *International Journal of Heat and Mass Transfer*, *15*(10), 1787–1806.
- Saladin, K. S. (2003). *Anatomy & Physiology* (3rd ed.). New York: McGraw Hill.
- Smirnov, R., Shi, S., & Celik, I. (2001). Random flow generation technique for large eddy simulations and particle-dynamics modeling. *Journal of Fluids Engineering*, *123*, 359–371.
- Stelzer-Braid, S., Oliver, B. G., Blazey, A. J., Argent, E., Newsome, T. P., Rawlinson, W. D., & Tovey, E. R. (2009). Exhalation of respiratory viruses by breathing, coughing and talking. *Journal of Medical Virology*, *81*, 1674–1679.
- Strausz, W. (1926). *Zeitschrift für Hygiene und Infektionskrankheiten*, *105*, 416.
- Tang, J. W., Liebner, T. J., Craven, B. A., & Settles, G. S. (2009). A schlieren optical study of the human cough with and without wearing masks for aerosol infection control. *Journal of the Royal Society Interface*, *6*(2009), S727–S736.
- Tupasi, T. E., Velmonte, M. A., Sanvictores, M. E. G., Abraham, L., De Leno, D. E., Tan, S. A., Miguel, C. A., & Saniel, M. C. (1988). Determinants of morbidity and mortality due to acute respiratory infections: implications for interventions. *Journal of Infectious Diseases*, *157*(4), 615–623.
- Verreault, D., Moineau, S., & Duchaine, C. (2008). Methods for sampling of airborne viruses. *Microbiology and Molecular Biology Reviews*, *72*(3), 413–444.
- Wainwright, C. E., France, M. W., O'Rourke, P., Anuj, S., Kidd, T. J., Nissen, M. D., Sloots, T. P., Coulter, C., Ristovski, Z., Hargreaves, M., Rose, B. R., Harbour, C., Bell, S. C., & Fennelly, K. P. (2009). Cough-generated aerosols of *Pseudomonas aeruginosa* and other Gram-negative bacteria from patients with cystic fibrosis. *Thorax*, *64*, 926–931.

- Wakeman, T., & Tabakoff, W. (1982). Measured particle rebound characteristics useful for erosion prediction. *The American Society of Mechanical Engineers, 82-GT-170*, 1-12.
- Weber, T. P., & Stilianakis, N. I. (2008). Inactivation of influenza A viruses in the environment and modes of transmission: a critical review. *Journal of Infection, 57*, 361–373.
- Wei, J., & Li, Y. (2017). Human cough as a two-stage jet and its role in particle transport. *PLoS ONE, 12*(1), 1–15.
- Wells, W. F. (1934). On air-born infection. Study II. Droplet and droplet nuclei. *American Journal of Hygiene, 20*, 611–618.
- Wells, W. F. (1955). *Airborne Contagion and Air Hygiene: An Ecological Study of Droplet Infection*. Harvard University Press.
- Xie, X., Li, Y., Chwang, A. T. Y., Ho, P. L., & Seto, W. H. (2007). How far droplets can move in indoor environments - revisiting the Wells evaporation-falling curve. *Indoor Air, 17*(3), 211–225.
- Yang, S., Lee, G. W. M., Chen, C.-M., Wu, C.-C., & Yu, K.-P. (2007). The size and concentration of droplets generated by coughing in human subjects. *Journal of Aerosol Medicine, 20*(4), 484–494.
- Yu, C. P., & Taulbee, D. B. (1975). A theory of predicting respiratory tract deposition of inhaled particles in man. *Inhaled Particles, 4*(1), 35–47.
- Zhang, L., & Li, Y. (2012). Dispersion of coughed droplets in a fully-occupied high-speed rail cabin. *Building and Environment, 47*(1), 58–66.
- Zhu, S., Kato, S., & Yang, J.-H. (2006). Study on transport characteristics of saliva droplets produced by coughing in a calm indoor environment. *Building and Environment, 41*(12), 1691–1702.

Chapter 4

4 Conclusions and Recommendations

4.1 Conclusions

As part of the Western Cold and Flu aerosol (WeCoF) studies, the present study provides Computational Fluid Dynamics (CFD) modelling of human cough flow. The cough flow is characterized in two different aspects, the flow field and the droplets. In the study of the flow field of coughing, various dynamic characteristics, including the velocity variation, streamwise penetration and power spectral density, are numerically examined. CFD simulations using two different approaches, the unsteady Reynolds Averaged Navier-Stokes (URANS) and the large eddy simulation (LES), are performed for comparison purposes. The numerical results are validated by the experimental data obtained from measurements by particle image velocimetry (PIV) and hot-wire anemometry (HWA), as well as the published data. In the study of the droplets produced by coughing, the dynamic characteristics, including the dispersion and evaporation processes, are investigated. The Lagrangian discrete phase model is employed to track a total 2084 droplets in the diameter range 3-750 μm . The effects of different inlet and ambient conditions, including the relative humidity (RH) of the ambient air and the inlet time-dependent cough velocity, on the droplet dispersion and evaporation are analyzed.

In the study of the flow field of coughing, the contours of velocity magnitude at different time are analyzed. Compared to the URANS modelling, which gives a velocity distribution in a symmetric and regular way, the LES modelling shows an irregular and non-uniform velocity distribution, which gives a good agreement with the PIV measurement and, hence, provides a more realistic and accurate prediction of the velocity magnitude variation with time of the flow field of coughing. The numerical results are also compared with the PIV measurements in terms of the spatially averaged velocity on the PIV field of view and the 2-dimensional velocity magnitude at the midpoint of each cough flow. It is found that the LES modelling and the PIV measurements have a similar variation of the velocity with time and the peak values are close, while the URANS modelling shows a smooth variation trend without any fluctuation. In the comparison with the HWA measurements, the LES

modelling gives a good agreement for the normalized u component velocity at the location of the hot-wire probe, while the URANS modelling still shows a smooth trend due to the ensemble-averaged flow field of motion it solves for. In the investigation of the streamwise penetration, the LES modelling is compared with the published experimental data, and shows a very good agreement for the normalized streamwise penetration distance in both the starting-jet and interrupted-jet stages. The maximum jet width in the interrupted-jet stage grows with time in a roughly linear trend, and the corresponding axial distance increases with time in a roughly second-order polynomial manner. In the analysis of the power spectral density, all the energy spectra obtained from the LES modelling and HWA measurements have a universal decay with the slope of $-5/3$, which indicates that the energy transfer process in the inertial subrange follows the Kolmogorov hypothesis. In summary, based on the comparison with the URANS approach and the experimental data, the LES approach can predict the dynamic development of the flow field of coughing reasonably well.

In the study of the droplets produced by coughing, the contours of the droplet diameters and the penetration distance are analyzed for the investigation of the droplet dispersion. It is found that as time progresses, the larger droplets fall to the ground, which could cause the droplet transmission of the respiratory pathogen, and the falling speed depends on the droplet size. While the smaller droplets with the diameter $d_p \leq 10 \mu\text{m}$ remain suspended for a longer period, which could result in the airborne transmission of the respiratory pathogen. Both the mean and maximum penetration distances from the mouth of the droplets grow in a more gradual trend with time, and will be weakened by both a higher RH of the ambient air and a lower inlet cough velocity, which implies that a higher ambient RH and a lower inlet cough velocity will weaken the respiratory pathogen transmission. In the analysis of the droplet evaporation, the droplet size distribution at different time and the variation of the overall mean droplet diameter with time are examined. It is found that the evaporation causes a gradual decrease in the droplet diameter, and is significantly affected by the ambient RH, i.e. the higher the RH, the slower the evaporation. However, the inlet cough velocity does not show a strong influence on the evaporation of the droplets. Moreover, the droplet collision and coalescence also affect the droplet size distribution,

and both a higher ambient RH and a lower inlet cough velocity give a lower coalescence rate of the droplets.

4.2 Recommendations

The present study numerically investigates the dynamic characteristics of human cough flow in terms of the flow field and the droplets by the CFD modelling, and some aspects are recommended for future work, as listed below:

- The effects of different conditions, including the RH of the ambient air, the inlet time-dependent cough velocity, etc., on the dynamic characteristics of the flow field of coughing, should be investigated.
- The recruitment of more participants is necessary for a statistically significant cohort of the experimental data, which will contribute to the validation of the numerical results.
- Additional simulations should be performed under different RH of the ambient air and inlet cough velocities to examine the effects on the dispersion and evaporation of the droplets produced by coughing further.
- In order to examine the validity of the Lagrangian discrete phase model, which is employed to track the droplets produced by coughing, related experiment data are required.

Appendices

Appendix A: Computational Fluid Dynamic (CFD) Modelling of a Steady Round Free Jet Flow

A Computational Fluid Dynamics (CFD) study is carried out to numerically investigate the performance of various turbulence models under the Reynolds Averaged Navier-Stokes (RANS) approach in predicting a steady-state, turbulent, round free jet. The commercial CFD package, ANSYS FLUENT 16.0, is used for the numerical simulation. The experimental data obtained from the work of Xu and Antonia (2002) are used to validate the numerical results. The most appropriate turbulence model is employed for the unsteady RANS (URANS) modelling of the flow field of coughing, which is introduced in detail in Chapter 2.

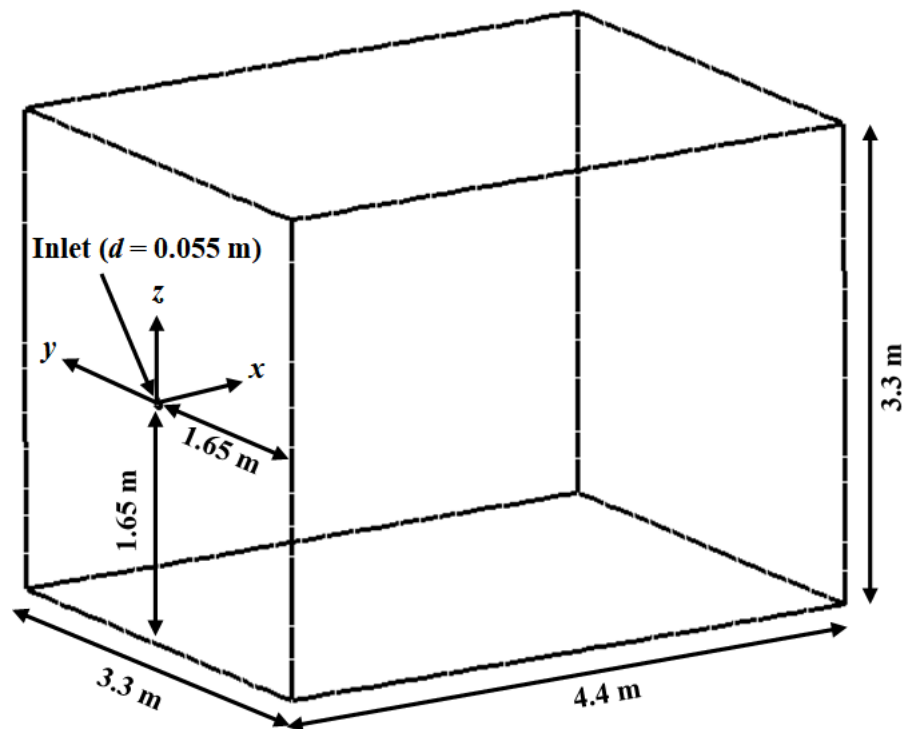


Figure A-1: Schematic of the computational domain along with its dimensions.

The turbulent round free jet studied in the experimental work is axisymmetric, isothermal, and has the exit bulk Reynolds number $Re = 86000$. A computational domain in the

dimensions of 4.4 m in length, 3.3 m in width and 3.3 m in height, is developed to remain consistent with the experimental work, as shown in Figure A-1, where the “ x ”, “ y ” and “ z ” axes represent the axial (streamwise), lateral and vertical directions, respectively. The inlet is a circular orifice of diameter $d = 0.055$ m with the centre denoted by $(0, 0, 0)$, which is also the origin of the coordinate system. The computation domain and grid are generated by using the commercial CFD package, ICEM CFD 16.0. An irregular unstructured tetrahedral grid is created in non-uniform sizes to characterize the dynamic development of the jet flow more effectively. The grid sizes in the inlet, cone and global regions are 0.8, 8 and 67 mm, respectively, as shown in Figure A-2. The number of the computational cells is approximately 19.3 million in total.

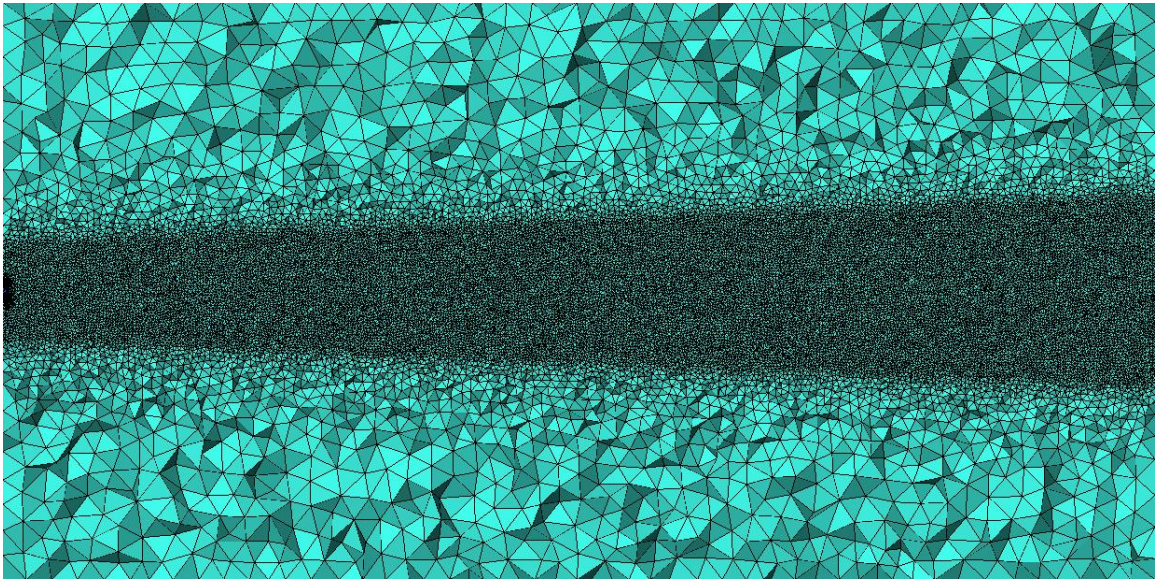


Figure A-2: Grid distribution on the x - z plane ($y=0$) of the computational domain.

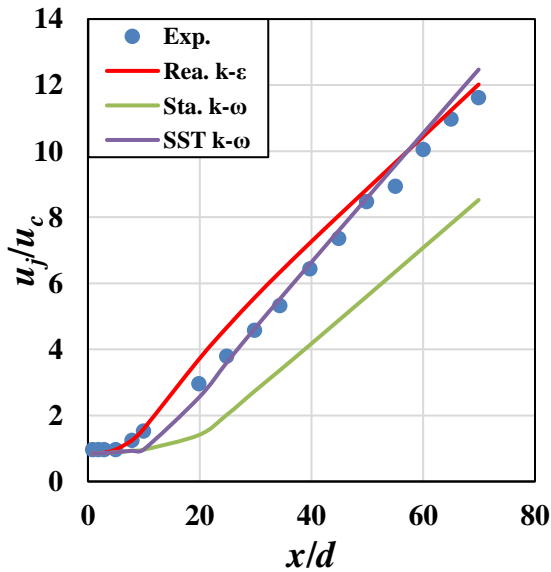
Three different two-differential-equation turbulence models, including the realizable k - ϵ , standard k - ω and shear stress transport (SST) k - ω models, are examined in the present study. A pressure-based solver with double precision is selected to gain a higher accuracy of the residual convergence. The coupled algorithm is employed as the pressure-velocity coupling method. For the pressure interpolation, the second-order scheme is used, and for the gradient evaluation, the Green-Gauss node-based scheme is performed. The second-order upwind discretization scheme is employed to solve the momentum, turbulent kinetic energy and turbulent dissipation rate. In order to prevent the residual convergence from

stalling under the second-order spatial discretization being used, the high order term relaxation is enabled.

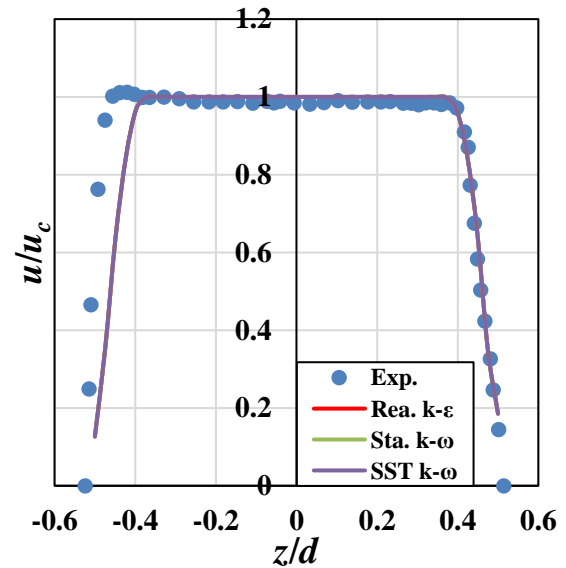
The boundary condition of the inlet is defined to be a velocity-inlet, and the velocity direction is set as normal to boundary, which satisfies that the airflow is issued into the computational domain with the velocity in the streamwise direction. The velocity imposed at the inlet is a function of the vertical distance from the origin (see Appendix L) with an area-averaged value of 23.3 m/s (i.e. exit bulk velocity u_j), which is defined to keep consistent with the top-hat velocity profile used in the experimental work. Other boundaries are set as pressure-outlet, in order to eliminate the effect on the dynamic development of the free jet flow. The turbulence intensity at the inlet is defined to be 0.5% of the exit bulk velocity u_j , and the hydraulic diameter is set as 0.055 m, equal to the inlet diameter. The surrounding fluid velocity is set as zero to satisfy the quiescent ambient environment. The airflow issued from the inlet is defined to be incompressible air with the density and viscosity of 1.225 kg/m^3 and $1.7894 \times 10^{-5} \text{ kg/m-s}$, respectively.

In the comparison with the experimental data, the spatial variation of different quantities is examined in a normalized way, including the centreline velocity (u_c), the velocity (u) at different downstream cross-sections, as well as the half-width (r_u), as shown in Figure A-3. It is deducible from Figure A-3 (a) that the centreline velocity u_c decays with an increase in streamwise distance (x), and the SST $k-\omega$ model gives the best agreement to the experimental data. Figure A-3 (b) shows the velocity profiles imposed at the inlet for both the experimental and numerical works, and it is clear that all the profiles are in a top-hat shape. Figure A-3 (c) and (d) exhibit the velocity u varying with the vertical distance (z) from the centreline at two different downstream cross-sections. It is found that the velocity profile across the free jet flow shows a nearly Gaussian shape, which infers that the change of the velocity u obeys a self-similarity. This is because when a jet enters a stagnant fluid, the absence of the external forces makes the sole momentum source be the jet flow itself, and the momentum flux in the cross-sections keeps constant downstream. It is also clear that all the turbulence models show similar profiles of u , and the SST $k-\omega$ model gives the best prediction. Figure A-3 (e) shows the streamwise variation of the half-width r_u , which is defined as the distance between the centreline and a radial plane where the mean flow

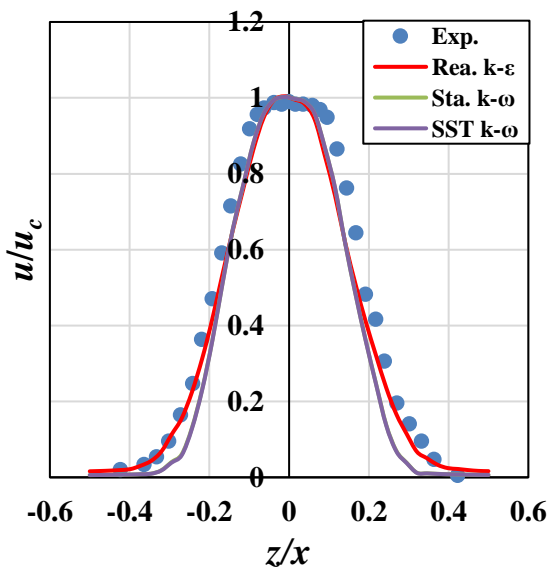
velocity u is half the corresponding centreline velocity u_c . The half-width r_u describes an approximate radial location of the shear layer, which is generated between the jet flow and the ambient fluid, and has the maximum shear stress. It is found from Figure A-3 (e) that r_u increases linearly with a slope, also known as the spreading rate, in the streamwise direction, and the SST $k-\omega$ model gives the best agreement to the experimental data.



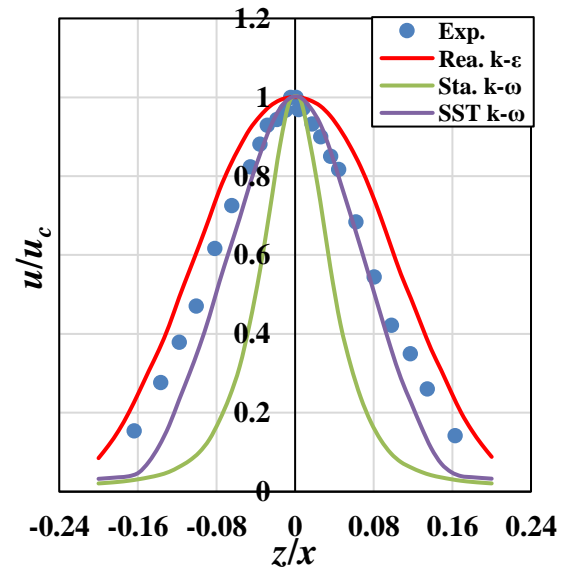
(a)



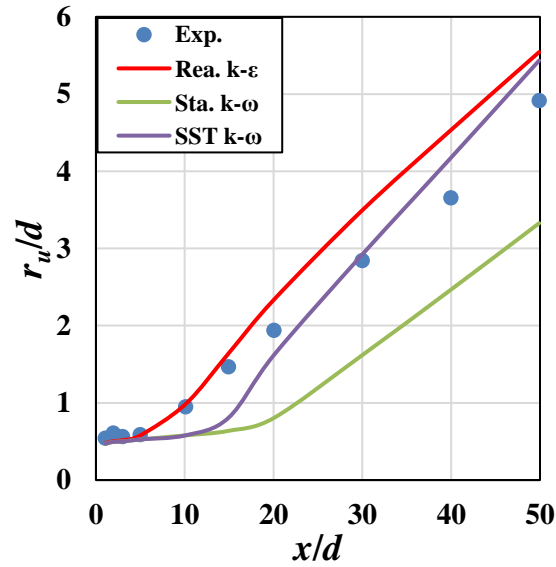
(b)



(c)



(d)



(e)

Figure A-3: Comparison of the spatial variation of (a) u_j/u_c along the streamwise direction, (b) u/u_c along the vertical direction at $x = 0$, (c) u/u_c along the vertical direction at $x = 3d$, (d) u/u_c along the vertical direction at $x = 20d$, and (e) r_u/d along the streamwise direction with the experimental data.

In conclusion, among all the RANS turbulence models selected in the present study, the SST $k-\omega$ model gives the best prediction performance of a steady-state, turbulent, round free jet and, hence, is adopted for the URANS modelling of the flow field of coughing in Chapter 2.

Reference

Xu, G., & Antonia, R. A. (2002). Effect of different initial conditions on a turbulent round free jet. *Experiments in Fluids*, 33(5), 677–683.

Appendix B: Details about the Governing Equations of the SST Turbulence $k-\omega$ Model

The form of the SST $k-\omega$ turbulence model is similar to that of standard $k-\omega$ model, but improves in the following terms:

- (1) A blending function is used in order to combine the standard $k-\omega$ and transformed $k-\varepsilon$ models. It equals 1 in the near-wall region to multiply by the standard $k-\omega$ model, and equals 0 in the far-field region to multiply by the transformed $k-\varepsilon$ model.
- (2) A damped cross-diffusion derivative term is involved in the specific dissipation rate (ω) equation.
- (3) It modifies the formulation of turbulent viscosity to determine the transport of shear stress.

The details about the governing equations of the SST $k-\omega$ model are shown as below.

In Eqn. (2.9), the coefficient α is calculated from

$$\alpha = \frac{\alpha_\infty}{\alpha^*} \left(\frac{\alpha_0 + Re_t / R_\omega}{1 + Re_t / R_\omega} \right), \quad \alpha_\infty = F_1 \alpha_{\infty,1} + (1 - F_1) \alpha_{\infty,2} \quad (\text{A-1})$$

where R_ω is equal to 2.95, and α^* is defined as a low-Reynolds number correction. α^* and Re_t are expressed as

$$\alpha^* = \alpha_\infty^* \left(\frac{\alpha_0^* + Re_t / R_k}{1 + Re_t / R_k} \right), \quad Re_t = \frac{\rho k}{\mu \omega}, \quad R_k = 6, \quad \alpha_0^* = \frac{\beta_i}{3}, \quad \beta_i = 0.072 \quad (\text{A-2})$$

In Eqn. (A-1), $\alpha_{\infty,1}$ and $\alpha_{\infty,2}$ are defined as

$$\alpha_{\infty,1} = \frac{\beta_{i,1}}{\beta_\infty^*} - \frac{\kappa^2}{\sigma_{w,1} \sqrt{\beta_\infty^*}}, \quad \alpha_{\infty,2} = \frac{\beta_{i,2}}{\beta_\infty^*} - \frac{\kappa^2}{\sigma_{w,2} \sqrt{\beta_\infty^*}} \quad (\text{A-3})$$

where κ is equal to 0.41. It is noteworthy that $\alpha = \alpha_\infty = 1$ for a high-Reynolds number flow, i.e. a fully-developed turbulent flow, which is normally defined as $Re \gtrsim 1-2 \times 10^4$ for a free jet flow (Dimotakis, 2000).

In Eqns. (2.10) and (2.11), the turbulent viscosity μ_t is expressed as

$$\mu_t = \frac{\rho k}{\omega} \frac{1}{\max[\frac{1}{\alpha^*}, \frac{SF_2}{a_1 \omega}]} \quad (\text{A-4})$$

where α^* is calculated from Eqn. (A-2), and S is the magnitude of the strain rate, defined as

$$S \equiv \sqrt{2S_{ij}S_{ij}}, S_{ij} = \frac{1}{2} \left(\frac{\partial \bar{u}_j}{\partial x_i} + \frac{\partial \bar{u}_i}{\partial x_j} \right) \quad (\text{A-5})$$

In Eqns. (2.10) and (2.11), σ_k and σ_ω represent the turbulent Prandtl numbers for k and ω , respectively, and are calculated from

$$\sigma_k = \frac{1}{F_1/\sigma_{k,1} + (1-F_1)/\sigma_{k,2}}, \sigma_\omega = \frac{1}{F_1/\sigma_{\omega,1} + (1-F_1)/\sigma_{\omega,2}} \quad (\text{A-6})$$

In Eqns. (A-1), (A-4) and (A-6), F_1 and F_2 are the blending functions, expressed as

$$F_1 = \tanh(\Phi_1^4), \Phi_1 = \min\left[\max\left(\frac{\sqrt{k}}{0.09\omega y}, \frac{500\mu}{\rho y^2 \omega}\right), \frac{4\rho k}{\sigma_{\omega,2} D_\omega^+ y^2}\right] \quad (\text{A-7})$$

$$F_2 = \tanh(\Phi_2^2), \Phi_2 = \max\left[2 \frac{\sqrt{k}}{0.09\omega y}, \frac{500\mu}{\rho y^2 \omega}\right] \quad (\text{A-8})$$

where y represents the distance from the closest no-slip wall (Jubayer, 2010), and D_ω^+ is defined as the positive part of the damped cross-diffusion derivative term (D_ω), given as

$$D_\omega^+ = \max\left[2\rho \frac{1}{\sigma_{\omega,2}} \frac{1}{\omega} \frac{\partial k}{\partial x_j} \frac{\partial \omega}{\partial x_j}, 10^{-10}\right] \quad (\text{A-9})$$

In Eqns. (2.12) and (2.13),

$$f_{\beta^*} = 1, \beta^* = \beta_i^* [1 + \zeta^* F(M_t)], \beta_i^* = \beta_\infty^* \left(\frac{4/15 + (Re_t/R_\beta)^4}{1 + (Re_t/R_\beta)^4} \right), \zeta^* = 1.5, R_\beta = 8, \beta_\infty^* = 0.09 \quad (\text{A-10})$$

$$f_\beta = 1, \beta = \beta_i [1 - \frac{\beta_i^*}{\beta_i} \zeta^* F(M_t)], \beta_i = F_1 \beta_{i,1} + (1 - F_1) \beta_{i,2} \quad (\text{A-11})$$

where Re_t and F_1 are calculated from Eqns. (A-2) and (A-7), respectively, and $F(M_t)$ represents the compressibility function, given as

$$F(M_t) = \begin{cases} 0 & M_t \leq M_{t0} \\ M_t^2 - M_{t0}^2 & M_t > M_{t0} \end{cases}, M_t^2 \equiv \frac{2k}{a^2}, M_{t0} = 0.25, a = \sqrt{\gamma RT} \quad (\text{A-12})$$

It is noteworthy that $\beta_i^* = \beta_\infty^*$ for a high-Reynolds number flow, and $\beta^* = \beta_i^*$ for an incompressible flow.

In order to combine the standard $k-\omega$ and $k-\varepsilon$ models, the SST $k-\omega$ model converts the standard $k-\varepsilon$ model into the formulations based on k and ω . To achieve the conversion process, a damped cross-diffusion derivative term, D_ω , is introduced and expressed as Eqn. (2.14).

The model constants are listed as follows (Menter, 1994):

$$\sigma_{k,1} = 1.176, \sigma_{\omega,1} = 2.0, \sigma_{k,2} = 1.0, \sigma_{\omega,2} = 1.168, a_1 = 0.31, \beta_{i,1} = 0.075, \beta_{i,2} = 0.0828, \alpha_\infty^* = 1, \alpha_0 = \frac{1}{9}, \beta_\infty^* = 0.09, R_\beta = 8, R_k = 6, R_\omega = 2.95, \zeta^* = 1.5, M_{t0} = 0.25$$

The evaluation of different turbulence models in predicting a steady-state, turbulent, round free jet is given in Appendix A, from which the SST $k-\omega$ turbulence model gives the best prediction.

Reference

- Dimotakis, P. E. (2000). The mixing transition in turbulent flows. *Journal of Fluid Mechanics*, 409, 69-98.
- Jubayer, C. M. (2010). *Numerical Modelling of Forced Convective Heat Transfer from the Inclined Windward Roof of a Low-Rise Building with Application to Photovoltaic/Thermal Systems*. M. E. Sc. Thesis, Department of Mechanical and Materials Engineering, The University of Western Ontario.
- Menter, F. R. (1994). Two-equation eddy-viscosity turbulence models for engineering applications. *AIAA Journal*, 32(8), 1598–1605.

Appendix C: The Dynamic Smagorinsky-Lilly Model

The dynamic Smagorinsky-Lilly model is conceived based on the Smagorinsky-Lilly model, in which the SGS stress tensor, defined in Eqns. (2.17) and (3.3), is parameterized by an eddy-viscosity model using the Boussinesq hypothesis (Hinze, 1975), and is given as

$$\tau_{ij} - \frac{\delta_{ij}}{3}\tau_{kk} = -2\nu_t\tilde{S}_{ij} \quad (\text{A-13})$$

The SGS eddy-viscosity, ν_t , is computed from

$$\nu_t = L_S^2|\tilde{S}| \quad (\text{A-14})$$

where L_S represents the mixing length for subgrid scales, and is given as

$$L_S = \min(\kappa d_w, C_S\Delta) \quad (\text{A-15})$$

where κ and d_w are the von Kármán constant and distance to the nearest wall, respectively, and Δ represents the local grid scale, defined empirically as the cube root of the volume, V , of one computational grid cell:

$$\Delta = \sqrt[3]{V} \quad (\text{A-16})$$

In Eqn. (A-13), τ_{kk} represents the isotropic part of the SGS stress tensor, which is not modelled but added to the term of filtered static pressure (ANSYS, 2013). In Eqn. (A-14), $|\tilde{S}|$ is calculated from

$$|\tilde{S}| \equiv \sqrt{2\tilde{S}_{ij}\tilde{S}_{ij}} \quad (\text{A-17})$$

where \tilde{S}_{ij} represents the strain rate tensor of resolved turbulence scales, and is expressed as

$$\tilde{S}_{ij} \equiv \frac{1}{2}\left(\frac{\partial\tilde{u}_i}{\partial x_j} + \frac{\partial\tilde{u}_j}{\partial x_i}\right) \quad (\text{A-18})$$

In the dynamic Smagorinsky-Lilly model, a test filter is applied on the governing equations of motion, i.e. Eqns. (2.15), (2.16), (3.1) and (3.2), by introducing a new filter scale, $\hat{\Delta}$,

which equals twice the local grid scale Δ . Then a new SGS stress tensor, called the subtest-scale stress tensor (Bisoi et al., 2017), is generated as

$$T_{ij} = \widehat{u}_i \widehat{u}_j - \widehat{u}_i \widehat{u}_j \quad (\text{A-19})$$

and can also be parameterized into the form of the Boussinesq hypothesis,

$$T_{ij} - \frac{\delta_{ij}}{3} T_{kk} = -2C \widehat{\Delta}^2 \left| \widehat{S} \right| \widehat{S}_{ij} \quad (\text{A-20})$$

where the coefficient C is defined as $C = C_S^2$, and the test-filtered strain rate tensor of resolved large scales, \widehat{S}_{ij} , is computed from

$$\widehat{S}_{ij} \equiv \frac{1}{2} \left(\frac{\partial \widehat{u}_i}{\partial x_j} + \frac{\partial \widehat{u}_j}{\partial x_i} \right) \quad (\text{A-21})$$

The relation between the test-filtered SGS (employed in the dynamic Smagorinsky-Lilly model) and grid-filtered SGS (employed in the Smagorinsky-Lilly model) is presented by Germano et al. (1991), as shown in the following equation

$$L_{ij} = T_{ij} - \widehat{\tau}_{ij} = \widehat{u}_i \widehat{u}_j - \widehat{u}_i \widehat{u}_j \quad (\text{A-22})$$

where L_{ij} is computable for the resolved turbulence scales, and $\widehat{\tau}_{ij}$ is introduced as the average SGS stress tensor. Based on the work of Lilly (1992), the coefficient C can be derived from the following equation,

$$C = \frac{(L_{ij} - L_{kk} \delta_{ij} / 3)}{M_{ij} M_{ij}} \quad (\text{A-23})$$

where M_{ij} is expressed as

$$M_{ij} = -2(\widehat{\Delta}^2 \left| \widehat{S} \right| \widehat{S}_{ij} - \Delta^2 \left| \widetilde{S} \right| \widetilde{S}_{ij}) \quad (\text{A-24})$$

In Eqn. (A-23), both the denominator and numerator are filtered locally by applying the test filter in order to avoid the numerical instability.

Reference

- ANSYS, Inc. (2013). *ANSYS Fluent Theory Guide 15.0*.
- Bisoi, M., Das, M. K., Roy, S., & Patel, D. K. (2017). Large eddy simulation of three-dimensional plane turbulent free jet flow. *European Journal of Mechanics, B/Fluids*, 65, 423–439.
- Germano, M., Piomelli, U., Moin, P., & Cabot, W. H. (1991). A dynamic subgrid-scale eddy viscosity model. *Physics of Fluids A: Fluid Dynamics*, 3(7), 1760–1765.
- Hinze, J. O. (1975). *Turbulence*. New York: McGraw-Hill Publishing Co.
- Lilly, D. K. (1992). A proposed modification of the Germano subgrid-scale closure method. *Physics of Fluids A: Fluid Dynamics*, 4(3), 633–635.

Appendix D: Details about the Energy Equation

Since the flow field of coughing is considered to be incompressible, the sensible enthalpy h of the injected fluid, i.e. the mixture of the air and water vapour, is expressed as

$$h = \sum_j Y_j \int_{T_{ref}}^T c_{p,j} dT \quad (\text{A-25})$$

where Y_j and $c_{p,j}$ represent the mass fraction and specific heat capacity of species j . The value of the reference temperature, T_{ref} , used in Eqns. (2.18), (3.4) and (A-25) is set as 288.16 K.

On the right-hand side of Eqns. (2.18) and (3.4), the first and second terms represent the energy transfer caused by the conduction and species diffusion, respectively, and the viscous dissipation of heat is neglected. The effective conductivity, k_{eff} , is defined as

$$k_{eff} = k_m + k_t \quad (\text{A-26})$$

where k_m and k_t are the molecular and turbulent thermal conductivity of the flow field, respectively. The turbulent thermal conductivity k_t is calculated from (Jubayer, 2010)

$$k_t = \frac{c_p \mu_t}{Pr_t} \quad (\text{A-27})$$

where c_p and μ_t are the specific heat capacity and turbulent viscosity of the flow field, respectively. Pr_t represents the wall Prandtl number, and is set as 0.85. The calculation of the turbulent viscosity μ_t is obtained based on the turbulence model being performed in the CFD simulation, for example, for the URANS approach using the SST $k-\omega$ model, it is computed from Eqn. (A-4), while for the LES method using the dynamic Smagorinsky-Lilly model, it is derived from Eqn. (A-14) and is shown as follows,

$$\mu_t = \bar{\rho} \nu_t = \bar{\rho} C \hat{\Delta}^2 \left| \hat{S} \right| \quad (\text{A-28})$$

In Eqns. (2.18) and (3.4), \vec{J}_j represents the mass diffusion of species j , which results from the gradient of temperature and concentration (ANSYS, 2013), and is given as

$$\vec{J}_j = -\left(\rho D_{j,m} + \frac{\mu_t}{Sc_t}\right) \frac{\partial Y_j}{\partial x_j} - \frac{D_{T,j}}{T} \frac{\partial T}{\partial x_j} \quad (\text{A-29})$$

where $D_{j,m}$ and $D_{T,j}$ are the coefficients of mass diffusion of species j in the mixture and thermal diffusion, respectively, and Sc_t represents the turbulent Schmidt number expressed as $Sc_t = \frac{\mu_t}{\rho D_t}$ where D_t is the turbulent diffusivity.

Reference

ANSYS, Inc. (2013). *ANSYS Fluent Theory Guide 15.0*.

Jubayer, C. M. (2010). *Numerical Modelling of Forced Convective Heat Transfer from the Inclined Windward Roof of a Low-Rise Building with Application to Photovoltaic/Thermal Systems*. M. E. Sc. Thesis, Department of Mechanical and Materials Engineering, The University of Western Ontario.

Appendix E: The FLUGIE Cough Chamber

Figure A-4 shows the diagrammatic description and photograph of the FLUGIE chamber. It is located in Thompson Engineering Building (TEB) Room 308, at Western University. The chamber has the internal dimensions of 1.81 m in length, 1.78 m in width and 1.81 m in height, as shown in Figure A-4 (a), and creates a sufficiently large space to satisfy that the flow field of coughing spreads as a free jet flow without any influence of the solid boundaries. On the front wall, there is a small opening used for the participant to cough and it is placed 72 cm above the chamber floor. It is in a pear-shape so that the participant's nose and mouth are unobstructed. A head-rest fixes the participant's forehead in place to ensure the cough enters horizontally for each trial.

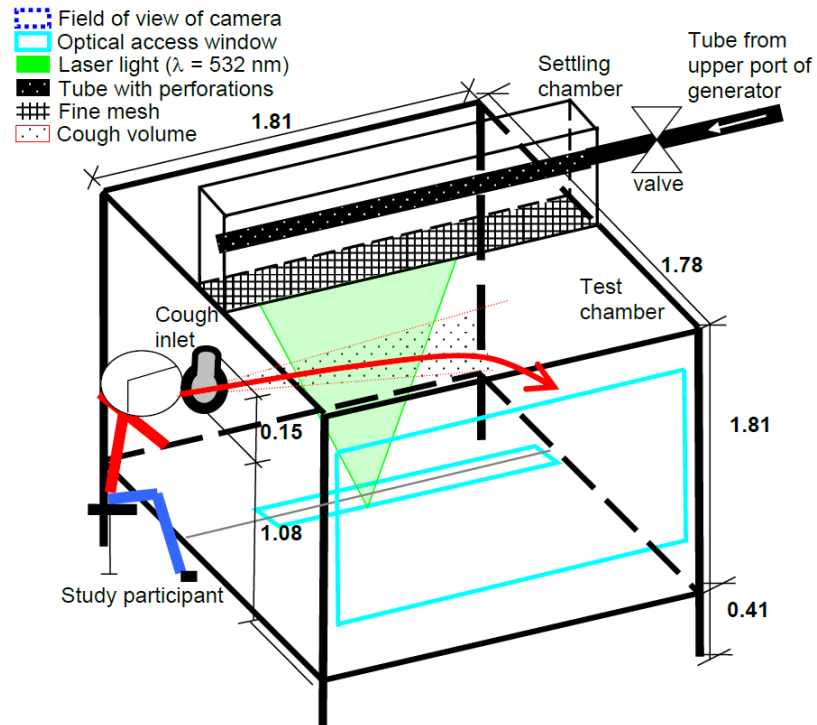


Figure A-4 (a): Schematic layout of the FLUGIE chamber (Mohamed, 2017 (with author's permission)). All dimensions are shown in the unit of metres.



Figure A-4 (b): The FLUGIE chamber located in Western University.

Reference

Mohamed, A. F. A. (2017). *Experimental Measurements of Far Field Cough Airflows Produced by Healthy and Influenza-Infected Human Subjects*. M. E. Sc. Thesis, Department of Mechanical and Materials Engineering, The University of Western Ontario.

Appendix F: Properties of the Injected Fluid

The correlations to determine the properties of the mixture of the air and water vapour used in the simulation are listed in Table A-1 (ANSYS, 2013).

Table A-1: Properties of the injected fluid.

Property	Computational method	Governing equation	Equation number
Density, ρ (kg/m ³)	Incompressible ideal gas law	$\rho = \frac{p_{op}}{RT \sum_i \frac{Y_i}{M_{w,i}}}$	(A-30)
Specific heat capacity, c_p (J/kg-K)	Mixing law	$c_p = \sum_i Y_i c_{p,i}$	(A-31)
Thermal conductivity, k (W/m-K)	Ideal gas mixing law	$k = \sum_i \frac{X_i k_i}{\sum_j X_j \phi_{ij}}$	(A-32)
Dynamic viscosity, μ (kg/m-s)	Ideal gas mixing law	$\mu = \sum_i \frac{X_i \mu_i}{\sum_j X_j \phi_{ij}}$	(A-33)

In Table A-1, the density ρ depends on the operating pressure, which is defined as the standard atmospheric pressure, i.e. 101,325 Pa, and the temperature T . In Eqn. (A-30), R is the universal gas constant with the value of 8.3145 J/mol-K. ϕ_{ij} in Eqns. (A-32) and (A-33) is given as

$$\phi_{ij} = \frac{\left[1 + \left(\frac{\mu_i}{\mu_j} \right)^{1/2} \left(\frac{M_{w,j}}{M_{w,i}} \right)^{1/4} \right]^2}{\left[8 \left(1 + \frac{M_{w,i}}{M_{w,j}} \right) \right]^{1/2}} \quad (\text{A-34})$$

The properties of the two species, air and water vapour, are shown in Table A-2,

Table A-2: Properties of the two species of the injected fluid.

Property	$M_{w,i}$ (g/mol)	$c_{p,i}$ (J/kg-K)	X_i	k_i (W/m-K)	μ_i (kg/m-s)
Air	28.966	1006.43	0.938	0.0242	1.7894×10^{-5}
Water vapour	18.01534	Piecewise-polynomial	0.062	0.0261	1.34×10^{-5}

where,

$M_{w,i}$ = molecular weight of species i ;

$c_{p,i}$ = specific heat capacity of species i ;

X_i = mole fraction of species i ;

k_i = molecular thermal conductivity of species i ;

μ_i = dynamic viscosity of species i .

The mass fraction of species i (Y_i), is determined by the species conservation equation, as shown in the following form:

$$\frac{\partial}{\partial t}(\rho Y_i) + \frac{\partial}{\partial x_i}(\rho u_i Y_i) = -\frac{\partial \vec{J}_i}{\partial x_i} \quad (\text{A-35})$$

Reference

ANSYS, Inc. (2013). *ANSYS Fluent Theory Guide 15.0*.

Appendix G: Moving Average Methodology

The actual cough flow is an unsteady turbulent phenomenon, therefore, a moving average can be employed to describe the underlying trend of such a flow by lowering the impact of the random variation (Mohamed, 2017). In statistics, a moving average is a technique to analyze the data through creating an array of averages of different subsets of the whole data (Booth et al., 2006). The window size k , i.e. the number of data in each subset, is a type of low-pass filter which is used to remove some of the short-term random variation, therefore, affects the fluctuation of the moving average. The LES approach solves for the unsteady instantaneous flow field of motion and, hence, the moving average can be used as a suitable methodology to tackle the dynamic characteristics of an unsteady flow. Figure A-5 (a) shows an example of instantaneous and moving average velocity profiles obtained from the LES modelling. It can be seen that the moving average provides a “smoother” trend of the transient velocity variation by filtering most of the random fluctuations. Figure A-5 (b) shows the variation of the RMS of the fluctuating velocity component u' with the averaging time $\langle t \rangle$ (the symbol “ $\langle \rangle$ ” means the average of the variable), where $\langle t \rangle$ is calculated by $\langle t \rangle = (k - 1)\Delta t$. The time step size Δt is 0.001 *secs*, as discussed previously. It is found that u' exhibits a more gradual growth with $\langle t \rangle$, which infers that as the averaging time increases, more fluctuations are filtered and the moving average profile becomes smoother. It is pointed out here that when $\langle t \rangle$ increases and gets equal to the total flow time, the moving average value will become equal to the arithmetic average value, whereas when $\langle t \rangle$ decreases to zero, the moving average value will be the same as the instantaneous value.

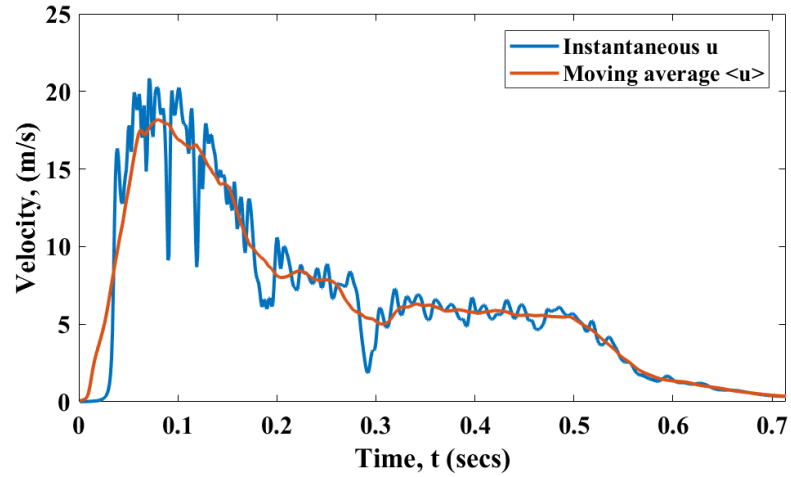


Figure A-5 (a): Comparison of instantaneous and moving average velocity profiles from the LES modelling.

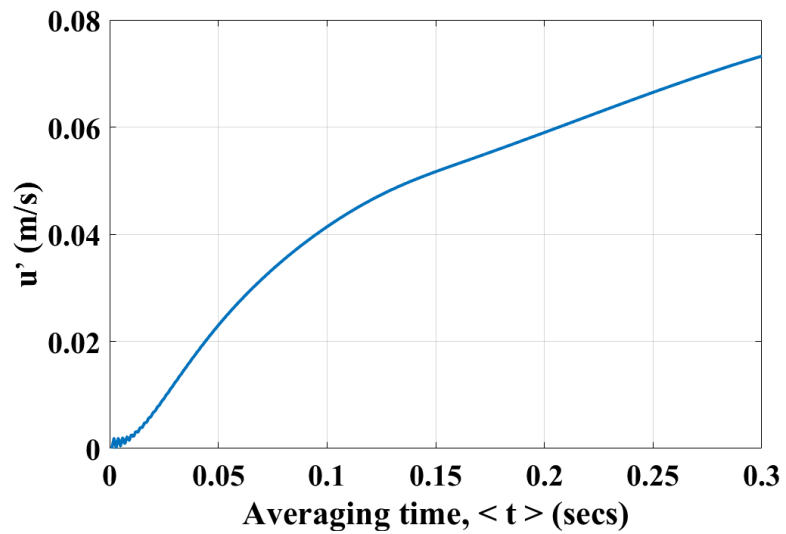


Figure A-5 (b): u' at $(1, 0, 0)$ versus the averaging time $\langle t \rangle$.

Reference

- Booth, E., Mount, J., & Viers, J. H. (2006). Hydrologic variability of the Cosumnes River floodplain. *San Francisco Estuary and Watershed Science*, 4(2).
- Mohamed, A. F. A. (2017). *Experimental Measurements of Far Field Cough Airflows Produced by Healthy and Influenza-Infected Human Subjects*. M. E. Sc. Thesis, Department of Mechanical and Materials Engineering, The University of Western Ontario.

Appendix H: Grid Independence Tests

In the present study, irregular unstructured polyhedral grids are implemented for both the URANS and LES modelling. The main merit of such a grid is that each polyhedral cell has more neighbours compared with tetrahedral or hexahedral grids, which is beneficial for calculating gradients and interpolations more accurately (Peric & Ferguson, 2004). In order to generate polyhedral grids, the tetrahedral grids are created first and then a conversion algorithm in FLUENT 16.0 is used, which merges the tetrahedral cells into polyhedral ones with a subsequent decrease in the total number of computational cells (80% on average) (ANSYS, 2014).

Normally, it is considered that the smaller the grid size, the more precise the numerical prediction. However, computational time should also be taken into consideration as it will be extremely long when a meritoriously fine mesh is being used. The grid independence, also known as grid convergence or sensitivity, is examined in order to balance the prediction accuracy and computational expense by comparing the numerical results obtained from grids with different sizes. If the grid independence is accomplished, the results from the two finest grids should be almost identical and would not be improved by an even finer grid (Cox-Stouffer, 1997).

To test the grid independence for the URANS modelling, a series of steady-state RANS simulations are carried out using different grid sizes (Spiegel et al., 2011). The detailed grid information is given in Table A-3, where it should be emphasized that the grid size in the global region increases with the growing ratio. Different dynamic characteristics, including the centreline mean velocity u_c , turbulent kinetic energy (TKE) k and half-width r_u , are compared to check the grid independence. Figure A-6 shows the streamwise variation of the inverse centreline mean velocity decay (u_j/u_c), normalized centreline TKE (k/u_c^2) and normalized half-width (r_u/d) for all the four grids, where u_j represents the inlet bulk velocity, which is 23.3 m/s (see Appendix A). The results of the grid independence test are summarized in Table A-4, where the difference percentages are calculated by using the root-mean-square (RMS) method. Based on Table A-4, the variabilities of u_j/u_c , k/u_c^2

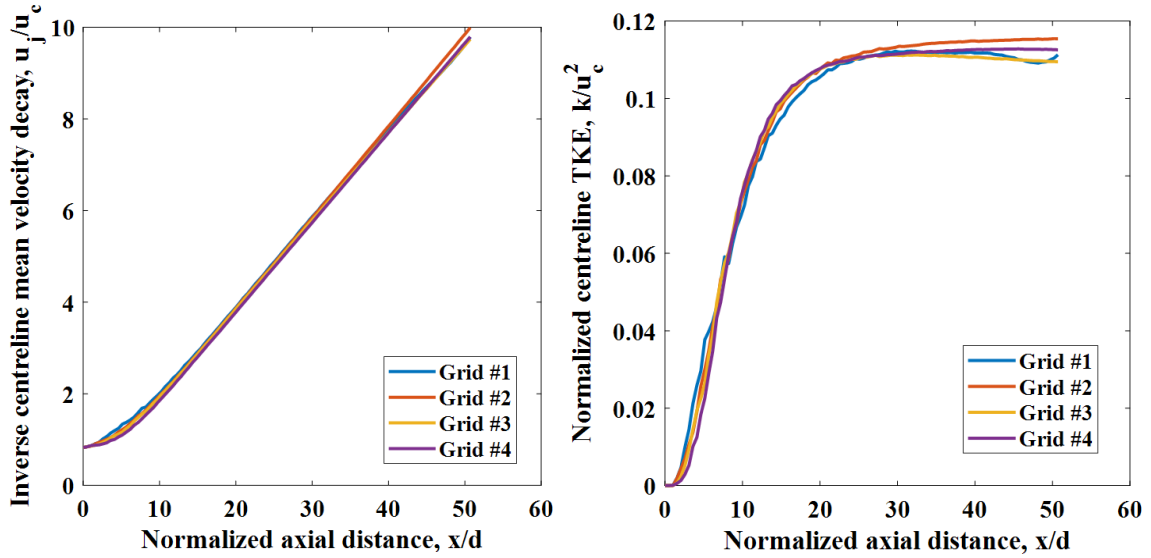
and r_w/d between Grids #3 to #4 are around 1%, which is small enough to be accepted as a grid convergence. Therefore, Grid #3 is used for the URANS modelling.

Table A-3: Information on different grids used for the URANS modelling.

Grid number	Inlet size (mm)	Cone region size (mm)	Number of computational cells (million)	Global growing ratio	Maximum aspect ratio
Grid #1	1	6.4	2.65	1.15	8.524
Grid #2	1	5.5	3.87	1.15	8.631
Grid #3	1	5.0	4.67	1.15	10.938
Grid #4	1	4.2	8.00	1.15	9.463

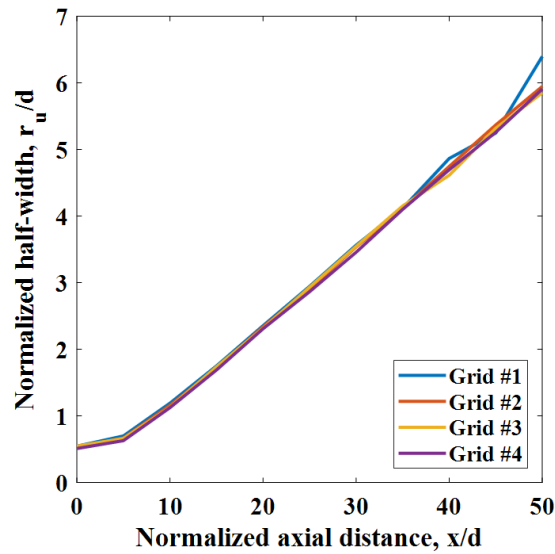
Table A-4: Grid independence tests for the URANS modelling.

Grid number	% Difference of u_j/u_c	% Difference of centreline k/u_c^2	% Difference of r_w/d
Grid #1	-	-	-
Grid #2	0.89	2.76	2.47
Grid #3	1.03	2.69	0.95
Grid #4	0.57	1.84	0.93



(a)

(b)



(c)

Figure A-6: Streamwise variation of (a) inverse centreline mean velocity decay, (b) normalized centreline TKE and (c) normalized half-width.

For the LES modelling, three grids in different size levels are created, as summarized in Table A-5. The moving average of the velocity u component (i.e. $\langle u \rangle$) along the centreline of the domain is selected to test the grid independence. The details about the moving

average methodology are shown in Appendix G. Figure A-7 (a) shows the streamwise variation of the peak value of $\langle u \rangle$ along the centreline, whilst Figure A-7 (b) shows the variation of the time corresponding to the peak value of $\langle u \rangle$. It is illustrated that the difference of the variation between Grids #5 and #6 is more apparent than that between Grids #6 and #7, which can also be found numerically from Table A-6 where the four centreline locations are in the unit of metres. The time history of $\langle u \rangle$ at various locations along the centreline for all the three grids is shown in Figure A-8. It is found that as the flow moves downstream, the variation of the moving average velocity $\langle u \rangle$ with time becomes more unstable, i.e., more fluctuations are observed, which reveals that the effect of turbulence becomes more significant due to the vortex formation process downstream. The results of the grid independence test are given in Table A-6, based on which the variabilities between Grid #6 and #7 are less but very close to those between Grid #5 and #6, hence in the present study, Grid #7 is chosen considering the simulation accuracy.

Table A-5: Information on different grids used for the LES modelling.

Grid number	Inlet size (mm)	Cone region size (mm)	Number of computational cells (million)	Global growing ratio	Maximum aspect ratio
Grid #5	1	6.4	3.7	1.15	8.891
Grid #6	1	5.5	5.6	1.15	11.411
Grid #7	1	5.0	7.3	1.15	10.877

Table A-6: Grid independence tests for the LES modelling.

Grid number	% Difference of peak $\langle u \rangle$	% Difference of time corresponding to peak $\langle u \rangle$	% Difference of $\langle u \rangle$ at (0.1, 0, 0)	% Difference of $\langle u \rangle$ at (0.2, 0, 0)	% Difference of $\langle u \rangle$ at (0.3, 0, 0)	% Difference of $\langle u \rangle$ at (0.4, 0, 0)
Grid #5	-	-	-	-	-	-
Grid #6	3.71%	4.80%	2.25%	4.81%	4.71%	7.75%
Grid #7	3.22%	3.12%	1.15%	4.26%	4.46%	7.14%

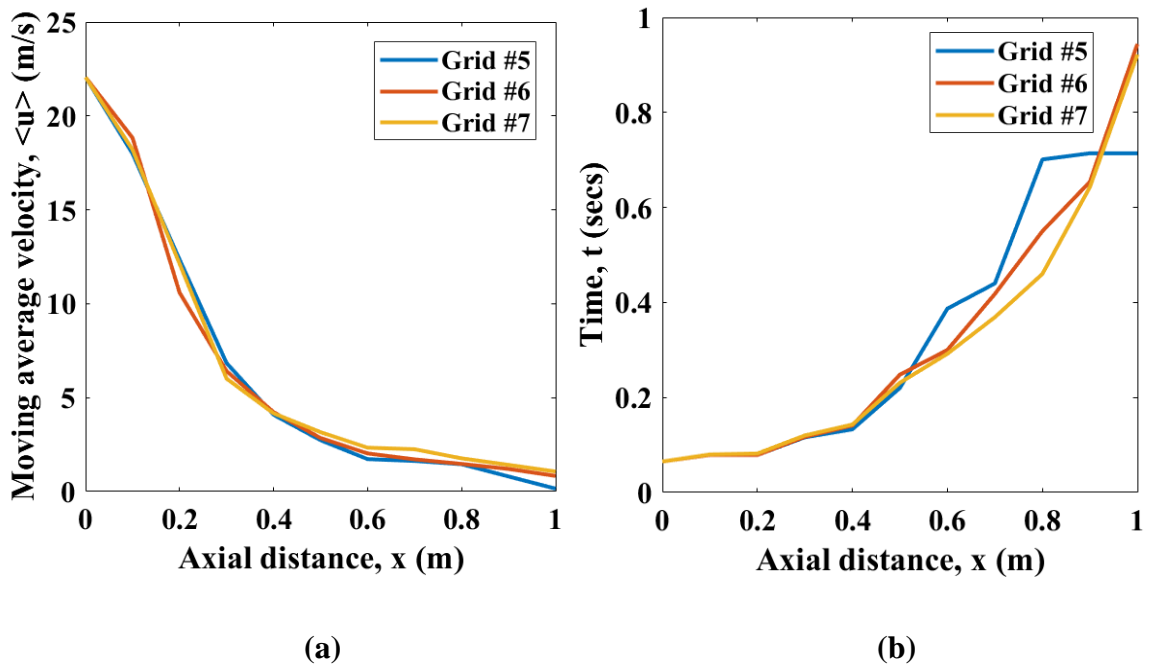


Figure A-7: Streamwise variation of (a) the peak value of $\langle u \rangle$ along the centreline and (b) the time when peak $\langle u \rangle$ occurs.

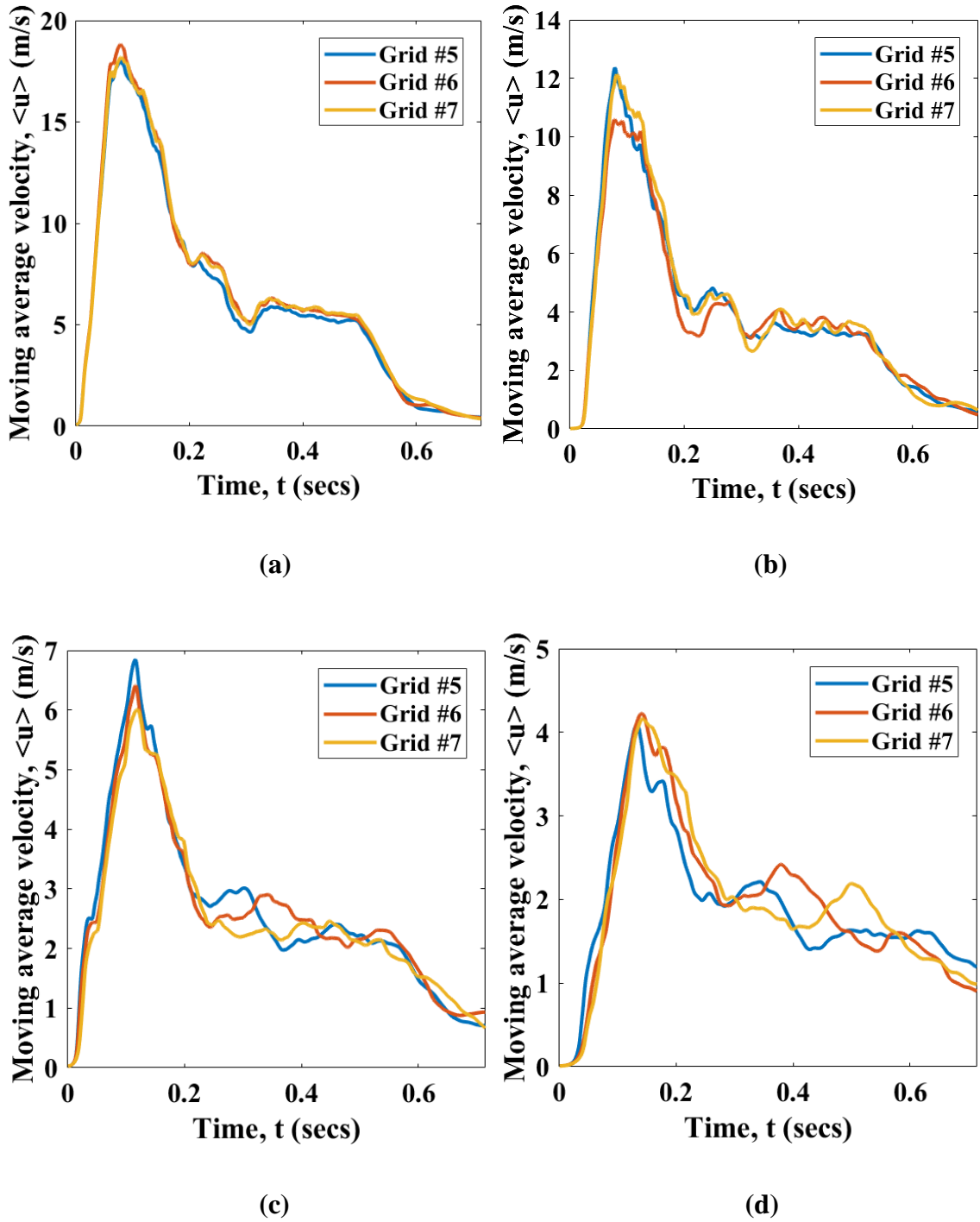


Figure A-8: Time history of $\langle u \rangle$ at centrelines locations of (a) (0.1, 0, 0), (b) (0.2, 0, 0), (c) (0.3, 0, 0) and (d) (0.4, 0, 0). The coordinates are in the unit of metres.

Reference

ANSYS, Inc. (2014). *ANSYS Fluent User's Guide 15.0*.

Cox-Stouffer, S. K. (1997). *Numerical Simulation of Injection and Mixing in Supersonic Flow*. Virginia Polytechnic Institute and State University.

Peric, M., & Ferguson, S. (2004). The advantage of polyhedral meshes. Retrieved from www.cd-adapco.com.

Spiegel, M., Redel, T., Zhang, Y. J., Struffert, T., Hornegger, J., Grossman, R. G., Doerfler, A., & Karmonik, C. (2011). Tetrahedral vs. polyhedral mesh size evaluation on flow velocity and wall shear stress for cerebral hemodynamic simulation. *Computer Methods in Biomechanics and Biomedical Engineering*, 14(1), 9–22.

Appendix I: The DRW Model

For the prediction of the droplet dispersion, the integral time scale T is introduced and expressed as

$$T = \int_0^{\infty} \frac{u'_p(t)u'_p(t-\tau)}{\overline{u'^2_p}} d\tau \quad (\text{A-36})$$

which is proportional to the droplet dispersion rate, i.e. the larger the value of T , the more turbulent motion the droplets will get. The droplet diffusivity is defined as $\overline{u'_i u'_j} T$.

For the small droplets which have the diameter smaller than a few microns and move with the continuous phase, T becomes the fluid Lagrangian integral time scale T_L , which is calculated from

$$T_L = C_L \frac{k}{\varepsilon} \quad (\text{A-37})$$

where the value of the time scale constant C_L is different for different turbulence models that are used to model the continuous phase.

By using the DRW model, the interaction between a droplet and a succession of turbulent eddies in the continuous phase is modelled (Gosman & Ioannides, 1983). Each eddy is characterized by the random fluctuating velocity components (i.e. u' , v' and w') and a time scale τ_e , named the characteristic lifetime. The values of u' , v' and w' of a turbulent eddy are assumed to obey the Gaussian probability distribution for sampling, and are defined as

$$u' = \zeta \sqrt{\overline{u'^2}} \quad (\text{A-38})$$

where ζ represents a normally distributed random number for the Gaussian distribution, and $\sqrt{\overline{u'^2}}$ is the root-mean-square (RMS) value of the fluctuating velocity component. The eddy lifetime τ_e is expressed as

$$\tau_e = 2T_L \quad (\text{A-39})$$

Another time scale t_{cross} , named the particle-eddy crossing time, is defined as

$$t_{cross} = -\tau_p \ln \left[1 - \left(\frac{L_e}{\tau_p |u - u_p|} \right) \right] \quad (\text{A-40})$$

where L_e represents the eddy length scale, $|u - u_p|$ is the relative velocity magnitude between the droplet and the flow field, and τ_p is the droplet relaxation time, computed from

$$\tau_p = \frac{\rho_p d_p^2}{18\mu} \quad (\text{A-41})$$

The droplet is assumed to interact with a turbulent eddy over the smaller of τ_e and t_{cross} . When this time is reached, the instantaneous flow velocity with a new value will be obtained through employing a new random number ζ in Eqn. (A-38).

Reference

Gosman, A. D., & Ioannides, E. (1983). Aspects of computer simulation of liquid-fuelled combustors. *Journal of Energy*, 7(6), 482–490.

Appendix J: Droplet Trajectory

The droplet velocity u_p at each point along the trajectory is yielded by stepwise integration of the force balance equation, i.e. Eqn. (3.6), with respect to the discrete time steps, and the trajectory itself is calculated by integrating the following equation,

$$\frac{dx_p}{dt} = u_p \quad (\text{A-42})$$

It is noteworthy that Eqns. (3.6) and (A-42) are a set of coupled ordinary differential equations, and Eqn. (3.6) can also be expressed in a general form,

$$\frac{du_p}{dt} = \frac{1}{\tau_p}(u - u_p) + g \quad (\text{A-43})$$

where g represents the gravitational acceleration of the droplet.

In order to obtain the droplet velocity at a new position, i.e. u_p^{n+1} , different integration schemes are available, including implicit, analytic, trapezoidal and Runge-Kutta schemes. When applying the implicit scheme to Eqns. (A-43) and (A-42), u_p^{n+1} and the corresponding position x_p^{n+1} are given respectively by

$$u_p^{n+1} = \frac{u_p^n + \Delta t(a + \frac{u_p^n}{\tau_p})}{1 + \frac{\Delta t}{\tau_p}} \quad (\text{A-44})$$

$$x_p^{n+1} = x_p^n + \frac{1}{2}\Delta t(u_p^n + u_p^{n+1}) \quad (\text{A-45})$$

The implicit integration scheme takes most of the variations in the forces, which act on the droplets, into consideration, and gives a higher accuracy in predicting the situations when a large time step size is used or the droplets are not in hydrodynamic equilibrium with the continuous phase (ANSYS, 2013), and therefore, it is chosen in the present study. Moreover, for the small droplets moving with the continuous phase, the velocity of the droplets is the same as that of the continuous phase, i.e. $u_p = u$, and the new trajectory position is obtained from Eqn. (A-45).

Reference

ANSYS, Inc. (2013). *ANSYS Fluent Theory Guide 15.0*.

Appendix K: Stochastic Collision and Coalescence

For N droplets, each droplet has $N - 1$ possible collision partners, and hence there will be $\frac{1}{2}N^2$ possible collision pairs. Normally a spray may contain thousands of droplets, which makes the computational expense of the collision calculation prohibitive. In this case, the concept of a parcel is introduced, which is defined as a statistical representation of a number of individual droplets in the same size range (ANSYS, 2013). Moreover, a second-order scheme of O'Rourke (1981) is used to estimate the stochastic collision between the droplets produced by coughing to lower the computational cost. Such algorithm assumes that two parcels of droplets may collide only if they are located within the same computational cell, and prevents the droplets, which are not distributed in the same cell but quite close to each other, from colliding.

The probability of a collision between two droplets is computed from

$$P = \frac{\pi(r_1+r_2)^2 v_{rel} \Delta t}{V} \quad (\text{A-46})$$

where r_1 and r_2 are the radius of the larger and smaller droplet, respectively, v_{rel} is the relative velocity between these two droplets, and V represents the volume of the computational cell. For two parcels, of which one contains n_1 larger droplets and the other contains n_2 smaller droplets, the mean number of collisions is calculated from

$$\bar{n} = \frac{n_2 \pi (r_1 + r_2)^2 v_{rel} \Delta t}{V} \quad (\text{A-47})$$

The actual number of collisions (n) is not the same as the mean number of collisions (\bar{n}). According to O'Rourke (1981), the probability of the actual number of collisions follows a Poisson distribution, as shown in the following equation,

$$P(n) = e^{-\bar{n}} \frac{\bar{n}^n}{n!} \quad (\text{A-48})$$

As a result of collision, the coalescence is also considered in the discrete phase model. The probability of a coalescence is dependent on a critical offset, which is a function of the radii of the larger and smaller droplets and is expressed as

$$b_{crit} = (r_1 + r_2) \sqrt{\min(1.0, \frac{2.4f}{We})} \quad (\text{A-49})$$

where f is defined as

$$f = \left(\frac{r_1}{r_2}\right)^3 - 2.4 \left(\frac{r_1}{r_2}\right)^2 + 2.7 \left(\frac{r_1}{r_2}\right) \quad (\text{A-50})$$

and We is the collisional Weber number, given as

$$We = \frac{\rho U_{rel}^2 \bar{D}_p}{\sigma} \quad (\text{A-51})$$

where \bar{D}_p represents the mean diameter of two parcels of droplets, ρ is the density of the continuous phase, σ is the droplet surface tension, and U_{rel} is the relative velocity between the two parcels.

Another parameter, named the actual collision parameter (b), is defined as

$$b = (r_1 + r_2) \sqrt{Y} \quad (\text{A-52})$$

where Y represents a random number with the value between 0 and 1, and is compared with the critical offset b_{crit} . If $b < b_{crit}$, the coalescence will occur as an outcome of the collision between the two parcels.

Reference

ANSYS, Inc. (2013). *ANSYS Fluent Theory Guide 15.0*.

O'Rourke, P. J. (1981). *Collective Drop Effects on Vaporizing Liquid Sprays*. Princeton University, Princeton, New Jersey.

Appendix L: User-Defined Function of the Inlet Velocity Profile for the CFD

Modelling of the Steady Round Free Jet Flow

```

#include "udf.h"
DEFINE_PROFILE(inlet_x_velocity_modifi, thread, index)
{
    real x[ND_ND]; /* this will hold the position vector */
    real y;
    real z;
    real a;
    face_t f;
    begin_f_loop(f, thread) /*loops over all faces in the thread
passed in the DEFINE macro argument*/
    {
        F_CENTROID(x,f,thread);
        y =x[1];
        z =x[2];
        a = pow((pow(y,2)+pow(z,2)),0.5);
        if (a>0.398012267*0.055)
            F_PROFILE(f, thread, index)=(-
60.699/pow(0.055,2)*pow(a,2)+44.704/0.055*a-7.177)*23.3;
        else
            F_PROFILE(f, thread, index)=23.3;
    }
    end_f_loop(f, thread)
}

```

Curriculum Vitae

Name:	Ran Bi
Post-secondary Education and Degrees:	<p>China University of Mining and Technology Xuzhou, Jiangsu, China 2009-2013 B. Eng.</p> <p>The University of Western Ontario London, Ontario, Canada 2015-2016 M. Eng.</p> <p>The University of Western Ontario London, Ontario, Canada 2016-2018 M. E. Sc.</p>
Honours and Awards:	<p>Excellent Student Scholarship of School of Mechatronic Engineering 2012-2013</p> <p>First-Class Scholarship of School of Mechatronic Engineering 2013-2014</p>
Related Work Experience	<p>Teaching Assistant The University of Western Ontario 2016-2017</p> <p>Research Assistant The University of Western Ontario 2016-2017</p>